Development of Nanosecond Range Light Sources for Calibration of Astroparticle Cherenkov Detectors

Omar Veledar

PhD

2007

Development of Nanosecond Range Light Sources for Calibration of Astroparticle Cherenkov Detectors

Omar Veledar

The thesis is submitted in partial fulfilment of the requirements for the award of Doctor of Philosophy

University of Northumbria at Newcastle
School of Computing, Engineering and Information Sciences

May 2007

Abstract

In this thesis the development of light emitting diodes (LED) is reviewed. The emphasis is put on devices emitting at the blue region of the spectrum. The physical characteristics of these devices are considered. The main interest is based around the ability of blue LEDs to generate nanosecond range optical flashes.

The fast pulsing electronic circuits capable of driving the devices are also reviewed. These are complemented by the potentially exploitable techniques that could provide further benefits for required fast optical pulse generation.

The simple, compact and inexpensive electronic oscillator for producing nanosecond range pulses is developed. The circuitry is adapted for generation of pulses necessary to switch on and assist with the turn off of blue InGaN based LEDs. The resulting nanosecond range blue optical pulses are suitable for, but not limited to, the calibration of scintillation counters. These devices used in neutrino detection experiments could provide a better understanding of cosmology and particle physics.

Contents

List of Symbols v

List of Acronyms viii

Acknowledgements ix

Author's Declaration x

Publications as a Result of Work on this Thesis xi

1 Introduction 1

1.1 Current State of the Art . . . 3
1.2 Present Applications . . . 3
1.3 Objectives . . . 5
1.4 Scope of the Thesis . . . 6
1.5 Contributions . . . 6
1.6 Thesis Structure . . . 6

2 The Light Emitting Diode 8

2.1 LED Development . . . 8
2.1.1 Present devices . . . 9
2.1.2 Future Devices . . . 16
2.2 LED Characteristics . . . 18
2.2.1 Charge Properties . . . 18
2.2.2 The P-N Junction . . . 20
2.2.3 Electrical Properties . . . 23
2.2.4 Optical Properties . . . 28
2.3 Advanced Structures - High Brightness LEDs . . . 29
2.3.1 Single Heterojunction . . . 30
2.3.2 Double Heterojunction . . . 31
2.3.3 Single Quantum Well - InGaN Based LEDs . . . 31
2.3.4 Manufacture of High Brightness LEDs . . . 33

2.4 Applications 35
2.5 Chapter 2 Summary 37

3 Pulse Shaping Techniques and LED Pulse Response **38**
3.1 Types of LED Drivers 38
3.1.1 Multivibrators 39
3.1.2 Emitter Coupled Monostable 39
3.1.3 Avalanche Transistors 40
3.1.4 Complementary Transistor Pair Regenerative Switch 41
3.1.5 Standard Telecommunication Techniques 42
3.2 Overview of Standard Pulse Shaping Techniques 42
3.2.1 Differentiation 42
3.2.2 Step Recovery Diode 43
3.2.3 Clipping and High Speed Comparators 43
3.2.4 Non-Saturating Switch 44
3.2.5 Speed up Commutating Capacitor for Transistor Switching . . . 45
3.2.6 Shorted Turn - Theory and Application 46
3.3 LED Switching Parameters 50
3.4 Basic Switching Principles 52
3.5 Chapter 3 Summary 53

4 LED Modelling **54**
4.1 OrCAD Models 55
4.1.1 Ideal Diode Static Model 55
4.1.2 Real Diode Static Model 56
4.1.3 Large Signal Model 59
4.2 Behavioural Models 60
4.3 Chapter 4 Summary 61

5 Experimental and Modelled LED Characteristics **62**
5.1 Methods and Results 62
5.1.1 Capacitance - Voltage Relationship 63
5.1.2 Current - voltage relationship 71
5.1.3 LED Output Spectrum 73
5.1.4 Current - Output Light Intensity Relationship 74
5.1.5 LED as a Photodetector 75
5.1.6 Correlation 77
5.2 Modelling Results 81

5.2.1 OrCAD Model Editor . . . 81
5.2.2 OrCAD Behavioural Model . . . 82
5.2.3 MATLAB Behavioural Model . . . 84
5.2.4 Model Comparison . . . 84
5.3 Chapter 5 Summary . . . 86

6 Optical Pulse Generation **88**
6.1 Investigation of the Current Arrangement . . . 88
6.2 Totem-Pole Drivers . . . 90
6.3 Single Output Configurations . . . 92
6.3.1 Switching Configuration . . . 92
6.3.2 Pulse Shaping . . . 93
6.3.3 Measurement Technique . . . 95
6.3.4 Results and Discussion . . . 96
6.3.5 Error Treatment . . . 99
6.4 Multiple Output Configuration . . . 100
6.4.1 Circuit Arrangement . . . 101
6.5 Chapter 6 Summary . . . 104

7 Conclusions and Recommendations for Further Work **105**
7.1 Conclusions . . . 105
7.2 Further Work . . . 106

A Practical Diode Equation Analysis **108**
A.1 Analysis by inspection . . . 108
A.2 Mathematical Analysis . . . 109
A.2.1 Manual Solution . . . 110

B SPICE Diode Model Parameters **113**

C LED Capacitance Analysis **115**
C.1 Inverse Capacitance Squared Versus Voltage Plots . . . 115
C.2 Depletion Capacitance Fit . . . 115
C.3 Diffusion Capacitance Fit . . . 116
C.4 Hump Capacitance Fit . . . 117
C.5 Fitting Errors . . . 118

D LED Current - Voltage Analysis **122**

E LED Output Spectrum Analysis **125**

F LED Intensity Analysis **126**

G Using LED as a Photodetector **127**

H Blue LED Model Netlist - Using OrCAD Model Editor **130**

List of Symbols

The following is a list of symbols used in the thesis:

Symbol	Unit	Description
A	m^2	cross sectional area
A_c	m^2	core area
B	T	Magnetic Flux Density
BV	V	breakdown voltage
C_D	F	diode capacitance
C_d	F	diffusion or injection capacitance
C_j	F	junction or depletion capacitance
$D_{n/p}$	m^2s^{-1}	diffusion coefficients
$E_{c1,2,3...}$	eV	energy of conduction band level
$E_{g(well)}$	eV	well material energy band gap
E_{gQW}	eV	Quantum well energy band gap
$E_{v1,2,3...}$	eV	energy of valance band level
f	Hz	frequency
$FWHM_{(observed)}$	s	measured FWHM
$FWHM_{(optical)}$	s	optical signal FWHM
$FWHM_{(system)}$	s	measuring system FWHM
h	Js	Planck's constant ($6.6260755 \times 10^{-34} Js$)
H	Am^{-1}	Magnetic Field Strength
I or i	A	current
$I_{(r,g)}$	A	generation-recombination current
$I_{D(ideal)}$	A	ideal diode current
I_n	A	electron current
I_s	A	saturation current
J_{COND}	Am^{-2}	sum of all drift and diffusion current densities
J_{diff}	Am^{-2}	diffusion current density
J_{drift}	Am^{-2}	drift current density
J_n	Am^{-2}	electron current density
$J_{n(diff)}$	Am^{-2}	electron diffusion current density
$J_{n(drift)}$	Am^{-2}	electron drift current density
J_p	Am^{-2}	hole current density
$J_{p(diff)}$	Am^{-2}	hole diffusion current density
$J_{p(drift)}$	Am^{-2}	hole drift current density
J_s	Am^{-2}	saturation current density
k	NmK^{-1}	Boltzmann's constant ($1.3806568 \times 10^{-23} JK^{-1}$)
l	m	carrier mean free path

Symbol	Unit	Description
l_c	m	core mean length
l_{QW}	m	quantum well length
L	H	inductance
L_0	H	inductance in a coil with an air core
L_n	m	electron minority carrier diffusion length
L_p	m	hole minority carrier diffusion length
m_e^*	kg	electron effective mass
m_h^*	kg	hole effective mass
m_r^*	kg	reduced effective mass
n	m^{-3}	electron concentration
n_i	m^{-3}	intrinsic carrier concentration
n_{n0}	m^{-3}	majority electron carrier equilibrium concentration
n_p	m^{-3}	minority electron carrier concentration
n_{p0}	m^{-3}	minority electron carrier equilibrium concentration
N		number of coil turns
N_A	m^{-3}	acceptor impurity concentration
N_B	m^{-3}	impurity concentration of the lightly doped side
N_D	m^{-3}	donor impurity concentration
p	m^{-3}	hole concentration
p_n	m^{-3}	minority hole carrier concentration
p_{n0}	m^{-3}	minority hole carrier equilibrium concentration
p_{p0}	m^{-3}	majority hole carrier equilibrium concentration
q	C	Electron charge ($1.60217733 \times 10^{-19}C$)
Q	C	charge
Q_d	C	diffusion charge - due to minority carrier injection
Q_D	C	charge stored by a diode
Q_j	C	depletion charge - due to doping atoms concentration
Q_n	C	stored (electron) charge per unit area
Q_p	C	stored (hole) charge per unit area
R		rate of direct recombination (radiation efficiency)
$R(f)$		LED frequency response
R_p	Ω	diode parallel resistance
R_s	Ω	diode series resistance
t	s	time
t_{fall}	s	fall time
t_{rise}	s	rise time
T	K	Temperature
v_{bi}	V	built in voltage
v_i	ms^{-1}	electron individual drift velocity
v_n	ms^{-1}	average electron drift velocity
v_p	ms^{-1}	average hole drift velocity
v_{th}	ms^{-1}	carrier thermal velocity
V	V	Voltage
V_{BE}	V	transistor base-emitter voltage
V_{EB}	V	transistor emitter-base voltage
V_t	V	diode thermal voltage
W	m	depletion layer width

Symbol	**Unit**	**Description**
x	m	distance from the junction
x_n	m	distance from the junction into n side
x_p	m	distance from the junction into p side
β	m^3s^{-1}	radiation constant of proportionality
ε	NC^{-1}	electric field
ϵ_S	Fm^{-1}	semiconductor dielectric permittivity
η		ideality factor or emission coefficient
μ_0	Hm^{-1}	permeability in free space
μ_n	$m^2(Vs)^{-1}$	electron mobility
μ_p	$m^2(Vs)^{-1}$	hole mobility
μ_r	Hm^{-1}	relative permeability
ν	Hz	frequency of light
ξ	V	emf
τ_c	s	mean free time (minority carrier lifetime)
$\tau_{f(PMT)}$	s	PMT fall time
$\tau_{f(scope)}$	s	oscilloscope fall time
$\tau_{f(system)}$	s	measuring system fall time
τ_n	s	excess minority electron carriers' lifetime
τ_p	s	excess minority hole carriers' lifetime
$\tau_{r(PMT)}$	s	PMT rise time
$\tau_{r(scope)}$	s	oscilloscope rise time
$\tau_{r(system)}$	s	measuring system rise time
ϕ	Wb	magnetic flux

The additional symbols used for the SPICE diode model parameters are shown in appendix B.

List of Acronyms

The following is a list of acronyms used in the thesis:

Acronym	**Meaning**
AC	Alternating Current
ANTARES	Astronomy with a Neutrino Telescope and Abyss environmental RESearch
DC	Direct Current
DH	Double Heterojunction
DUT	Device Under Test
DVM	Digital Volt-Meter
ECL	Emitter-Coupled Logic
ELOG	Epitaxially Laterally Overgrown
FWHM	Full Width Half Maximum
EMF	Electro-Magnetic Force
HVPE	Hybrid Vapour Phase Epitaxy
IR	Infrared
LAN	Local Area Network
LCD	Liquid Crystal Display
LD	Laser Diode
LED	Light Emitting Diode
LEEBI	Low-Energy Electron Beam Irradiation
MATLAB	MATrix LABoratory
MIS	Metal-Insulator-Semiconductor
MOCVD	Metal Organic Vapour Deposition
MOVPE	Metal-Organic Vapour Phase Epitaxy
MQW	Multi Quantum Well
OLED	Organic Light Emitting Diode
PMT	Photomultiplier Tube
PSPICE	Personal computer Simulation Program with Integrated Circuit Emphasis
QW	Quantum Well
SCADAS	Spectrometer Control And Data Acquisition System
SH	Single Heterojunction
SL	Super Lattice
SMD	Surface Mount Device
SQW	Single Quantum Well
TF-MOCVD	Two Flow Metal Organic Vapour Deposition
UV	Ultra Violet

Acknowledgements

I wish to express my thanks to those that helped me survive this mammoth ordeal that has been my PhD. My sincere thanks go to my long-suffering supervisors who have endured through the exponential rise in the frequency of my questions I generated for every answer that we stumbled across. I am indebted to my director of studies, Dr Sean Danaher, for his patience and guidance even at the times when many others would have been discouraged (and for my first, but certainly not the last, pint of Guinness). Special credits go to Prof Phillip O Byrne for his practical guidance, endless inspiring conversations over staff bar 'tea parties' and for giving me hope that there might be few more engineers out there who are happy to use a soldering iron. Thanks also go to Mr Joseph I H Allen for his patience, support and advice. I am also grateful to Dr Lee F Thompson for initiating the project, giving me the opportunity to be a part of it and also for his support.

A special mention goes to my colleagues, with whom I shared an office over the past few years, for their friendship and the odd hangover. I admire their ability to cope with my live performances. I would also like to thank the School's technicians Allan, Keith, Tom, Phil and John for their technical assistance, the academic staff for their support and to the ladies from the school office for painstakingly dealing with my paperwork.

I would also like to acknowledge the financial support received from the School and the University in the form of my scholarship without which this thesis would have not been achieved. I am grateful to Prof Alistair Sambell for providing me with that opportunity.

Several individuals, who will be able to recognise themselves in this paragraph, have proved to be my very effective life pillars in recent years. In simple terms, if it were not for them I would not be what I am (good or bad) today. Consequently, no words could be used to describe my appreciation.

Most importantly I would like to thank my parents and my sister for their love and support without which my life would have been very different and none of this would have been possible. Finally, I would like to thank my late grandmother for her love, inspiration and also for her patience while waiting for me to leave the 'school' and get a 'proper job'. She sadly missed it by a matter of weeks.

Author's Declaration

I declare that the work contained in this thesis has not been submitted for any other award and that it is all my own work.

Name Omar Veledar

Signature

Date

Publications as a Result of Work on this Thesis

Journals:

- Veledar O, Byrne P O, Danaher S, Allen J I H, Thompson L F and John E McMillan, *Simple techniques for generating nanosecond blue light pulses from light emitting diodes*, Measurement Science and Technology, **18** (2007) 131-137
- Veledar O, Danaher S, Allen J I H, Byrne P O and Thompson L F, *Review and development of nanosecond pulse generation for light emitting diodes,* Scientific Reports, Journal of the University of Applied Sciences Mittweida (Wissenschaftliche Berichte, Wissenschaftliche Zeitschrift der Hochschule Mittweida (FH)) **9/10** 2005 3-6

Conference talks:

- Veledar O, Danaher S, Allen J I H, Byrne P O and Thompson L F, *Review and development of nanosecond pulse generation for light emitting diodes,* 17th International Scientific Conference in Mittweida, Germany 2005 – keynote speech by Veledar O
- Veledar O, Danaher S, Allen J I H, Thompson L F, and Byrne P O, *Design of a high-speed blue light source for calibration purposes*, Institute of Physics Optical Group, Young Researchers in Optics 05 at Imperial College London, 21/09/05

Posters:

- Veledar O, *High-Speed Blue Light Source for Calibration in Physics Experiments*, UK GRAD Yorkshire and North East Hub Poster Competition and Networking Event – Promoting your Research to the Public, 03/05/06

Chapter 1

Introduction

As the quest to devise the theory of everything continues, the physics experiments are continuing to expand the technological boundaries. The advances in the science and technology continually support the search for new information. Some of the resulting experimental initiatives that incorporate scintillators and photomultiplier tubes (PMT) offer fresh avenues of research that contribute to our improved understanding of the physical phenomena. Some of these experiments are based on detection of the Cherenkov radiation emitted by the neutrino-generated muon travelling through the seawater. The Cherenkov radiation is electromagnetic radiation emitted when a particle, that passes through a medium at a speed greater than the speed of light in that medium, causes constructive interference [1]. There are few operational experiments around the globe that are indirectly detecting neutrinos [2–6]. The observation of high-energy extraterrestrial neutrinos is one of the most promising future options to increase our knowledge of non-thermal processes in the universe [7]. Neutrinos are ideal astrophysical messengers as they are not deflected by electromagnetic fields and their weakly interacting nature allows them to escape even from very dense regions and travel large distances without attenuation [7]. Our future progress in understanding these particles largely depends on the improvements of the already existing experiments that are aimed at detection of these particles.

Correct operation of the experiments that are based on detection of this radiation require fast, clearly defined optical pulses. Various techniques can be applied for creation of fast optical pulses, but they are not necessarily exploitable in all required situations. The simplest method of creating well-defined optical pulses in required nanosecond range involves the use of lasers. In majority of applications the highly directional monochromatic beam of light is seen as advantageous. Lasers of semiconductive nature are also beneficial at the required frequency of operation because they can be controlled by simple modulation of the biasing current.

A disadvantage carried by the laser technology is that the laser setup highlights the cost issue. This should not represent a great difficulty for small-scale projects where

few optical sources are required. However, a vast number of optical sources necessitated by some large scientific experiments creates financially a considerably more challenging atmosphere.

ANTARES, an experiment considered in this thesis, requires 2196 fast pulsing blue optical sources. The expected redevelopment of the experiment into a new one (KM3NeT), that will occupy a km^3 of volume in the Mediterranean Sea, will considerably increase the number of required optical sources. The financial burden caused by the use of lasers in such a situation is simply prohibitive considering the current state of laser technology. The immature blue laser technology inflates the problem. The simulated Cherenkov radiation emits light in the blue region. It is desirable for the simulating devices to emit light similar in wavelength to that for which the experiment is designed to detect. However, as blue pulsing lasers are not yet economically feasible and are still not technologically perfected, an alternative exploitable laser colour would be green. However, the green emission is not well matched to the spectral response of the PMTs employed in the experiment. The PMTs have a rather narrow spectral response at the blue end of spectrum and ideally require blue light for their calibration. Their spectral response is matched to that of the Cherenkov radiation.

Additionally the non-divergent beam of light (anisotropic radiation) generated by lasers is inappropriate in this application as the light is used to simulate a natural phenomenon that results in conical light emission. It is also favourable that the driving complexity is reduced. The disadvantages brought in by lasers heavily outweigh the possible advantages. Therefore an alternative solution is required.

An alternative to laser technology in this case is the use of Light Emitting Diodes (LED). The benefits generated by the cost reduction and production of isotropic radiation are the obvious reasons for the use of LEDs. Development of low cost high speed LEDs has made these devices suitable for use as pulsed light sources of a kind required for the proposed PMT calibration. The emitted optical spectrum of these devices has been considerably extended into the blue end of the spectrum in recent years, allowing good spectral match of the emitted light with that of the PMTs. These devices are currently capable of radiating from the Ultraviolet (UV) to the Infrared (IR) section of the spectrum.

Optical communication systems have long relied on the use of IR and red LEDs. This part of the spectrum has been exploited because of its suitability for light propagation along optical fibres. Hence, technology for the LEDs operating at longer wavelengths has advanced further than is the case with LEDs operating at the blue end of the spectrum. However, the ability of the LEDs to generate very fast light pulses is often exploited for calibration of scintillation counters and PMTs [8–11]. Some of those calibrating sources emit blue light, but there is a further need for development of better LED based fast pulsing calibration apparatus that radiates at the blue end of the

spectrum. The differences in physical and electrical characteristics between standard red LEDs and their blue counterparts prevent the use of blue LEDs in configurations previously developed for pulsing standard red LEDs. Furthermore, the blue LEDs are mainly manufactured for use as displays, indicators and more recently for lighting purposes. Their ability to be pulsed is not a manufacturing priority. Manufacturers do not guarantee their pulsing characteristics; any technological change does not need to support the pulsing ability of the devices as long as their *d.c.* characteristics are maintained. The reasons behind the pulsing ability of the devices are investigated so that any future unexpected manufacturing changes can be pre-empted with adequate actions.

1.1 Current State of the Art

Some existing optical pulse generators successfully utilise the switching speed of the avalanche transistors [12, 13] or transistor pairs regenerative switching action [14] in order to produce fast LED driving pulses. The light intensity generated with the avalanche transistor circuits is very poor. However, a series combination of the transistors allows higher intensity generation. However, the generated intensity per pulse is not necessarily repeatable. The regenerative switch type LED driver currently produces optical pulses with $6ns$ Full Width Half Maximum (FWHM) value. Even though this circuit is adequate for the PMT calibration in current setup, it is realised that further improvements are required if the circuit is to be used in the proposed expanded neutrino detection system (see Section 1.2). The experimental work presented in this thesis also addresses the shortage of the circuit development activities for the proposed applications.

1.2 Present Applications

The ANTARES [8, 9] deep-sea neutrino detector is under construction off the French south coast. This detector could provide a new understanding of astronomy and particle physics. The neutrino is an elementary particle with no charge and almost no mass. The study of low energy neutrinos adds to the knowledge of neutrino masses and their oscillations. The detection of high energy neutrinos contributes to our understanding of distant, massive astrophysical objects and it is generally accepted that they also might help in the discovery of the origin of dark matter. ANTARES relies heavily on its optical modules. Several hundreds of these modules are tied together and are anchored in Mediterranean Sea [8]. These modules, each containing a PMT, are calibrated with the use of the bright blue LEDs driven by the flash drivers. The modules are optimised for detection of Cherenkov radiation. This radiation is an indirect result of the rare

neutrino interactions in the matter surrounding the detector. In a charged current interaction a high energy neutrino generates a muon. This muon travels through water at a velocity comparable to that of light in a vacuum. As this velocity is larger than the velocity of light in seawater the Cherenkov radiation is emitted. This radiation is detected by the three-dimensional network of modules. The time and the position of the detected hits allow reconstruction of the muon trajectory. This trajectory is a continuation of the trajectory of the neutrino that generated the muon. As the time of radiation travel and position of the hit modules are crucial for reconstruction of the particle trajectory the calibration system that would allow precise positioning of the modules is required. The optical system is chosen because the optical properties of the deep sea water are more stable than the acoustic ones.

The first generation neutrino detection systems, such as ANTARES, have improved the understanding of the issues emerging in the field. However, the weakly interacting nature of the neutrinos makes the observations of these events extremely rare. There is a need for development of second generation detectors which would allow considerable increase of detector size in order to enable the neutrino detection astronomy beyond the single event count. Consequently, the planned ANTARES expansion has evolved into a new deep-sea research infrastructure KM3NeT [15, 16]. The volume of the new detection system is $1km^3$. Due to financial limitations it is not possible to populate such large volume with the same density of optical modules as it is the case in ANTARES. The effect of such limitation is the increase in the distance between the optical modules. This results in the need for more accurate calibration system. The required modifications principally include increase of optical pulse amplitude and shortening of the rise time and FWHM without increase in cost. The intensity improvement is required because of the expected optical attenuation in water increases as the distance between the LED drivers and the optical modules increases. The rise time is required to be faster than that of the employed PMTs so that the driver can be used for the calibration of the PMT rise time. The FWHM needs to be short because of the possible pulse broadening over the long distance. The pulse jitter needs to be minimised because of the required precision positioning. The main reason for our research and improvement of the existing optical pulse generation techniques is their potential application to the proposed neutrino detection system KM3NeT.

The reason for deep sea positioning of the above detector is the availability of natural radiation shield ($2.4km$ of sea water) from above as well as the freely available detection medium - Seawater. This advantageous environment however has a negative side. The fact that the electronic equipment is immersed $2.4km$ under the surface of the sea creates a challenge as the components need to provide reliable operation for long periods of time (minimum 10 years) [8]. Considering the necessity for long periods of accurate functionality and the importance of the signal accuracy, repeatability is one

of the major factors involved in the development of the electronic equipment for this application.

The medical community also has a strong interest in developing new, more sophisticated techniques for smart, non-invasive methods of cancer detection. Optical spectroscopy provides new ways to characterise physical and chemical changes occurring in tissues and cells and thereby offers exciting possibilities for novel diagnostic approach [17]. The tests consist of flashing the suspected area with light and observation of the cell response. The energised cells radiate in order to return to their original state. A change in the state of a cell or tissue, such as from normal to cancerous, will change the fluorescence [17–19]. There is a possibility for involvement of the proposed high-speed high power LED driver in the medical diagnostic field.

Other possible applications are identified. Some of those are related to bond setting and breaking in high-speed photochemistry and observation of liquid flow in living cells in the area of high-speed photobiology. Indeed, the developed circuitry can be applied to the study of any short lifetime phosphorescence that is responsive to shorter wavelengths of the optical spectrum. The development of UV LEDs has considerably improved the possibilities for these types of applications.

1.3 Objectives

- Review the physical structure of blue LEDs and theoretically determine the consequent electrical characteristics of the devices
- Take detailed measurements of the selected LEDs and create mathematical models of their behaviour
- Investigate the suitability of devices for nanosecond range pulsing
- Critically compare the new models with those existing in the literature
- Create models for the investigated LEDs, in both Matlab and Simulink, for subsequent optimisation
- Critically review the existing pulsing techniques in order to determine the current 'state of the art' and the most promising method for the intended improvements
- Identify the optimal electrical conditions essential for generation of the specified optical pulses based on a-priory principles as opposed to ad hoc methods
- Produce a prototype LED driver for scientific experiments that require optical pulses with FWHM of under $3ns$
- Produce a multiple output LED driver with the independent intensity control

1.4 Scope of the Thesis

LED development is reviewed. The LED theoretical and practical characteristics are investigated. The data is used for the LED modelling. The modulation limitations of those devices are considered. The pulse generation techniques are also reviewed and the most appropriate one is redeveloped to suit the proposed PMT calibration.

The main target of the thesis is the improvement of the optical pulse generating techniques for the LEDs operating at the blue end of the spectrum. The specific requirements include improvement in optical rise times of the emitted signal and the reduction of the pulse width. The optical pulse FWHM needs to be reduced to under $3ns$. The presented work is distinctive from other work in this area in a sense that the generated optical pulses provide a significant improvement in relation to the timing of the previously published results. A considerably more detailed theoretical underpinning of the operation of these devices and their drivers is developed.

The exact details of the results of the above work are explained in the following chapters of the thesis.

1.5 Contributions

- A comprehensive novel review of LED development to date is presented
- Some discrepancies between the experimental and theoretical LED characteristics are discovered and clarified
- New behavioural models for InGaN based heterostructure blue LEDs are developed
- The free running and externally triggered pulse generator, which is based on the theoretical underpinning of the driver and LED operation, is designed – it is exploitable in both optical and non-optical applications
- The switching speed of the developed optical driver offers a considerable improvement in relation to the speeds of the existing LED flashers
- A multiple optical output LED driver with the independent intensity control is developed

1.6 Thesis Structure

The thesis is broken into 7 chapters. The 6 chapters, which follow this one, are briefly described below.

Chapter 2 presents a review of the LED technological development from its discovery to the present day. It also considers various LED properties from theoretical perspective. These are expanded into a field of complex heterostructure LEDs used for high brightness outputs. The applications of the LEDs are also included.

Chapter 3 presents a review of pulse generation techniques and their application to driving LEDs. This chapter together with the previous one forms a theoretical basis for the experimental work performed and described later, in Chapters 5 and 6.

Chapter 4 considers modelling techniques and is a basis for the modelling of the complex LED structures described in Chapter 5.

Chapter 5 describes the majority of investigative and modelling work performed. It focuses on results obtained from measurements on blue LEDs.

Chapter 6 presents implementation of theoretical and investigative knowledge described in the previous chapters. It focuses on experimental work carried out with the aim of developing a successful flashing generator that would produce blue optical pulses with FWHM of under $3ns$.

Chapter 7 draws conclusions on the relevant findings of this research. It also provides recommendations for future work, which may lead to the additional development in the area.

Chapter 2

The Light Emitting Diode

Theoretical understanding of the LEDs is essential when designing fast pulsing circuits that employ these devices as the light sources. An LED is a special type of semiconductive diode that emits incoherent light when it is forward biased. This electroluminescence effect was not fully utilised until long after its discovery. The successful search for more adequate materials and technologies helped the transformation of the devices from their primitive form in the 1960s to the present day ultra-bright emitting devices. This development will most certainly continue up to the point when these devices become the primary lighting source. The technological advances, covered in Section 2.1, provide an insight into the reasons and events that resulted in today's devices. Present LED material properties are a result of the historic material development. It is very likely that the LED structure would differ from what it is at the present had the materials technology taken a different path in the past. The relevant electrical and optical properties of LEDs are reviewed in the Section 2.2. These provide background for the work described in the future chapters. Section 2.3 looks at the construction of advanced LED structures. These are relevant as the LEDs investigated in this case are heterostructure type devices and their structure differs from that of the homojunction devices. Consequently, there are some differences in the physical attributes of the two groups of the devices. Section 2.4 briefly touches upon the common uses of the LEDs today. These applications are the main drivers for the development of the devices, so it is very likely that the advances in the LED technology will continue to provide more efficient devices. The lighting industry steers the technology towards the generation of devices with ultra bright optical output. It is reasonable to believe that the other applications ought to benefit from this continual development.

2.1 LED Development

The structure and the characteristics of the modern LEDs are largely determined by the historic development of the semiconductor materials. This development, described

in Section 2.1.1, informs about the issues with the manufacture of these devices. Some of the subsequent device characteristics are investigated in later chapters in order to confirm that blue LEDs can be used in the proposed high switching applications.

2.1.1 Present devices

The phenomenon of electroluminescence was discovered by Henry Joseph Round in 1907 while experimenting with Silicon Carbide (SiC - carborundum) [20]. Round detected that the SiC crystals emit dim yellow light when exposed to a potential (in order of few volts). The poor light intensity, as well as the difficulties experienced with handling Silicon Carbide, weakened the research activities in this area. There were numerous other attempts to developing electroluminescence, but all were of limited success in terms of light emission. All the experiments were based on SiC or ZnS (Zinc Sulphide). These attempts failed to result in development of a device with significantly noticeable output light intensity. The indirect bandgap nature (see Figure 2.4 in Section 2.2.2) of the SiC was the main reason for this inability to fabricate high power LEDs.

In 1962, Nick Holonyak, of then General Electric Company laboratory in New York, made a breakthrough in discovery of electroluminescence while creating very simple devices from silicon, germanium and III-V materials [21]. Other researchers were also experimenting with LEDs. Hall, Nathan and Rediker were attempting to develop LEDs at the same time. They had an early lead in terms of facilities and were working with good-quality ready-made GaAs. Holonyak produced his own materials. He used an alloy of Gallium Arsenide Phosphide created in (what was then considered as) a rather unconventional method. He heated GaAs and GaP with a metal halide in a closed ampoule to create a mixed crystal. For the chemists at the time, this was considered as an absurd and impossible method of developing crystals. The conventional method involved slow replacement of As atoms by P atoms. This is achieved by heating GaAs in phosphorus gas. Holonyak continued with his method. This 'disadvantage' played a major role in development of visible LEDs. Though both materials, Gallium Arsenide and Gallium Arsenide Phosphide, were used in a similar manner to create LEDs the advantage of this alloy was its larger band gap, which meant that the final result was red, as opposed to infrared light. The luminous intensity of the GaAsP and GaP LEDs was quite poor ($10^{-3} - 10^{-2} cd$ at $20 mA$). As a result, these devices were employed mainly as indicators. Apart from developing the first LED that emits visible light, Holonyak also showed that an alloy could be used to create a usable semiconductor device. This invention led to the progress of the present heterostructure devices.

Research into the LED and manufacturing technologies was developing quickly. By the end of the 1970s additional colours of LEDs were available. The most commonly used materials remained GaP (red and green) and GaAsP (orange and yellow). The

production of LEDs rapidly increased with the development of a new material - AlGaAs. It allowed tenfold increase of the luminous output due to better efficiency and multi-layered heterojunction construction. Despite the achieved progress, the new LEDs had relatively high failure rate limiting the benefits achieved from the newly available colours. The majority of the used devices were still the ones that operated in the red end of the spectrum.

Advancing laser diode technology was a great source of manufacturing ideas for the progress of LEDs. This resulted in production of red, orange, yellow and green LEDs with the use of a single technology. A major outcome was an increase in reliability of the final products. These employed AlInGaP for their active semiconductive layer. The same material was used in subsequent research aimed at an increase in the luminous intensity of blue LEDs. Toshiba, at the time one of the leading LED manufacturers, introduced a new method of LED growth using Metal Organic Chemical Vapour Deposition (MOCVD) process. The devices created using this new method were capable of transferring over 90% of the internally generated light to the outside of the package.

In order to expand and complete the visible spectrum emissions the research focused on developing a reliable blue LED source. The result was an extensive search for new materials and technologies that would fulfil the requirement for blue LEDs. The majority of this research was focused on investigation of II-VI material properties. However, the efficiency and reliability of the produced devices was extremely poor; they would degrade within few tens of operating hours. Research into II-VI compound based light emitters had not to date yielded a viable commercial product [22]. Even though the II-VI compounds can relatively easily be grown in high quality crystal form (almost as easily as GaAs) with relatively negligible amount of crystal imperfections, the fact that they are grown at relatively low temperatures is demonstrated in their rapid failure. It was experimentally proved that the relatively low manufacturing temperature is the cause for the material to become brittle.

In 1969 Maruska and Tietjenstarted initiated a revolution in development of blue LED materials when they succeeded in growing single crystalline GaN on sapphire substrate by hybrid vapour phase epitaxy (HVPE) [23, 24]. This paved the path for further developments in GaN crystal growth. Sapphire was the first and so far only successful material that was found to be suitable for this purpose. It was also found that the newly manufactured GaN film has direct transition-type band structure, qualifying it for a potential LED source material. Blue light was emitted for the first time from an LED in 1971. This was not pure electroluminescence as the luminescence of GaN was excited with an UV laser [25–27]. More similar attempts were reported a year later by Maruska *et al.* [24, 28] and Dingle *et al.* [29]. The LED based on GaN was very inefficient. This was caused by problems relating to fabrication of sufficiently high quality crystalline layers and realisation of p-type doping [22, pp13]. Undoped

GaN films are always highly conductive n-type materials. This is caused by native imperfections such as nitrogen vacancies and Gallium Interstitials (empty sites in the crystal lattice or an atom in a normally-empty space). Both of these act as donors. The GaN films were doped with group II elements such as Zn. The results of such doping are semi-insulating materials. Those materials are then used as a replacement for p-type GaN. Hence devices with poor efficiency are formed. Consequently, the reported LEDs were Metal-Insulator-Semiconductor (MIS) devices, not the p-n junctions. Facing these technological difficulties made the vast majority of researchers in the field neglect GaN as a material that would be useful for further development of LEDs.

One of the very few scientists who still believed in properties of the GaN was Professor Akasaki (Nagoja University, Japan). Inspired by the previous success of Pankove *et al.* [25], Akasaki continued the struggle to develop GaN as a potential base material for LEDs. The team did not succeed in commercialising any of their newly manufactured LEDs due to poor efficiency and unreliable biasing requirements (threshold voltage from few volts to $10V$ [24]). However, they did make limited progress from manufacturing perspective. The use of x-ray diffraction patterns of GaN films showed that the films consisted of many mosaic crystallities with various orientations. Single crystal films of high quality were yet to be manufactured. The reasons for the inability to fabricate such films were large lattice mismatches and large difference in thermal expansion coefficients of the base and the active layer [30]. A particularly important manufacturing improvement was achieved by Akasaki's team in 1986. They demonstrated that the surface morphology of the GaN single crystal films was improved by prior deposition of a thin Aluminium Nitride (AlN) buffer layer before the growth of GaN by Metal-Organic Vapour Phase Epitaxy (MOVPE) [31, 32]. The idea of an AlN buffer layer came from earlier attempts to grow GaN on AlN coated sapphire substrates. This was done using a different growth technique (Molecular Beam Epitaxy) [33]. The buffer layer minimises creation of the orientation fluctuation of the active layer crystal molecules. This in turn decreases the effects of the deep level defects. Consequently, both the electrical and optical properties of GaN films grown on sapphire were improved [30].

One of the assumed key steps required to improve efficiency of MIS diodes would involve the development of InGaN films [34]. These films would allow the production of p-type material necessary for development of efficient LEDs. Osamura *et al.* had reported fabrication of such compound [35] with the confirmation of the results reported by Nagatomo *et al.* [34]. Nagatomo *et al.* also proved the dependence of the film morphology on the substrate ambient temperature during the growth process. They also proved a dependence between energy band gap of InGaN films on the In/N ratio by showing that the direct energy band gap in the $In_xGa_{1-x}N$ compound is inversely proportional to the composition x for a fixed manufacturing temperature. It was shown

that it is possible to control the emitted wavelength simply by controlling the ratios of substances used to form the compound.

Akasaki's team eventually succeeded in developing a p-n junction capable of emitting UV light under laboratory conditions [36]. The p-type material was manufactured indirectly by low-energy electron beam irradiation (LEEBI) treatment of Mg doped GaN film. Both Zn and Mg doped GaN change their optical properties after such treatment, but it is only GaN:Mg that loses its resistivity dramatically, showing p-type conduction. It took a short time for the p-n junction to be optimised and the first observation of the GaN optical emission was reported at room temperature. Even though the emission was stimulated optically with a N_2 pulsing laser light, a clear path was set for the current stimulated diodes - both Laser Diodes (LD) and LEDs.

Akasaki's research played a major role in the success of Shuji Nakamura of Nichia in development and commercialisation of bright blue light sources. Nakamura succeeded in solving the problems of GaN crystal growth and p-type doping. His research into blue LED commenced in 1989. A year later, MOCVD that was already in use by LED manufacturers was the object of Nakamura's further interest. He improved the MOCVD method aiming to grow high quality single crystal GaN layers [37]. Nakamura developed new 'Two Flow' Metal-Organic Chemical Vapour Deposition (TF-MOCVD) [38–41]. The previously used MOCVD method relied on fast flowing reactive gas, which flows parallel to the sapphire substrate. Close inspection of the grown GaN films revealed insufficient coverage of the substrate area. For that reason, Nakamura introduced another gas sub-flow consisting of nitrogen (N_2) and hydrogen (H_2) with the direction perpendicular to that of the main reactant gas. The aim of the sub-flow is to control direction of the main flow in order to bring the reactant gas into contact with the substrate [39, 40]. Nakamura also confirmed previously reported benefits of the AlN buffer layer deposited between the sapphire substrate and the GaN film. The TF-MOCVD was soon employed for growth of GaN films on GaN buffer. The buffer was deposited at lower temperature. This was followed by GaN film growth at higher temperature resulting in highest quality GaN films at the time [40]. Most importantly, it is the electrical, rather than optical characteristics of the GaN films that were improved when using the GaN buffer layers. This major improvement gave Nakamura a reason to further investigate a possibility of using the GaN for ultra-bright blue LEDs.

However, Nakamura knew that previously developed films have hole concentration and resistivity properties that would not allow successful production of ultra-bright LEDs. Inspired by the work done by Akasaki's team in this area, Nakamura closely followed their footsteps constantly improving the methods they had already developed. In 1991, he reported first p-type GaN material, which was highly doped with Mg. This was the first discovery of 'as grown' GaN material that shows p-type material properties

with no exposure to LEEBI treatment. The new p-type material was superior to the previously reported ones in terms of conductivity control and hole mobility. However, its resistivity was still prone to fluctuations [40–42]. The material was then treated using the LEEBI method resulting in remarkable results in terms of hole concentration and resistivity. However, the LEEBI treatment produces relatively thin layers of material with maximum thickness of $0.35\mu m$. The researchers continued improvement of the LEDs using the same manufacturing method. This resulted in first p-n junction high-power blue LED suitable for practical use [42]. Its external quantum efficiency (0.18%) is better than that of then conventional SiC blue LED. Also the output power was enhanced by factor of ten. The new LEDs also had lower forward voltages ($4V$) at operating current ($20mA$). Despite the success, there was still room for blue LED improvement, especially in the area of crystal growth and p-type physical properties. One of the major disadvantages with the manufacturing techniques was the inability to develop thick layers of p-type material. This is because the low resistivity region of the Mg doped GaN depends on the penetration depth of incident electrons of the LEEBI treatment. Apart from the absence of p-type layers thicker than $0.35\mu m$ another disadvantage of LEEBI treatment was that its principles were not understood, even though its effect was applied to conversion of poor quality p-type materials into films with high hole concentration and mobility. The same type of conversion of poor quality p-type material into films suitable for creation of high-power LEDs was soon discovered to be possible with the use of high temperature annealing [43, 44]. It was found that the thermal annealing, regardless of chosen temperature, does not cause any change in the surface morphology of the Mg doped GaN material exposed to it. The temperatures to which the films are exposed should be higher than 700°C in order to obtain $4\mu m$ thick p-type films of low resistivity ($2-8\Omega cm$). However, in the same way as the LEEBI treatment mechanisms were not understood, the thermal annealing treatment was also a mystery to the scientists. Later observations showed that the LEEBI treatment and thermal annealing operated on the same principle. This was based on rearrangement and removal of the doping acceptor H-neutral complexes and was dependant on temperature applied to the films exposed as well as on the gas used to perform the treatment [44, 45]. The H neutral complexes are areas where acceptor atoms are neutralised by H atoms when hydrogen gas is incorporated in the material. This occurs during hydrogenation process while p-type film is being manufactured. N_2-ambient thermal annealing can remove atomic hydrogen from the acceptor-H neutral complexes, thus reducing the resistivity of the p-type Mg doped GaN films. Throughout the improvements in p-type material, the production of n-type GaN material was not altered. There was no need for this as the originally used method was proven to be successful (using Si or Ge as GaN dopants) [46].

Research into the suitability of other types of materials, which could possibly result

in creation of ultra bright blue LEDs, continued in parallel with the research into GaN. Even though the majority of scientists concentrated on II-VI materials for a long time no reliable device was manufactured. Limited success was achieved in early 1990s when Xie *et al.* reported a practical usable blue LED based on Zn(S, Se) elements [47]. An attempt to develop InGaAlN with the aim of its application to short wavelength optical devices resulted in production of InGaN compound at high temperature using MOVPE [48]. The experiments also help demonstrate the photoluminescence properties of the material. Nakamura, once again, adopted ideas from other scientists and created p-n junction LED based on InGaN as active material grown on sapphire with GaN as a buffer layer [49]. Nakamura's previous experience with buffer layer made of GaN played a major role in this development. Soon afterwards, he reported improvement in blue LED light intensity by factor of 36 [50]. The improvement was possible due to the use of Si doped InGaN instead of using undoped InGaN. The light intensity of the new LED had twenty times the output of Mg doped GaN that was already in practical use.

Nakamura believed that to obtain high-performance optical devices the use of double heterostructure is required. It was already reported that InGaN could be used in the creation of double heterostructure [51]. Researchers were facing a restricted choice of materials for double heterostructures as the only high performance p-type material that would be suitable for such combination with InGaN is GaN. Hence, the first blue LED based on double heterostructure consisted of p-GaN/n-InGaN/n-GaN. The output power and external quantum efficiency of such LED was twice as high as of the II-VI blue LEDs [51, 52]. Another attempt to investigate double heterostructure device properties employed AlGaN/GaInN combination [53]. Violet emission was observed, but it was optically stimulated. However, the results confirmed a possibility for use of the III-V materials for construction of short wavelength optical devices. Almost simultaneously, Nakamura performed similar type construction of InGaN/AlGaN double heterostructure LED and obtained blue output light with intensity of over $1cd$ for the first time [54]. The doping material used to fabricate these devices was Zn. This change of the doping material in combination with the use of very thin active layer soon allowed development of ultra-bright ($4cd$) blue and green LEDs [55]. The importance of the thin active layer was proved later when it was shown that the photoluminescence efficiency strongly depends on well width (the thinner the well width, the better the efficiency) [56]. Poor external quantum efficiency of conventional green LEDs stimulated research into use of III-V compounds for longer wavelengths. InGaN was considered as inappropriate material for yellow light emission because the physical properties of the compound negated such emission. The emission wavelength of the material is controlled by the In concentration in the compound. In order to produce yellow light, the amount of In in the material is reduced so much that the alteration of the active material structure causes dramatic reduction in the output power - eliminating InGaN

as a possible source of yellow light. Nakamura dramatically decreased the thickness of the active layer in order to achieve high power emission at shorter wavelengths. The new green LEDs peaked at $525nm$ instead of yellowish-green $555nm$ peak achieved by the conventional GaP green LEDs. The efficiency of the new green LEDs was also improved in relation to GaP LEDs [55]. Yellow light emission was also achieved. Using similar techniques, the blue and violet LEDs were developed [57]. Further development of the manufacturing technique contributed to creation of a $12cd$ green LED [58]. This achievement made the idea of full-colour display reachable. This could be realised by combination of ultra bright InGaN single quantum well (SQW) blue and green LEDs with GaAlAs red LED. The techniques used to manufacture blue LEDs were soon applied in development of Laser Diodes [59, 60]. Gradually the idea of multi quantum well (MQW) LEDs became a norm for III-V compounds. The thickness of the active layers was kept minimal in order to create ultra-bright output.

The development of manufacturing techniques and material development continued through mid-90s, but were all based around the same materials - III-V compounds, mainly InGaN and AlGaN. The materials were getting more and more sophisticated so that they could be used to emit light in almost whole of the visible spectrum. This was proven when a high efficiency Amber InGaN-Based LED was reported in 1998 [61]. The LED did not only match the already available AlInGaP amber LEDs in terms of light intensity, but has shown an ability of being used in harsher environments without expressing any significant dip in its performance. The output power of such LED remains constant when the ambient temperature increases from room temperature (20°C) to 80°C [61] demonstrating material robustness. Similar results were obtained for the red LED based on the InGaN compound in 1999 [62]. The amber and red LEDs were proven to have improved external quantum efficiency for higher currents when Epitaxially Laterally Overgrown GaN (ELOG) Substrates are used [63, 64].

The visible spectrum was covered by InGaN LEDs. The search for white LED and its commercialisation were completed in 1996 when a blue LED chip was combined with yellow phosphor [22]. There are various white LEDs available today based on the same principle of combining (blue or UV) LED and photoluminescence [65, 66]. UV LEDs were also developed by Akasaki's team in 2003 [67]. As a next promising device, high efficiency UV-LEDs using AlGaN base layer with low dislocation density have been demonstrated [68].

The recent development of the LEDs is dependant on epitaxial growth advances in semiconductor technology [69]. No radical changes in LED technology have been reported since the end of 1990s. However, the development has continued resulting in constant improvements in terms of LED efficiency and brightness [67, 70–73]. It has become a standard to manufacture double heterostructure (DH) and MQW LEDs because of the significant increase of device brightness brought in by these techniques.

Another perspective alternative for GaN devices may be the use of rare earth dopants (Eu, Er and Tm) [69]. GaN films doped with these elements emit pure red, green and blue emission colours [74]. Some white light generating devices are also achievable without the use of phosphorus or colour mixing [75]. The current commercially available LEDs provide optical output of up to $5W$ [76].

2.1.2 Future Devices

These devices are not studied to a great depth here because they are still in their early stages of development. They are covered with the intention of indicating the probable future developments in the field.

Nanotubes

Carbon nanotubes are components whose material structure is based on cylindrical carbon molecules. They might take the future development of LEDs in a previously unimaginable direction. This sort of technology, if successful will enable smaller and faster electronic devices with increased functionality. The nano-diode is one of the smallest functioning devices ever made. The carbon nanotube devices are capable of performing multiple functions - as a diode and two different types of transistors. This property should enable such devices to both emit and detect light [77–80].

The way these devices operate depends not on their impurities (they do not have any that are deliberately introduced), but on the electric field used to "program" the devices. They are exposed to electric field in order for p and n type regions to be formed. This is achieved using the split gate coupling positioned underneath the tubes. The two coplanar gates couple to the two halves of a carbon nanotube. Gate biasing allows formation of a p-n junction. Non-fixed doping implies changeable polarity. The material properties of carbon nanotubes should enable the device to function as an LED. The light emission occurs when the electrons and holes are injected at the opposite ends of the channel. A localised emission point, where the two types of carriers recombine, is formed in the tube. The position of this point is controlled by the gate bias [81]. The emitted light is strongly polarized along the tube axis and the radiation energy depends on the physical characteristics of the device [81].

Organics

The organic light emitting diodes (OLEDs) were originally demonstrated in 1965 [82]. The main advantages of the invention were improved operation over a long period of time and reduction of the optical decay time. The fabrication of the OLEDs is simpler than the manufacture of the organic phosphors. The devices were also less dependent on the straight control of the impurity concentration. The design improvements in 1982

resulted in, at the time, high luminescence efficiency at relatively low bias conditions [83]. The devices were further improved in 1990s when a conducting polymer LED was developed [84]. The OLEDs were commercialised in 1997 by Pioneer Electronics [85]. Since then the interest into the devices is driven by their potential application in flat panel displays [86–88].

The basic structure of the devices consists of two charged electrodes that enclose organic light emitting material [85, 86] as shown in Figure 2.1. The organic material is normally deposited in thin layers. A basic two-layer diode uses one organic layer to transport holes and the other organic layer to transport electrons [87]. The electroluminescence is achieved when the two types of carriers recombine at the interface between the two layers. A number of organic layers with a variety of impurities is introduced when a higher efficiency is sought. The recombination probability is increased with the heterostructure arrangements.

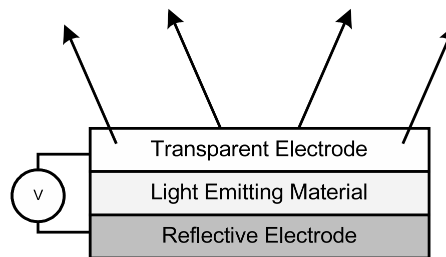

Figure 2.1: Organic LED structure

A major advantage offered by this sort of arrangement is that the need for bulky and environmentally unfriendly mercury lamps (as in Liquid Crystal Displays - LCD) is removed as these devices are self-luminous [88]. Consequently these are low power consumption displays, which are also more compact and adaptable than their LCD counterparts. These more efficient displays are also beneficial in terms of thermal and electrical interference.

There are passive and active OLED displays. Passive displays are simple OLED matrices activated by the drivers in such a way that the current is passed through selected OLEDs. External drivers select the specific rows and columns of the matrix. The frequency of the frames is approximately $60Hz$. The simple array matrix structure of this sort of arrangement allows easy manipulation of the display panel shape and size. The active displays use integrated electronic back plane, which is responsible for selection of individual OLEDs (and hence pixels). The duration of a pixel's on or off time is arbitrary of the frame time i.e. each pixel can remain in its desirable state for either a single frame or as many frames as required. This feature is possible because of the use of Thin Film Transistors (TFT) and capacitors incorporated in the active back plane.

A particular interest lies in development of white OLEDs because of their potential

application in full colour displays and general illumination. The luminous efficiency of these devices is comparable to that of the incandescent light sources, but is still seven times less than that of fluorescent light sources [89]. An obstacle that is yet to be overcome by this technology is the degradation of these devices. Further developments are expected to follow in the field.

2.2 LED Characteristics

The behaviour of the carriers in the semiconductors and their junctions is reviewed. These physical parameters define the electrical and optical characteristics of the LEDs. These characteristics are crucial for the success of the development of the LED drivers. Slow and inadequate LED frequency response can result in lack of optical pulses even though the driving signal is considered to be suitable in general terms. The consideration of the LED behaviour as predicted by theory also contributes to the analysis of the experimental data in Chapter 5.

2.2.1 Charge Properties

At thermal equilibrium the carriers inside a semiconductor conduction band move in a random manner. However, over a period of time, net displacement as a product of the random motion is non-existent.

Application of the electric field to the semiconductor sample engages an additional force onto randomly migrating carriers. Despite being influenced by the collisions inside the material, the velocity increments created by the electric field are all in the same direction. This additional velocity component called *drift velocity* results with a *drift* as a net effect. The drift velocity for electrons and holes are defined in Equations 2.1 and 2.2 respectively

$$v_n = -\mu_n \varepsilon \tag{2.1}$$

$$v_p = \mu_p \varepsilon \tag{2.2}$$

where v_n and v_p are average electron drift velocity in conduction band and average hole drift velocity in valance band respectively, μ_n and μ_p are electron and hole mobilities respectively and ε is the applied electric field.

The net current generated by the applied electric field is called *drift current*. The density of this current due to electrons is the product of the total electron charge and electron drift velocity, as defined in Equation 2.3

$$J_{n(drift)} = \frac{I_n}{A} = \sum_{i=1}^{n}(-qv_i) = -qnv_n = qn\mu_n\varepsilon \tag{2.3}$$

where I_n is the electron current through the semiconductor sample, A is the cross-sectional area of the sample and $(-q)$ is the elementary charge. The summation is executed over a unit volume (m^3).

The same principle applies to the drift current caused by the migration of holes, as shown in Equation 2.4.

$$J_{p(drift)} = qpv_p = qp\mu_p\varepsilon \tag{2.4}$$

The total current generated by the electric field is the sum of the currents carried by the electrons and holes.

$$J_{drift} = J_{n(drift)} + J_{p(drift)} = (qn\mu_n + qp\mu_p)\varepsilon \tag{2.5}$$

An additional manifestation of the charge carrier motion is diffusion. It appears when the mobile carriers are not uniformly distributed in a material. Under such conditions, the carriers move from region of high concentration to region of low concentration cancelling the imbalances of carrier concentration. This results in a diffusion current. The amount of this generated diffusion current depends on diffusion coefficient defined in Equation 2.6

$$D_{n/p} = v_{th}l \tag{2.6}$$

where v_{th} is carrier thermal velocity and l is a mean free path. Those two quantities are related as shown in Equation 2.7

$$l = v_{th}\tau_c \tag{2.7}$$

where τ_c is the mean free time. The mean free path and time describe the distance and the time taken for a minority carrier to travel in a semiconductor before it is annihilated through carrier recombination processes. The diffusion currents in a sample with n or p carriers diffusing in the x direction are defined in Equations 2.8 and 2.9. The total electric current produced by the diffusion process is the sum of the currents carried by the electrons and holes, as shown in Equation 2.10.

$$J_{n(diff)} = qD_n\frac{dn}{dx} \tag{2.8}$$

$$J_{p(diff)} = -qD_p\frac{dp}{dx} \tag{2.9}$$

$$J_{diff} = q\left(D_n\frac{dn}{dx} - D_p\frac{dp}{dx}\right) \tag{2.10}$$

When the carrier concentration gradient and electric field are present simultaneously then both, drift and diffusion, currents will flow as shown in the current density equa-

tions, 2.11, 2.12 and 2.13.

$$
\begin{aligned}
J_n &= qn\mu_n\varepsilon + qD_n\frac{dn}{dx} && (2.11)\\
J_p &= qp\mu_p\varepsilon - qD_p\frac{dp}{dx} && (2.12)\\
J_{COND} &= J_n + J_p && (2.13)
\end{aligned}
$$

The diffusion coefficients are related to the carrier mobilities in that they are a measure of ease of carrier motion through the crystal lattice [92]. These constants are linked through Einstein's Relationship, Equation 2.14.

$$
D_n = \left(\frac{kT}{q}\right)\mu_n \qquad\qquad D_p = \left(\frac{kT}{q}\right)\mu_p \qquad (2.14)
$$

2.2.2 The P-N Junction

A p-n junction is formed when the p and n type semiconductors are merged together. This causes the large carrier concentration gradient and consequently carrier diffusion. The majority carriers diffuse to the other side of the junction leaving the immobile doping ions behind, as they are fixed in the lattice. As the negative and positive ions are left at the p and n side of the junction respectively, the corresponding space charges form near the junction. This space charge region forms an electric field pointing from the positive towards the negative charge (Figure 2.2).

With no external excitation being present, the drift current due to the electric field and the diffusion current due to the concentration gradient must exactly cancel each other. Comparison of the drift and diffusion currents results in the need for a constant Fermi level through the sample in order to satisfy zero net current (Figure 2.2). The Fermi level determines the energy at which the probability of occupation by an electron is one half. The need for constant Fermi level results in unique space charge distribution in the junction [90].

When the p−n junction is reverse biased, a very small current flows through. The reason is that only the minority carriers on each side have right polarities to carry current across the junction. Consequently, the minority carrier distribution is disturbed as the minority carriers are depleted from the junction. Similarly, the carrier injection, through either optical excitation or electrical bias, results with the change in the minority carrier density distribution. Because of the diffusion of minority carriers the changes in the minority carrier concentrations caused by a bias voltage are not localised at the edges of the depletion layer [91]. Instead, the minority carrier concentration has the spatially dependent variations as shown in the Figure 2.3 (rearranged from [90] and [91]), where the first letter in the carrier concentration denotes carrier type and the subscript denotes material type.

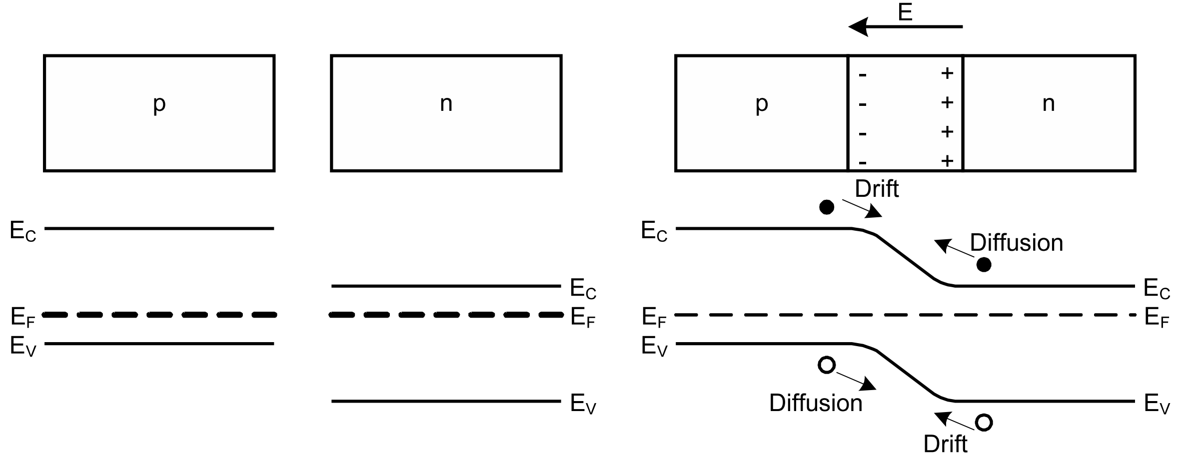

Figure 2.2: Energy band diagrams for doped semiconductors and a p-n junction

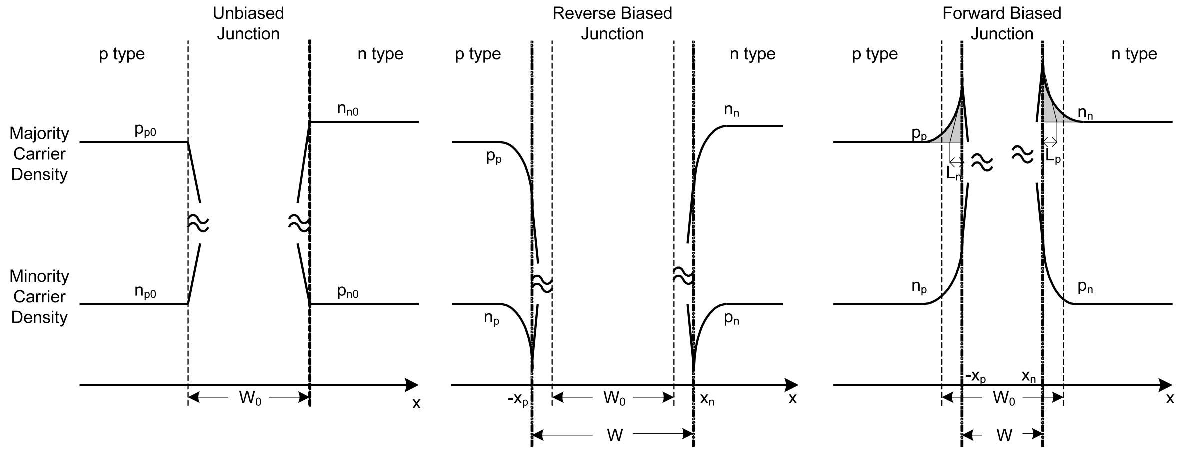

Figure 2.3: Majority and Minority Carrier Distribution

The spatially dependent variations of the minority carrier concentration across the diffusion regions are described by Equations 2.15 and 2.16.

$$n_p(x) - n_{p0} = n_{p0}\left[\exp\left(\frac{qV}{kT}\right) - 1\right]\exp\left(\frac{x + x_p}{L_n}\right) \tag{2.15}$$

$$p_n(x) - p_{n0} = p_{n0}\left[\exp\left(\frac{qV}{kT}\right) - 1\right]\exp\left[-\left(\frac{x - x_n}{L_p}\right)\right] \tag{2.16}$$

In the Equations 2.15 and 2.16 q is the elementary charge, k is Boltzmann's constant, T is temperature, L_n and L_p are minority carrier diffusion lengths defined in Equations 2.17 and 2.18.

$$L_n = \sqrt{D_n \tau_n} \tag{2.17}$$

$$L_p = \sqrt{D_p \tau_p} \tag{2.18}$$

In the Equations 2.17 and 2.18 τ_n and τ_p are the excess minority carriers' lifetimes. For

low carrier injection, those two lifetimes are comparable quantities [92]. The minority carrier lifetime is the inverse constant of proportionality that relates recombination rate to the carrier concentration. Thus, a short lifetime corresponds to a high recombination rate. During recombination the number of minority carriers in the sample decay exponentially. The minority carrier lifetime is the time constant that defines the decay [90].

Whenever the non−equilibrium is established the carriers attempt to achieve their respective equilibrium concentration. Contrary to the carrier generation process occurring during the reverse biasing, the mechanism that restores equilibrium following the injection of the excess carriers is the recombination of the excess minority carriers with the majority carriers. The nature of the recombination process determines the form in which the energy is released. This could be either in the form of radiating photons or phonon dissipation to the lattice. In order for a material to be utilisable for efficient photon generation its band structure needs to be direct [90]. Such semiconductors have no momentum difference between the minimum of their conduction band and the maximum of their valence band, as shown in Figure 2.4. This arrangement allows direct transition of an electron either upward or downward with no need to change its momentum. In contrast when an electron makes an indirect transition it has to absorb or emit a phonon, thereby exchanging energy and momentum with the crystal lattice, in order to complete the transition [91]. Recombination phenomena can be classified as direct and indirect process - each dominating in direct and indirect semiconductors respectively. LEDs and lasers require direct semiconductors for efficient photon generation [90]. Regardless of the recombination type, the net result of any recombination process is release of energy by an electron when dropping from a higher to a lower energy level.

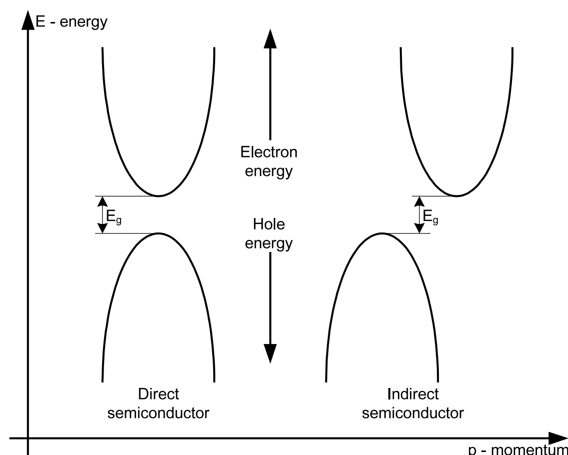

Figure 2.4: Simplified Energy-momentum diagram

2.2.3 Electrical Properties

Diode current and capacitance are considered as the most crucial electrical characteristics for the proposed application. The relationship between the current and voltage defines the amplitude of the driving signal required for successful light generation. The capacitance significantly affects the speed of the diode response. The theoretical consideration of the practical diode is included because of the experimental nature of the project.

Junction Current

The total potential generated by the space charge region (Figure 2.2) is called built in potential, v_{bi} and is defined in Equation 2.19.

$$v_{bi} = \frac{kT}{q} \ln\left(\frac{N_A N_D}{n_i^2}\right) \tag{2.19}$$

As the majority carrier concentration equals the doping concentration at thermal equilibrium (i.e. $n_{n0} = N_D$ and $p_{p0} = N_A$), using the mass action law ($p_{p0} n_{n0} = n_i^2$) [90] Equation 2.19 is rearranged into Equation 2.20.

$$v_{bi} = \frac{kT}{q} \ln\left(\frac{p_{p0} n_{n0}}{n_i^2}\right) = \frac{kT}{q} \ln\left(\frac{n_{n0}}{n_{p0}}\right) \tag{2.20}$$

Assuming that the carrier densities at the boundaries are related to the electrostatic potential difference across the junction [90], Equation 2.20 can be rearranged into Equation 2.21 where V is the applied voltage. The sign of the applied voltage is positive for the forward bias and negative for the reverse bias.

$$n_n = n_p \exp\left[\frac{q\left(v_{bi} - V\right)}{kT}\right] \tag{2.21}$$

Minority carrier densities at the boundaries of depletion layer can be obtained (2.22 and 2.23) from the Equation 2.20 considering the low-injection condition for which the number of injected minority carriers is much smaller than the majority carrier density ($n_n \approx n_{n0}$ and $p_p \approx p_{p0}$) [90].

$$n_p - n_{p0} = n_{p0}\left[\exp\left(\frac{qV}{kT}\right) - 1\right] \tag{2.22}$$

$$p_n - p_{n0} = p_{n0}\left[\exp\left(\frac{qV}{kT}\right) - 1\right] \tag{2.23}$$

Using the Equations 2.22 and 2.23 the hole and electron currents at the boundaries can be defined by Equations 2.24 and 2.25 where the diffusion coefficients, $D_{n/p}$, are

defined by Equation 2.6 and the diffusion lengths, $L_{n/p}$, are defined by Equations 2.17 and 2.18. It follows that the diffusion currents fall exponentially with the diffusion lengths. The total current in the device must be constant and it is equal to the sum of the two current components (Equation 2.26).

$$J_p(x_n) = \frac{qD_p p_{n0}}{L_p}\left[\exp\left(\frac{qV}{kT}\right) - 1\right] \tag{2.24}$$

$$J_n(-x_p) = \frac{qD_n n_{p0}}{L_n}\left[\exp\left(\frac{qV}{kT}\right) - 1\right] \tag{2.25}$$

$$J = J_p(x_n) + J_n(-x_p) \tag{2.26}$$

Incorporating Equations 2.24 and 2.25 into Equation 2.26 results with the total ideal diode current density relationship shown in Equation 2.27. J_s is the saturation current density with its value being defined in Equation 2.28.

$$J = J_s\left[\exp\left(\frac{qV}{kT}\right) - 1\right] \tag{2.27}$$

$$J_s = \frac{qD_p p_{n0}}{L_p} + \frac{qD_n n_{p0}}{L_n} \tag{2.28}$$

As $I = JA$, $I_s = J_s A$ and the specified area is fixed then the ideal diode current is defined by Equation 2.29.

$$I = I_s\left[\exp\left(\frac{qV}{kT}\right) - 1\right] \tag{2.29}$$

This section highlights the standard semiconductor theory relevant to the application. The deviations from the ideal theoretical characteristics are considered in the following section.

Deviation from Ideal Characteristics

The ideal diode equation (Equation 2.29) describes current voltage characteristic for p-n junction diodes at low current densities [90]. A more realistic solution to diode current-voltage characteristic includes an ideality factor η, the voltage drop across its internal resistance R_s and current flow through diode parallel resistance R_p. The result is a more realistic diode equation (Equation 2.30). This equation can be rearranged into Equation A.26, so that diode current is the subject of the equation (as shown in appendix A).

$$I = I_s\left\{\exp\left[\left(\frac{q(V - IR_s(V))}{\eta kT}\right)\right] - 1\right\} + \frac{V - IR_s(V)}{R_p(V)} \tag{2.30}$$

The ideality factor takes into account the generation and recombination processes in the depletion layer of a diode. These are ignored in the ideal diode equation due to

an assumption that neither of those two processes occurs in this region. Theory shows the value for the ideality factor lies between 1 and 2 [91, 93]. A detailed analysis shows that the ideality factor tends to being equal to 2 at high injection levels [91]. However, in practice the ideality factor can be higher than this theoretically predicted value [94]. It can be as high as 7 when considering GaN based diodes [95].

Ideally the series resistance should be zero. However, in practice it appears as a product of the resistance of the neutral regions and internal contact resistance [96]. The value of the series resistance for a particular diode can be established from Equation 2.31. The derivative needs to be taken at the voltages significantly larger than the diode threshold voltage where the slope of the I-V curve is relatively constant.

$$R_{s,p}(V) = \frac{dV}{dI} \tag{2.31}$$

The parallel resistance is an outcome of any conduction channel that bypasses the p-n junction. This is normally a consequence of damaged regions and surface imperfections [96]. To find the value of the parallel resistance the relationship shown in Equation 2.31 is also valid. In this case the derivation is performed in the reverse bias section of the I-V characteristic. Ideally the parallel resistance should be infinitely high. Apart from controlling the slope of the diode I-V characteristic in the reverse bias region, this resistance also affects the slope of the same curve at low forward bias voltages where the value of the parallel resistance is comparable to the diode dynamic resistance. The second term in the expression for the practical diode (Equation 2.30) represents the current flowing through the parallel resistance. It normally has negligible contribution in forward bias.

The I-V characteristic generated from the practical LED equation (2.30) is shown in Figure 2.5. Even though the plot might appear to be purely exponential it is in fact broken into distinctive exponential regions (as shown in Figure 2.6). The diode current follows the parallel resistance current at reverse bias and low forward bias. It then behaves according to the rules described by the standard diode equation. At larger forward bias, the diode current asymptotically approaches the behaviour of the diode series resistance current. The regions and the way the plots are derived are described in appendix A in detail.

Capacitance - Voltage Relationship

The LED capacitance behaviour is important in the fast pulsing applications because this characteristic has a potential of preventing the generation of light. It was experimentally determined that some of the devices that fail to produce fast light pulses also have increased capacitance. There are two types of capacitance associated with a p-n junction: junction or depletion layer capacitance and charge storage or diffusion

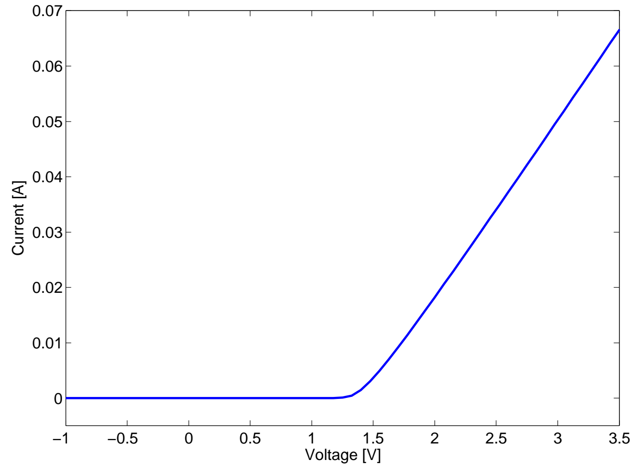

Figure 2.5: Practical LED I-V relationship

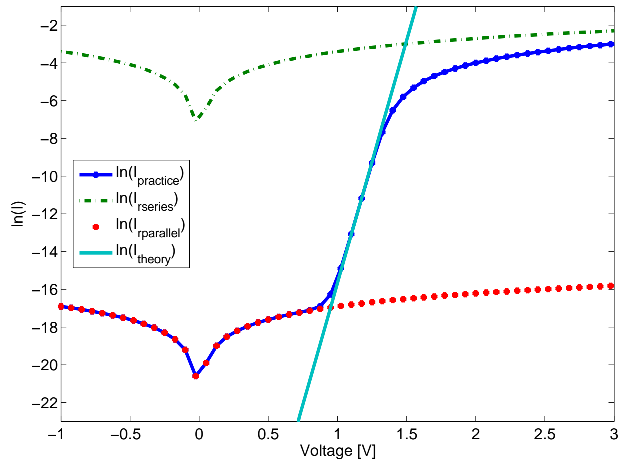

Figure 2.6: Practical LED ln(I)-V relationship (scale arbitrary)

capacitance.

The depletion layer holds negative space charges on the p side and positive space charges on the n side [91]. The dipole that is the result of this charge storage distribution causes the junction depletion layer capacitance [97]. The depletion capacitance per unit area is defined as the rate of change of depletion layer charge per unit area, dQ, with respect to change of the applied voltage, dV, (Equation 2.32).

$$C_j = \frac{dQ}{dV} \qquad \text{(per unit area)} \tag{2.32}$$

Increasing the reverse bias voltage across the p-n junction results in increment of the depletion layer width, W (see Figure 2.3). The incremental space charges on the n and p sides of the depletion layer are equal, but with opposite charge polarity, thus maintaining overall charge neutrality. This incremental charge causes an increase in the electric field by an amount defined by Equation 2.33 where ϵ_S is semiconductor

dielectric permittivity [90].

$$d\varepsilon = \frac{dQ}{\epsilon_S} \tag{2.33}$$

Thus Equation 2.32 can be developed into Equation 2.34.

$$C_j = \frac{dQ}{dV} = \frac{dQ}{W\frac{dQ}{\epsilon_S}} = \frac{\epsilon_S}{W} \qquad => \qquad C_j = \frac{\epsilon_S}{W} \tag{2.34}$$

The expression for the depletion capacitance per unit area (Equation 2.34) is identical to the standard expression for a parallel plate capacitor. The spacing between the two plates represents the depletion layer width. The equation is valid for any arbitrary impurity distribution.

For one sided abrupt junction, the junction width is defined as shown in Equation 2.35.

$$W = \sqrt{\frac{2\epsilon_S(v_{bi} - V)}{qN_B}} \tag{2.35}$$

Combining Equation 2.35 into Equation 2.34, the junction capacitance expressed in terms of applied voltage and material properties can be found (Equation 2.36) and it can be rearranged into Equation 2.37.

$$C_j = \sqrt{\frac{q\epsilon_S N_B}{2(v_{bi} - V)}} \tag{2.36}$$

$$\frac{1}{C_j^2} = \frac{2(v_{bi} - V)}{q\epsilon_S N_B} \tag{2.37}$$

The Equation 2.36 allows the use of plot of C_j^{-2} versus V for experimental determination of the material properties from a ready made device. The plot produces a straight line for a one sided abrupt junction. The slope gives the impurity concentration N_B of the substrate and the intercept (at $C_j^{-2} = 0$) gives built in voltage, v_{bi} [90]. Similar equations can be developed for the linearly graded and the parabolic junctions.

To derive Equation 2.37 it is assumed that the only variation of the space charge in the depletion layer contributes to capacitance. This certainly is a good assumption for the reverse bias condition. For forward bias, however, the applied voltage effectively reduces the built in potential and hence the built in field which prevents excessive diffusion. A large current, in the form of excess minority carrier, can flow across the junction corresponding to a large number of mobile carriers present within the neutral region. Once injected, the minority carriers recombine with the majority carriers and decay exponentially with the distance. These minority carrier distributions lead to current flow and to charge storage in the p-n junction [90]. The storage of these mobile carriers in diffusion region with respect to the biasing voltage contributes to an additional term, called the diffusion capacitance.

The number of stored minority carriers depends on the diffusion length and the charge density at the boundary of the depletion region. The charge of the stored minority carriers can be found by integrating the excess carriers in the neutral regions. These are represented by the shaded areas in Figure 2.3. The stored charges per unit area are defined in the Equations 2.38 and 2.39.

$$Q_n = qL_n n_{p0}\left[\exp\left(\frac{qV}{kT}\right) - 1\right] \tag{2.38}$$

$$Q_p = qL_p p_{n0}\left[\exp\left(\frac{qV}{kT}\right) - 1\right] \tag{2.39}$$

The stored charge can also be expressed in terms of the injected current. The amount of the stored charge is the product of the current and the minority carrier lifetime (Equations 2.40 and 2.41).

$$Q_n = \frac{L_n^2}{D_n} J_n(x_p) = \tau_n J_n(x_p) \tag{2.40}$$

$$Q_p = \frac{L_p^2}{D_p} J_p(x_n) = \tau_p J_p(x_n) \tag{2.41}$$

The same relationship from Equation 2.32 is used to define the diffusion capacitance. However if the junction area is to be considered (Equation 2.42), then the diffusion capacitance is expressed as show in Equation 2.43.

$$C_d = A\frac{dQ_p}{dV} \tag{2.42}$$

$$C_d = \frac{Aq^2 L_p p_{n0}}{kT}\exp\left(\frac{qV}{kT}\right) \tag{2.43}$$

Under reverse bias, the diffusion capacitance becomes inconsequential because of the negligible minority carrier storage.

2.2.4 Optical Properties

Had the electroluminescence effect in the LEDs been an instantaneous process with 100% efficiency, it could have been said that the LEDs operation depends on their electrical characteristics only. However, the practical limitations are defined by the optical characteristics. The most important ones in the case of the LEDs are light emission, absorption and interaction between light and changes in refractive index [98].

The most important optical features required for PMT calibration are the light intensity and the speed at which the optical pulses are switched. The relationship between the LED light intensity and its injection current is roughly linear. Nonlinearities in the relationship are usually found at very low and very high current levels [91]. This

is caused by the variation in LED radiative efficiency. This factor starts from being low at low injection currents and it increases with the current increase. It finally saturates at higher injection rates. Due to the low non-linearity and desired simplification, it is generally accepted that the intensity – current relationship is linear. This assumption allows a simple estimate of the LED output intensity if the current flowing through the device is known.

Theoretically, the radiation efficiency at any temperature is proportional to the number of electrons and holes present in the material as shown in Equation 2.44, where β is the constant of proportionality [92].

$$R = \beta np \tag{2.44}$$

In principle, LEDs are nearly 100% efficient internally. By the time the light leaves the outer surface of the device, this efficiency is significantly reduced because of the material properties. Similarly, the material properties limit the speed at which the devices react to the driving signal. The time response of the optical signal is subject to the physical characteristics of the device itself. It is not possible to realise instantaneous switching between the on and off states. The optical output is a result of the recombination process. The time the carriers take to travel across the depletion region together with the time carriers take to recombine, represents a delay between the stimulating current pulse and generation of the optical signal. A comparatively small additional delay is caused by the optical signal propagation to the outer surface of the device. When the electrical signal to the junction is removed the excess minority carriers contained within the junction take a finite time to recombine with the majority carriers. Thus they are responsible for the exponential turn off decay [90].

Generally, it is expected that the rise of the optical signal should closely follow in shape its electrical counterpart, but after a certain time delay. The removal of the electrical pulse does not necessarily imply an immediate disappearance of the optical signal. More detailed consideration of the LED transient responses is studied in Section 3.3.

2.3 Advanced Structures - High Brightness LEDs

In a pursuit of improved electrical and optical characteristics of the LEDs, different types of junctions have been developed. These are split into groups: homojunctions, heterojunctions and metal - semiconductor junctions. Different doping in the same semiconductor forms a homojunction, while a heterojunction is created using at least two different materials. A metal-semiconductor junction is produced using a metal and semiconductor.

Heterojunctions are a direct product of the need for improvement in light intensity. A heterojunction is normally formed between two lattice-matched semiconductors of dissimilar energy bandgaps. The junctions are named using lowercase for conductivity type of the smaller bandgap material in combination with the uppercase for the conductivity type of the larger bandgap material. Depending on which conductivity types of the materials are employed, these junctions can be either isotype (p-P, n-N) or anisotype (p-N, P-n). The two most common types of heterostructures are Single Heterojunction (SH) and Double Heterojunction (DH).

The same mathematical relations regarding the depletion layer, the carrier distribution, the current-voltage characteristics and capacitance are valid for both homojunctions and heterojunctions [91]. The additional resistance can be caused by contact resistance, resistance caused by the abrupt heterostructures and bulk resistance occurring particularly in the materials with low carrier concentrations or low carrier mobilities [96]. A voltage drop occurs at the series resistance thereby increasing the drive voltage [96].

2.3.1 Single Heterojunction

Single heterojunctions are used with the aim of controlling distribution of excess minority carriers through restriction of the diffusion length. Normally a P-p-n diode is formed with heavily doped n region. Consequently, electron injection completely dominates hole injection. The P-p heterojunction restricts electron diffusion and confines them to the narrow gap p region (Figure 2.7). This becomes the active region. Its thickness is controlled by the location of the P-p heterojunction with respect to that of the p-n junction [91].

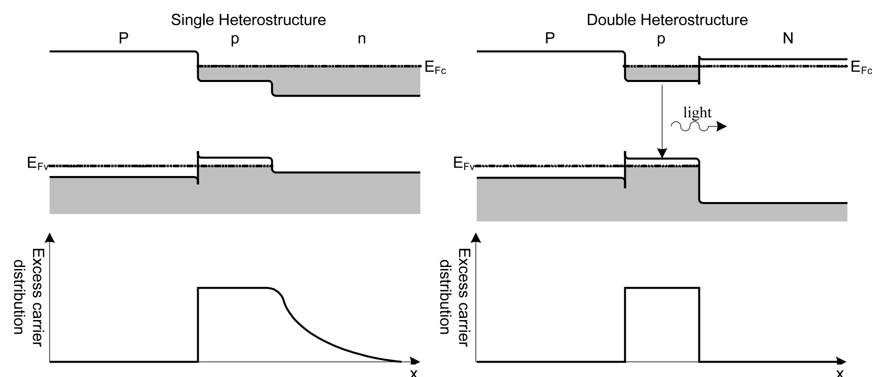

Figure 2.7: SH and DH energy bands and excess carrier distribution

2.3.2 Double Heterojunction

Improved electrical and optical confinement is possible when a DH is employed. These devices are either P-p-N or P-n-N. Most of the injected excess carriers are collected in the narrow gap where they are bounded by the energy barriers on both sides, as shown in Figure 2.7. Typically, this active layer is under $100nm$ wide. Compared to the active layer of a homostructure that has a thickness of the order of $1\mu m$ or larger, which is determined by the electron diffusion, this tight carrier confinement creates a much higher carrier concentration for a given injection current [91]. The achieved high carrier concentration results in high radiative efficiency of the recombination process. As the radiative recombination rate is given by the bimolecular recombination equation (Equation 2.44) it is clear that a high carrier concentration in the active region increases the radiative recombination rate and decreases the recombination lifetime [96]. Consequently, all high intensity LEDs employ heterojunctions.

The optical energy of the generated photons is lower than the energy bandgap of the barriers (Figure 2.8). Consequently, the barriers are transparent to the light emitted by the active layer. This reduction of absorption loss makes DH devices also optically superior over their SH and homojunction counterparts.

2.3.3 Single Quantum Well - InGaN Based LEDs

A quantum well (QW) device is a variation of DH. It is formed when the layer between two barriers is thin enough to cause quantisation of energy. This results in discrete energy levels associated with the motion of electrons and holes, as shown in Figure 2.8 [91].

The simplest possible structure employing this effect is a single quantum well (SQW). It consists of a thin layer of narrow gap semiconductive material sandwiched between thicker layers of a wider gap material. This layer formation causes an increase of carrier concentration in the quantum well region thus increasing the number of carrier interactions. The injected carriers are more concentrated in a quantised subband of a quantum well than in the entire band of a bulk semiconductor [91]. The emitted light intensity increase makes the SQW one of the basic building blocks for optoelectronic devices. This is the most common structure used for manufacture of high brightness LEDs. The simplified energy band diagram of the device is shown in Figure 2.8.

The operation of the quantum well largely depends on the length of the quantum well (l_{QW}) as it is required to be sufficiently small in order to create size quantisation. If the active layer is thin enough, the motion of carriers in the direction perpendicular to the heterointerfaces is quantised. That is, this motion involves discrete (quantum) energy levels [99, pp99-103].

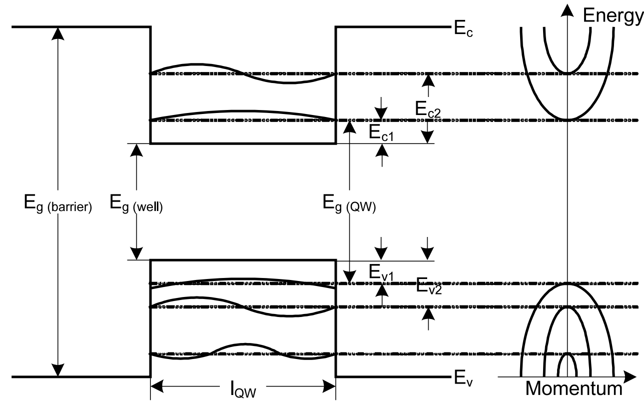

Figure 2.8: Single Quantum Well Energy Band Diagram

The energy of the transmitted photons and wavelength of the transmitted light also depend on the length of the quantum well. The quantised electrons and holes contribute to energy band gap of the newly formed material as the new energy band gap is equal to the sum of well material band gap and electron/hole quantised energies, as shown in Equation 2.45. The selection rules for optical transitions of electrons between quantised conduction sub-bands and quantised valence sub-bands require that only transitions between a conduction sub-band and a valence sub-band of the same quantum number are allowed [91]. It can be seen, from Equation 2.45 and from Figure 2.8, that the emission energy caused by the quantum well is not the same as the emission energy of either of the two materials employed. This limited independence of the emitted light energy and hence wavelength, makes the SQW devices an attractive solution for manufacture of light emitting devices operating at wide range of emission wavelengths, but using the same technology. This allows freedom to design required emission wavelengths.

$$E_{gQW} = E_{g(well)} + E_{c1} + E_{v1} = h\nu \tag{2.45}$$

Following the laws of quantum physics, it can be shown [92] that the precise expression for the energy band gap of the quantum well is defined by Equation 2.46, where m_r^* is reduced effective mass expressed in Equation 2.47 in terms of electron m_e^* and hole m_h^* effective masses.

$$E_{gQW} = E_{g(well)} + \frac{h^2}{8m_r^* l_{QW}^2} \tag{2.46}$$

$$m_r^* = \frac{m_e^* m_h^*}{m_e^* + m_h^*} \tag{2.47}$$

The structure of SQW devices also restricts the possibility of surface recombination because the carriers are enclosed inside of the well and are less likely to escape through

the surface and recombine - as shown in Figure 2.9.

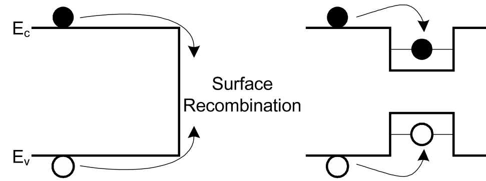

Figure 2.9: Prevention of surface recombination in SQW

It is possible to stack quantum wells together in order to create Multiple Quantum Wells (MQW). These are used in semiconductor lasers. The MQW maintain the same properties as SQW, but they also have larger volumes due to stacking. This material property causes higher optical power output of the MQW. When the vertical wall thickness of the MQWs is reduced so that the carrier tunnelling is possible, the final result is a Super Lattice (SL). The MQW and SL have relatively similar physical and optical properties.

2.3.4 Manufacture of High Brightness LEDs

Heterostructures became a norm in LED technology because of their contribution to device improved optical performance [51] as well as decrement of the LED (or LD) threshold voltage [53]. The layer structure of the IR sources for optical fibre communications always involves a double heterostructure for optimum efficiency [22, pp24].

Double heterostructure blue LED employ InGaN films grown using MOCVD technology (an alternative is InGaN/AlGaN). The compound is grown indirectly onto a sapphire substrate using GaN instead of AlN buffer layer. The dopants are introduced into the active layer during its deposition. The doping atoms are usually Zn or Si and are introduced into the manufacturing process with the gases containing these atoms (monosilane and diethilzinc). The dopants need to be introduced in order to create blue emission centres. It is also possible to conduct combined doping where both Si and Zn atoms are introduced into InGaN deposition simultaneously. These impurity atoms are responsible for the high efficiency performance through the use of impurity assisted recombination. Such deposited films are then exposed to thermal annealing in order to reduce resistivity of the p-type material and convert it from almost insulating into semiconductive material. This process ensures that the entire area of the as grown layer is uniformly converted into a highly p-type material. An alternative approach that creates similar results is LEEBI treatment, which produces thinner p-type layers of poorer quality. The growth process as well as the reasons for replacing LEEBI treatment with thermal annealing are described in Section 2.1 in more detail. Once all of the layers are deposited, the chip is partially etched until n-type layer is exposed. The chip is then framed and the contacts are added to it. When testing such device, it was

established that the device output light power is linearly proportional to the current flow. The light emitted by the device is relatively constant at temperatures between −20°C and +80°C [22, pp200]. An interesting feature performed by these devices is the movement of the peak wavelength - it shifts to the shorter wavelength side of spectrum with increasing forward current.

The manufacturing processes engaged in production of double heterostructure blue LEDs are only vaguely understood. This is one of the main reasons for the lack of comprehension of III-V compounds' physical characteristics. After all the operation of these devices is a mystery, given the huge number of defects in them [22, 96].

The blue SQW LEDs were commercialised in 1994 [100]. Following the theoretical requirements for narrow active region, a layer of undoped InGaN is used as an active region of SQW blue (as well as violet to yellow) LED. The reduced thickness and the use of undoped material for the active region are the main differences between the SQW and DH LEDs [22, ch10]. The emission wavelength of the devices is selected by the control of In mole concentration in this active layer. Even though the output power of the devices represents an improvement in comparison with devices made of other types of materials, a characteristic of the SQW LEDs that requires improvement is the FWHM of the luminous intensity at longer wavelengths. The FWHM of these devices tends to widen due to stress on the well caused by the difference in thermal expansion of the well and barrier materials. However, at the shorter wavelengths, this characteristic is dramatically improved when comparing with DH LEDs. The manufacturing of the device is performed in the same manner as manufacturing of the previously developed blue LEDs - TF-MOCVD [22, 54, 57, pp221]. Different layers are deposited on top of each other and the etching take place in order to expose the p-type material. Contacts are added to both terminals and the wafer is cut into square shapes. A typical layer structure of an InGaN based SQW LED is shown in Figure 2.10.

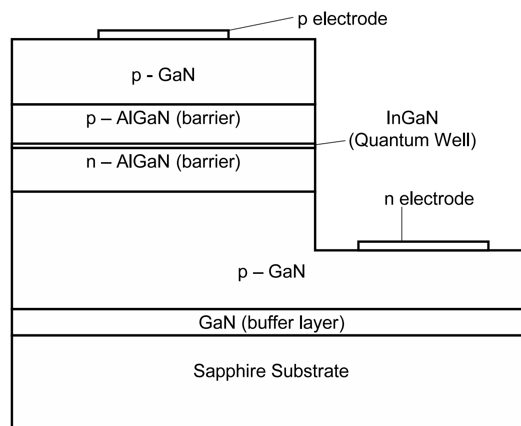

Figure 2.10: Typical InGaN based SQW LED material structure

The development of the SQW LEDs was a step towards realisation of MQW lasers.

Even though the aim was an LD, the LEDs have benefited from this tendency to improve the materials and techniques used for LD development.

2.4 Applications

LEDs are considered the ultimate general source of continuous light due to their high luminescence efficiency, quick response time and long lifetime [22]. Most commonly, the LEDs are used as indicators and displays. However they do have wide application range - some of its uses are shown in table 2.1.

Application	**Example**
Telecommunications	fibre optics light source
Electronics	erasing EPROM (UV)
Semiconductors manufacturing	definition of mask patterns for wafers
Environmental	UV air purifier, UV decomposition of toxic substances
Transport	traffic lights, street lighting, vehicle lights
Security	chemical detection, emergency lights, forgery detection
Medicine	test equipment, cancer treatment, human genome analysis
Home appliances	indicators and displays, TV sets, phones
Advertising	displays
Measurements	indicators
Office Equipment	printers, scanners

Table 2.1: Common LED applications

LED application can mainly be split into three general groups: displays, indicators and in more recent years lighting.

In the past, prior to the development of the LEDs, small incandescent lamps were used as the front panel indicators. First application of LEDs involved their use in scrolling red light messages on a black background. These were obviously used for displaying purposes. With the time, these simple apparatus evolved into three-colour displays as amber and green LEDs were finding their way into the market. LED use for digital displays (most commonly as 7-segment displays, but also in the form of 16-segment displays for alphanumeric outputs or as dot-matrix displays) allowed messages to became more complex too, as they developed into animations as well as the simple scrolling letters. A disadvantage that was hanging over the use of LEDs was that they were definitely indoor devices. With time, this changed as brighter and more robust devices were developed, so that these products could be used for outdoor purposes as well because of the increased brightness in relation to ambient sunlight.

One of the greatest disadvantages that followed LEDs for a long time through their development was the inability to produce true-colour. The reason for lack of such ability came from the fact that no blue light could be produced with the use of LEDs. This changed in the 1990s with the advancement in green and blue light emitting technology. The capability to produce green and blue colours permitted creation of full colour displays with the use of the three primary colours (red, green and blue).

By mid-1990s, LED technology was sufficiently developed to support practical application of full-colour animation displays. Alongside the invention of new devices that were outperforming their predecessor in the wavelength aspect of the LED characteristic, the LED brightness levels were significantly improved as well. This meant that mono-colour traffic signals and other similar applications that require the brightest LEDs possible are nowadays achievable. The high brightness blended with weather-resistant packaging makes the LEDs supreme devices for such applications as traffic signals, speed limit signs, stadium scoreboards or advertising for example.

The size and the lifetime are also the factors that contributed to the inclusion of LEDs in telecommunication systems. They do have disadvantages when used as such: poor intensity, lacking ray focus, low-modulation bandwidth, and incoherent radiation when contrasted against laser diodes. These disadvantages have forced LEDs to be applied into relatively low-bandwidth short-distance networks such as Local Area Networks (LANs). The communication means for such networks are fibre optics cables.

On the other hand space propagation based optical transmission systems, that do not require any cables or electrical waves, can be set up at relatively short range. The interference imposed by sunlight and light producing devices makes the range be a very important limiting factor in such systems. Hence, such sort of communication is advisable under special conditions - i.e. darkened environment. Alternatively, UV LEDs can be employed in order to slightly extend this range, as the influence of sunlight and fluorescent lamps becomes rapidly weakened at wavelengths shorter than $380nm$.

As previously stated some of the major advantages of LEDs are their energy efficiency and lifetime. When compared with conventional light bulbs, their power consumption is reduced by at least factor of ten. Concurrently, LEDs are likely to operate in normal conditions for up to ten times longer than the standard light bulbs do. These are the reasons for many to believe that LEDs are to become light sources for the future.

The other advantages that LEDs have over conventional light bulbs include being environmentally friendly (lifetime, material, size) and having a superior response speed. This technology is already introduced into a broad range of applications such as illumination, backlights and decorative lighting.

2.5 Chapter 2 Summary

The technological evolution of the LEDs prescribed the grounds for the physical characteristics of the devices. The structure of the current devices is largely determined by the historic search for the materials and manufacturing methods that would satisfy market trends at the time. The resulting limited functionality does not necessarily allow the use of these devices in fast pulsing applications. The appropriateness of the devices for the proposed application is investigated in the following chapters. The construction of LEDs is important for the background understanding of the electrical and optical properties of the devices in question. This chapter touched upon the manifestation of these electrical and optical characteristics. These informed about possible LED theoretical responses to the driving signals. The device current, capacitance and optical generation are of the main interest for the application. All these properties are defined by the behaviour of the charge carriers in the LEDs.

The structure of the advanced devices informed about possible complications caused by the still progressing and not fully understood technology. The LED applications showed the direction the LEDs have followed. Chapter 3 considers the response of these devices to pulses and the methods employed for creation of adequate LED driving signals.

Chapter 3

Pulse Shaping Techniques and LED Pulse Response

This chapter focuses on the methods of pulse generation and subsequent shaping. Existing techniques are studied. Some of the techniques used by the standard LED drivers are experimentally determined with no full theoretical appreciation of their operating principles publicised. The techniques are theoretically analysed in order to determine their suitability for the intended LED driver. The techniques are altered and optimised for the intended application. The optimisation is based on the developed theoretical understanding of the operating principles. The developed methodology is employed as described in Chapter 6. The aim of this research is to generate switching techniques that would overcome some of the problems caused by physical responses of LED to fast electronic "turn on" pulses. The main focus of this work is the creation of an optical signal that would satisfy the requirements for high speed PMT calibration and the simulation of optical signals encountered by Cherenkov radiation detectors. The work differs from the standard reported techniques in that it is completely focused on the theoretical understanding of the techniques and their applicability to the LEDs as opposed to the ad hoc methods.

Generally, the shape of the optical pulses generated by LEDs is governed by the driving signal parameters. However, at higher switching speeds the output optical pulses are dictated by the LED physical properties. This switching process takes finite amount of time, which is determined by the device quantum characteristics. The fast pulse response of the LED is considered in detail in Section 3.3.

3.1 Types of LED Drivers

The review of the pulse generating circuits [101–119] shows that in order to obtain fast optical pulses the LED drivers very commonly rely on the simple concept of dis-

charging capacitor through a fast switch (as described in Section 3.4). A few groups of circuits are identified as possible foundation for the LED drivers. These are described in the following sections. A number of potential LED drivers are considered in this chapter. These are: multivibrators, emitter-coupled monostable, avalanche transistor based drivers and a complementary transistor pair regenerative switch.

3.1.1 Multivibrators

Multivibrators [103–107, 120] are circuits commonly used for creation of (rectangular) pulses. They rely on the use of regenerative transistor switches. They are split into three groups: bistable, monostable and astable. There is also a special case of multivibrators, which are used as Schmitt Triggers.

It is the regenerative action of the monostable and possibly astable multivibrators that could play an important role in creation of fast optical pulses. The quasi-stable states of those vibrators are determined by the passive components in the circuit. These states inevitably stop with no aid from an external signal. Hence if triggered (in monostable case) and if the time from the beginning to the end of the quasi-state can be reduced to the required period then the circuit could be used as a basis for an LED driver. One of the primary uses of monostable multivibrators is creation of pulses well defined in amplitude and duration when incoming pulse is weak or ill defined [103].

The simplicity of multivibrator circuits is seen as an advantage that could potentially be exploited for generation of the required optical pulses. However, the experimental work has resulted in relatively poor pulse timing when compared with the other techniques that are considered in this chapter. It is concluded that the discharging time constants in the circuits are much higher than what would be tolerable to generate adequate optical pulses.

3.1.2 Emitter Coupled Monostable

The emitter coupled monostable [103, 108–110, 120] is a variation of multivibrators derived because of its speed, improved linearity and stability. The width of the output pulses is linearly dependant on the trigger voltage. Simultaneously, this width is also controlled by the passive components in the same manner as for the other multivibrators. This pulse width dependence on the passive components provides an advantage for the multivibrators, as their output can easily be repeatable due to the passive component value accuracy.

An advantage that the emitter-coupled monostable could provide over the other pulse drivers lies in the fact that its output can easily be pulled below the ground level. This would provide the load LED a chance for its current to be swept out of the depletion layer (see Section 3.3).

The emitter coupled configuration was in the past a basis for conventional digital circuits. The Emitter-Coupled Logic (ECL) circuits were at one point the fastest conventionally available digital circuits [110].

The experimental work performed on the emitter coupled monostable circuits has generated improved pulse timing in relation to that of the standard multivibrators. This is mainly attributable to the ability of those circuits to pull the signal below ground level before the switched signal approaches its slowest section. This establishes reverse bias across the LED so that the optical pulse is cut off early. However, the experimentally achieved pulses are deemed to be slower than required, hence the technique was abandoned.

3.1.3 Avalanche Transistors

When the reverse bias across a p-n junction is increased to the junction breakdown level, the diode conducts very large current. Even though this process is not necessarily destructive, the maximum current must be limited in order to avoid excessive junction heating. This is why the avalanche breakdown represents the upper limit of the p-n junction reverse bias [90].

Reverse bias provides increase of the depletion layer electric field. This electric field causes sweep of the minority carriers across the junction (and hence saturation current). If an electron (p-type minority carrier) is attracted by the electric field, it accelerates across the depletion layer. It is likely that this electron collides with a crystal (or impurity) atom in the depletion region delivering its kinetic energy to the atom with which it collides. However, if the electric field is increased so much so that the electron gains enough energy to break covalent bonds, than it causes creation of the electron-hole pair [121]. The newly formed pair gains more energy from the electric field causing creation of more electron-hole pairs. The process continues in the avalanche manner for as long as the avalanche conditions are maintained.

It is reported that the LED avalanche breakdown as well as the use of avalanche transistors for LED driving makes it possible to obtain sub-nanosecond light pulses [13, 109, 116–119]. However, it was found that the number of emitted photons in such case is limited to several hundreds, thus limiting the possibility for application of the driver. A few avalanche transistors can be used in series in order to gain enough current to drive the load LED with required pulse height [116].

The failure of the avalanche transistor circuits to provide repeatable and reliable pulses is the main reason for rejection of this technique as a possible candidate for development of the LED driver in this case.

3.1.4 Complementary Transistor Pair Regenerative Switch

A successful light pulse generator based on PNP-NPN regenerative switch (Section 3.4) is reported by Kapustinsky *et al.* [14]. It provides sufficient current to drive directly a blue LED. It is primarily intended for use in calibration of scintillation detectors. The LED driver circuit is shown in Figure 3.1. The trigger signal sent to the electronic switch is a negative $1.5V$ to $3V$ pulse superimposed on the $24V$ negative d.c. supply. The supply and the d.c. component of the trigger pulse charge the storage capacitor C_3. The minimum trigger pulse width of $150ns$ is required for the capacitor to have a sufficient length of time to charge fully. The falling edge of the trigger pulse is differentiated with the resistor - capacitor (R_3C_2) combination. This differentiated edge triggers the complementary pair regenerative switch consisting of the two transistors. This action in turn creates low impedance path for the capacitor C_3 to discharge its stored charge through the two transistors and hence through the LED. This rapid charge release provides a fast current pulse to the LED. However for the reasons discussed in the Section 3.3, the optical pulse does not follow the electric signal closely. The width of the decaying optical signal is reduced by an inductor L_2 connected in parallel with the LED. The voltage induced by this inductor opposes the charge released by the storage capacitor C_3, hence reverse biasing the LED and helping its trapped charge carriers to be swept away from the depletion layer. The inductor introduced to the LED is reported to reduce the fall time of the decaying light pulse from $100ns$ to $12.5ns$ [14]. This circuit is taken as a basis for the later developed circuitry (Chapter 6) because of its promising timing characteristics and ability do provide relatively high amount of current at high speeds.

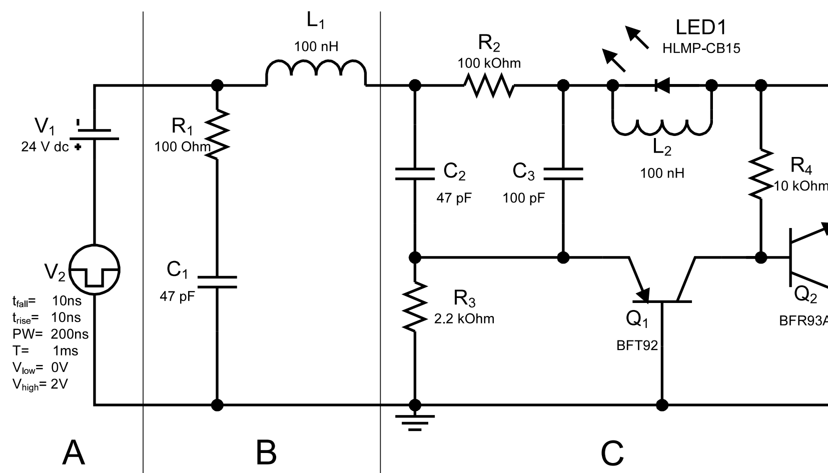

Figure 3.1: A - oscillator input signal riding on negative DC supply, B - power supply filtering, C- Original Kapustinsky oscillator

3.1.5 Standard Telecommunication Techniques

A number of LED driving techniques are used in optical fibre based telecommunication systems. The widespread interest in this field has resulted in commercially available simple IR LD drivers. These often operate at high frequencies because of the communication demand for high-speed data transmission. As these devices are designed to drive LDs, they are normally capable of providing currents that are large enough to drive the blue LEDs in pulsing mode. However, a problematic aspect of these drivers is their low output voltage. As the energy band gap of the light emitting devices is inversely proportional to the emission wavelength, the voltage required to drive these in the shorter (blue) end of the spectrum is considerably larger than that needed to modulate IR LD.

It is possible to obtain ready-made white LED drivers with output voltage high enough to drive blue LEDs. However, these are normally designed for low frequency operation as they are normally used for backlight of displays and keyboards. Currently, there is no driver of this type that would satisfy the required current, voltage and frequency conditions simultaneously. The same is true for operational amplifiers, which can be used as LED modulators in telecommunication systems.

A combination of the above drivers and the frequency doubling materials can be exploited to half the emission wavelength of the communication LD. Unfortunately, the normally used optical communication windows ($850nm$, $1310nm$, $1550nm$, $1650nm$), largely limited by the fibre attenuation characteristics, do not fall in the required wavelength band that would when halved produce required Cherenkov radiation matching emission wavelength.

The above techniques could potentially be exploited for the proposed application, but at the moment they do not provide required functionality.

3.2 Overview of Standard Pulse Shaping Techniques

The investigated pulse shaping techniques are described. These are implemented to a various degree at different stages of the driver development.

3.2.1 Differentiation

Various techniques can be exploited for pulse modification in order to obtain a pulse with desired characteristics. The simplest principle for pulse shaping is differentiation. This reliable method can be implemented with the use of passive components. It is well established that a pulse contains a wide spectrum of frequencies. This process

eliminates the lowest frequency components of the input pulse and allows the higher frequencies to pass through. A disadvantage of such signal modification is a power reduction through redistribution of frequency components. The technique is also limited as the pulse leading edge depends on the transistor switching characteristics and is not improved by differentiation.

Short lengths of open circuit or shorted transmission line can also be used as differentiation circuits. These lines, because of their high 'Q' factor, are often used when high voltage pulses are needed. The transmission line was a preferred modulation solution in the early RADAR designs that required short high voltage pulses.

3.2.2 Step Recovery Diode

The circuit shown in Figure 3.2a can be employed for the improvement of the pulse leading edge. The pulse source (V_S) represents a pulse generating circuit used for creation of the input signal. The blocking capacitors are used to isolate the step recovery diode from the input and output stages. The fast switching diode is normally forward biased under the influence of the voltage supply V_b. Some charge is stored by the diode while it is forward biased. A slow rising positive going pulse reverse biases the diode and diverts the diode's transient current into the load. The diode acts as a short circuit bypassing the pulsing circuit until the diode's stored charge is depleted. Upon charge depletion, the diode starts acting as an open circuit and it allows the input pulse to be applied to the load. Figure 3.2b shows the simulated input voltage (at point X), diode current (from ground to point Z) and output voltage (at point Y) waveforms. The rise time of the output voltage is purely dependant on the transition time of the diode and the charging time of its internal capacitance in combination with any stray shunt capacitances [101]. Obviously, the benefit to the rising edge of the output pulse in comparison with its input counterpart is only viable if the switching time of the diode is shorter than that of the input pulse's rising edge. The step recovery diodes can be used in more complex circuits for better control and improvement of rise and fall times [122].

3.2.3 Clipping and High Speed Comparators

It is proposed and experimentally confirmed that a possible method for altering the pulsing signals in order to create faster rise and fall times includes the use of clipping circuits. This could be employed if the input pulse has a very slow rising edge at its infant stage or indeed to clip the end part of the falling edge that asymptotically approaches its minimum level. An issue arising from the clipping action is the reduction of power transfer. Also, the timing improvements are possible only if the switching frequency of the clipping diode is considerably faster than that of the driving pulse.

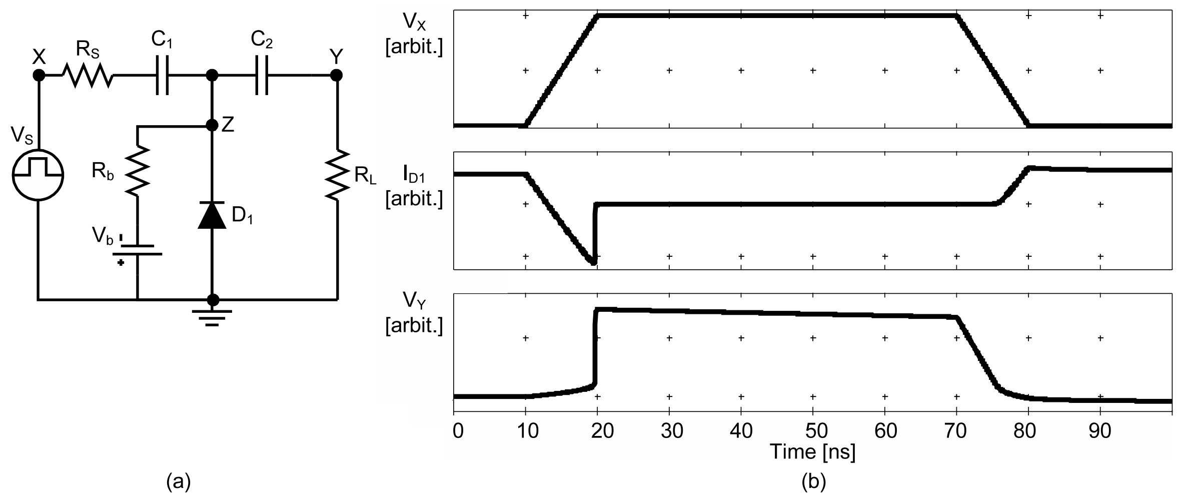

Figure 3.2: Pulse sharpener: (a) circuit, (b) input pulse, diode current and output pulse

It is possible to avoid the clipping circuit energy loss by employing the comparator circuits. The comparators generate output pulses when a set voltage value is detected. The energy of the resulting pulse is independent of the input pulse. The negative aspect related to the comparator design is its speed. The transition times of the comparators need to be shorter than that of the incoming pulse if the circuitry is to result in improved timing.

3.2.4 Non-Saturating Switch

Similarly to the switching action of the diodes, the transistor transition times are not instantaneous. This is due to the internal characteristics of the components i.e. practical active devices are not purely resistive. The capacitances associated with the transistors cause two types of delays for the transistors during switch off. These delays are storage and fall time (as shown in Figure 3.3a). The storage time is the interval in which the transistor output drops to 90% of its maximum output level after removal of the driving base current [113]. The delay is caused by trapping (storing) of the charge carriers in the collector-base depletion region when the junction becomes reverse biased [114]. These carriers are the ones that normally flow across the junction when it is forward biased. Once stored, the length of time required to remove the trapped carriers depends on whether the transistor is saturated or not. In the case when it is saturated, then the hardness of the saturation defines the removal of the trapped carriers from the depletion region.

From the above, it follows that the storage delay can be avoided by not allowing the transistor to reach saturation. This is achievable with the adequate biasing. An alternative method, that provides more reliable performance, involves the use of a fast switching signal diode connected between the base and the collector of the transistor

as shown in Figure 3.3b. The voltage drop across the diode ensures that the transistor never enters the saturation stage. The usefulness of the circuit depends on the choice of the diode. The diode reverse recovery time should be considerably shorter than the transistor recovery time. Also the diode voltage drop rating should be smaller than the voltage required for sending the transistor collector-base junction into saturation [104, 120].

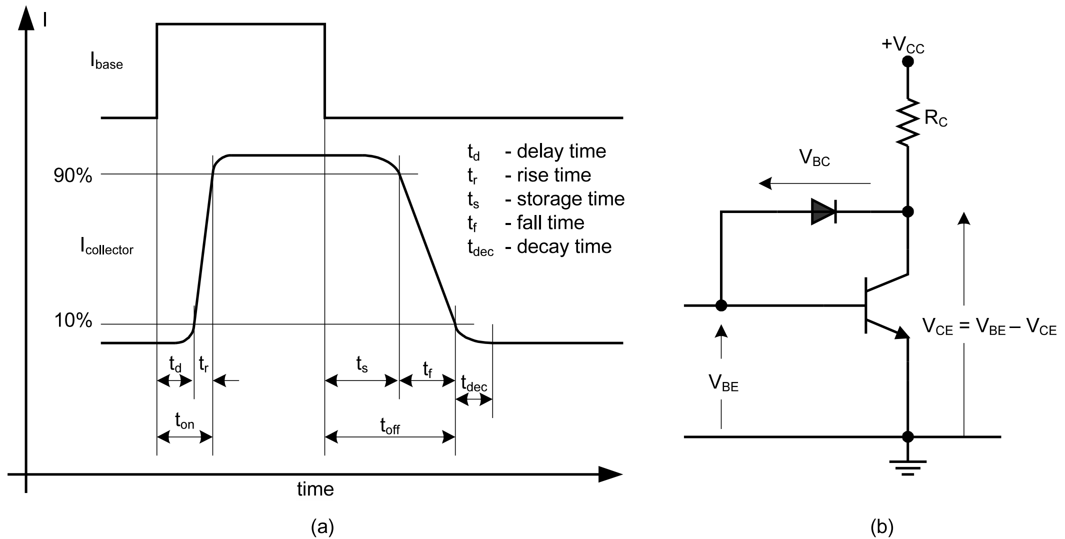

Figure 3.3: Non-saturating transistor: (a)transistor timing, (b) non-saturating configuration

3.2.5 Speed up Commutating Capacitor for Transistor Switching

Transistor switching speed is reduced if the charge stored by its junction capacitance is removed prior to transistor being switched on [105]. If the junction transistor capacitance is charged in the reverse direction, then this capacitance needs to be discharged before the base-emitter voltage can become positive. The transistor capacitances can be charged faster if the transistor base current is made larger than is necessary to be to turn the transistor on [104].

A method used to satisfy both of the above requirements employs parallel capacitor-resistor combination in the transistor base current path as shown in Figure 3.4 [101, 104, 105, 108, 109, 113]. A disadvantage arising from this technique is that the transistor overdriving causes increase of its storage time (see Non-saturating Switch - Section 3.2.4). However, the capacitor-resistor combination only overdrives the transistor during the rising edge transient. This method also allows for the reduction of the storage time and fall times as it provides reverse bias conditions to the base-emitter junction during the turn-off [104, 109].

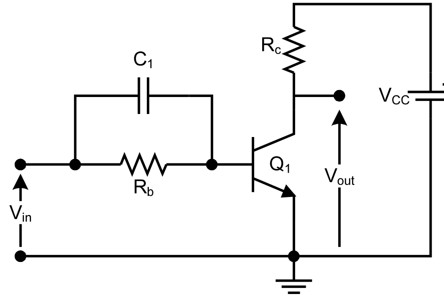

Figure 3.4: Speed up capacitor configuration

3.2.6 Shorted Turn - Theory and Application

Faraday's Law defines the behaviour of an induced voltage in a coil under the influence of a time-dependent magnetic flux. The induced EMF (ξ) in a circuit is proportional to the rate of change of magnetic flux ($d\phi$) in that circuit. If the circuit is represented by a coil of N turns then the induced EMF is given by Equation 3.1.

$$\xi = -N\frac{d\phi}{dt} \tag{3.1}$$

Lenszs' Law dictates that the induced flux generates a voltage (back EMF) that tries to oppose any change in the circuit. The inductive properties of the magnetic circuit, defined in Equation 3.2, influence the way in which a time-dependent current flows and subsequently the magnetic flux it produces. In the case of a simple transformer wound on a ferromagnetic core, the inductance (L) of the circuit increases with the increase of the relative permeability (μ_r) of the material used. The induced output voltage and the nature of its shape can be controlled by manipulating the way a time-dependent current establishes a magnetic flux and the way this flux is made to collapse. Hence the frequency spectrum of the output pulse is also controllable.

$$L = \frac{\mu_r N^2 \mu_0 A_c}{l_c} = \mu_r L_0 \tag{3.2}$$

$$L = N(\frac{d\phi}{di}) \tag{3.3}$$

The coil inductance is also the measure of the change in linking flux as a result of change of current flow in the coil (Equation 3.3). Equation 3.3 implies that the large current change with no substantial flux change results in small coil inductance. This emphasises the importance of the operating point on the hysteresis curve (Figure 3.5). Operation on the steep slope of the curve results with a substantial coil inductance. However, if the operating point is in the saturating region or near it, then a large change in current will cause a very small change in flux and thus the coil inductance will be significantly lower than in the previous case. Simultaneously, the induced voltage is

significantly lowered as a result of the decreased coil inductance caused by the lack of flux change. This happens as the induced voltage is proportional to the coil inductance (Equation 3.4).

$$\xi = L(\frac{di}{dt}) \tag{3.4}$$

The theoretical considerations from this section imply that there are two potential applications for the high frequency transformer:

1. Saturation of the core of the pulse transformer (stimulating change in current while limiting change of magnetic flux)

2. The use of the shorted turn around the core (application of Lensz's law)

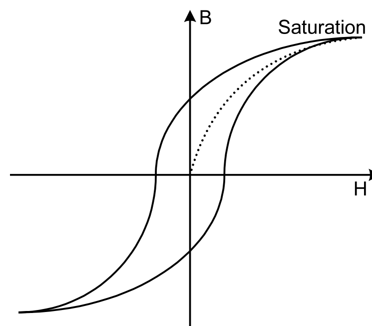

Figure 3.5: Hysteresis Loop

Core Saturation

Inspection of the hysteresis (B-H) curve of a material (Figure 3.5) shows that if the operating point of a coil is near the saturating region of its core, then the change in current does not produce large rate of change in the flux. Consequently, as implied by combination of Equations 3.3 and 3.4 there is little induced voltage in the coil even though the current flowing through the core changes in magnitude. This normally undesired region of operation has a potential to be effectively used for this application. If the coil is saturated during the rising edge of a pulse then the core of the pulse transformer by itself could be used for the pulse shaping. Providing that the coil inductance is sufficiently large, the transformer should allow the input pulse rising edge to be recreated on the secondary side. However, if during this rise time of the input pulse the core of the pulse transformer gets saturated, there will be no more change in the magnetic flux and hence no voltage will be induced on the secondary side after the saturation point is hit. This should make the secondary pulse collapse and its decay time should remain much shorter than the decay time of the input pulse. The output signal from the pulse transformer can then be used to drive an LED. This

technique could potentially reduce the pulse fall time, but does not improve the rise time. The issue of the rise time would have to be dealt with the use of faster switching components.

The core required for this application should allow easy saturation as the input pulses to the transformer in high frequency small signal applications have relatively small power. Effectively, the amount of current needed to saturate the core should be relatively low if the above principle is to generate the expected outcome.

The described system is modelled as shown in Figure 3.6. Transfer functions, which are the mathematical representations of the relationship between the output and input of a system, can be used to model this dynamic system. The second order transfer function applied to the unit step generates the input signal by differentiating (numerator) the input step function and consequently generating the band limited (denominator) impulse. The *tansig* (hyperbolic tangent sigmoid transfer function) in combination with the first order transfer function represent the system. Here, the differentiation of the input impulse represents the induction of the voltage in the system. The theoretical input and its output response are shown in Figure 3.7. The output is reduced in magnitude, has narrower pulse width and faster turn off than the input pulse. The negative portion of the output signal is preferred for driving LEDs in this application for the reasons described in Section 3.3.

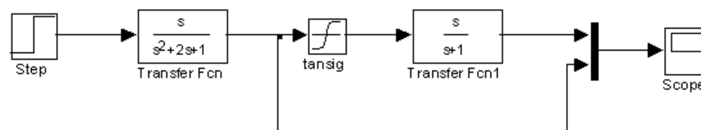

Figure 3.6: Core saturation - model

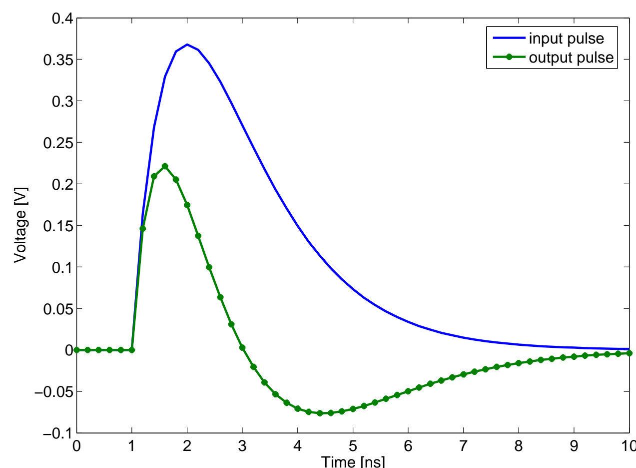

Figure 3.7: Core saturation model - simulation results

Shorted Turn

The shorted turn is commonly used in transformer design for the purpose of active shielding, especially in very sensitive applications like medical or audio instruments. The shorted turn is a band of copper that wraps around the core of a transformer. When used, it acts as an additional secondary winding with very low impedance, capable of drawing large amount of current. When in operation, as any other secondary winding, the shorted turn will induce voltage and the current flowing through it will oppose the flux generated in the coil (Lenz's law), therefore nulling the original magnetic flux. The shorted turn increases the rate at which the power dissipates in the circuit, thus lowering the 'Q' factor by decreasing the effective inductance [123]. This technique is regularly implemented for speed control of the magnetic head in data storage equipment [124]. It is proposed that the same method is explored in the planned pulse shaping for LED driving.

The above prediction is tested experimentally. The circuit shown in Figure 3.8 is constructed. The transformer is assembled by winding two coils around a toroid. A shorted turn is also added to the toroid. This is just a single piece of wire wound around the core with its ends shorted together.

The circuit (considered in Chapter 6) used to create the pulse is irrelevant as this is employed only to prove the principle of operation and investigate the possibility of applying the concept in later stage of the LED driver design. The measurements have proved that the technique that involves the use of shorted turn can be used to reduce the time of the falling edge of the pulse. It also reduces the ringing period of the transformer by approximately factor of ten. The experimental results show that the effective input impedance of the pulse transformer used later in Chapter 6 is reduced by up to a factor of hundred using this technique.

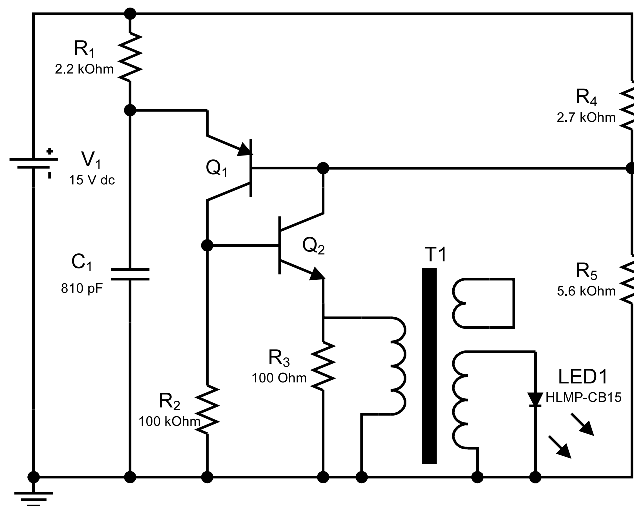

Figure 3.8: Shorted Turn test circuit setup

3.3 LED Switching Parameters

Due to the finite diffusion time in the semiconductor material the initiation of the minority carrier injection does not instantly result in a substantial minority carrier gradient between two sides of the PN junction. This lack of a large differential carrier concentration limits the flow of diffusion current across the device even though the diode is in the process of being forward biased. Consequently, the LED initially presents high resistance to the current flow. As the excess minority carriers drift further from the junction, the diffusion current increases and the diode resistance falls. The pseudo-transient resistance is dominant when the device is being turned on (as indicated in the following paragraph).

The LED releases photons upon initiation of the recombination process. The delay between an applied electrical pulse and the photonic output is caused by removal of the capacitance charges, the carrier diffusion and carrier recombination time. Additionally, the speed at which the LED responds to its driving pulse depends on the driving current pulse rise time and magnitude [120, 125]. If the LED is not appreciably reverse biased prior to the application of a driving pulse then the effect of the diode junction capacitance becomes less dominant. This is because the time taken to charge this capacitance becomes negligible [120]. The LED behaves only as a high value resistor during the short turn on period while the capacitive effect is eliminated. During this period the photon producing process is established and the device emits light. Thereafter the optical output is expected to follow the driving current pulse.

When the electrical signal to the junction is removed the excess minority carriers near the junction take a finite time to recombine with the majority carriers. This leads to a natural decay of the optical signal, which is governed by the minority carrier lifetime. Hence, the excess minority carriers, which are near the junction just before the removal of the driving signal, are responsible for the exponential turn off decay of the optical output [90]. The LED continues to generate light through recombination process until the excess minority carriers are removed. The characteristic time constant of this decay (see Section 2.2.2), denoted minority carrier lifetime τ_c, defines LED frequency response [92] as shown in Equation 3.5 where $R(f)$ is response at a given frequency.

$$R(f) = \frac{R(0)}{\sqrt{1 + 4\pi^2 f^2 \tau_c^2}} \tag{3.5}$$

Equation 3.5 is valid providing that the low-level injection conditions are satisfied. For high level injection the concept of constant lifetime no longer applies and some average value of τ_c must be assumed [92].

An alternative method of analysing the pulse performance of the LED would involve consideration of device's electrical characteristics. When an ideal electrical pulse

is applied to a purely resistive load, the voltage developed across the load is expected to closely mimic the input signal with respect to time. However, if reactive components are introduced into the circuit, the response of the complex load modifies the characteristics of the pulse shape. This latter point must be considered when fast changing electrical signals are used to drive LEDs. When dealing with a device in practice it is necessary to consider the effects of both the depletion and diffusion capacitances along with any parasitic impedance attributable to the circuit layout. When the diode starts to conduct the depletion capacitance disappears due to the removal of the parallel plate effect. Simultaneously, the carriers injected into the forward biased junction form the diffusion capacitance. The dynamic electrical impedance presented by the diode during switching is that of complex voltage dependant impedance, initially dominated by the depletion capacitive reactance combined with a high valued resistor. At forward bias voltages the impedance is controlled by the normal diode equation (Equation 2.29) in combination with LED capacitance. Hence, the parameter that limits the modulation frequency of an LED is the diffusion capacitance. As this capacitance is dominant over the junction capacitance in forward bias mode the junction capacitance can be neglected. Consequently the LED frequency response is dictated by the diffusion capacitance. Because this capacitance is the function of minority carrier lifetime (Equation 2.43 with reference to Equations 2.17 and 2.18) it is concluded that the minority carrier lifetime is the defining parameter for LED frequency response.

It follows from Equation 3.5 that the frequency response of the LED can be increased by reduction of minority carrier lifetime. This can be achieved by introduction of recombination-generation centres that have energy levels located near the mid-gap of material forming the p-n junction, such as gold in silicon [96]. Alternative solutions are use of highly doped active regions [126] or application of heterostructures. Minority carrier lifetime is reduced in heterostructures by formation of high carrier concentrations within small well regions [96]. Reduction of minority carrier lifetime inevitably results in decline of LED quantum efficiency. Therefore, this is not a feasible solution for those applications that require maximum possible optical output. The control of the minority carrier lifetime is dictated by the manufacturing processes and cannot be subsequently altered.

In practice, the junction capacitance needs to be taken into account when an electrical pulse is applied to a diode. The junction capacitance affects diode response if not eliminated or reduced prior to application of the driving pulse. The way to minimise the effect of this capacitance on diode pulse response is by ensuring the diode is not reverse biased prior to a pulse being applied to the device.

It is generally considered a good practice to reverse bias the diode immediately after the positive cycle of the drive pulse is removed in order to sweep out the remaining excess minority carriers. A bipolar drive pulse is used to achieve this condition. Using

Figure 2.3 as a reference, the effect of the reverse biasing process can be visualised. As the depletion width increases when the LED is reverse biased the large number of exponentially distributed minority carriers near the junction are removed. The time taken to sweep out the carriers can be assumed to be shorter than the minority carrier lifetime providing that a fast and adequate reverse biasing signal is applied to the LED upon removal of the drive pulse. Care must be taken not to exceed the reverse bias rating of the device.

3.4 Basic Switching Principles

The simplest way to generate a pulse is based on capacitor discharge into a load [102] with the aid of a high speed electronic switch. This is also a relatively inexpensive method, providing that adequate high speed switching devices are available. A possible candidate for successful application is a complementary transistor pair regenerative switch. It is formed by a pair of PNP-NPN transistors which are cross-coupled in such a way that normally both transistors are configured to be in the off state [103, 108, 109, 111, 112]. The transistors exit the off state when externally triggered or when the circuit is specifically designed to be free running. The transistor combination provides quiescent current equal to almost zero while its on state provides high current capability. The switch configuration shown in Figure 3.9 assumes that the storage capacitor C_1 is initially discharged and that V_{ref} is defined by the divider comprising of resistors R_2 and R_3 in conjunction with the power supply. As C_1 charges through R_1 the voltage across the capacitor eventually exceeds V_{BE1} necessary for the transistor turns on. The collector current of Q_1 switches on transistor Q_2. The collector current of Q_2 causes the V_{ref} point to fall rapidly enhancing the turn on of Q_1. This regenerative action continues until the current path through Q_1 and Q_2 discharges C_1. The discharge of C_1 automatically restets the circuit to the initial off state and the cycle starts again. This process results in a very fast rising pulse appearing across R_4.

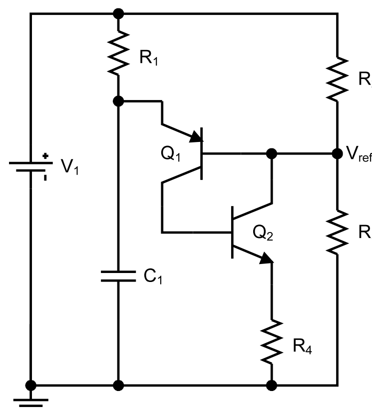

Figure 3.9: Complementary Pair Regenerative Switch

The simplicity and the fast action of the regenerative switch make it an ideal candidate for driving LEDs. The transient nature of the pulse makes it suitable for further pulse shaping. The above switching circuitry is combined with the pulse shaping techniques of Section 3.2 in order to develop adequate LED drivers (Chapter 6).

3.5 Chapter 3 Summary

The LED transient behaviour and the pulsing circuits suitable for driving the LEDs were covered in this chapter. When pulsed, an LED should act as a resistor at the instant when the current starts flowing through. This is why the LED electrical pulse follows the driving signal - with a sharp rising edge assuming that such is provided by a driver. If the pulse is maintained, the diode capacitance charges to its final value. Once this charge is built up, the removal of the driving pulse does not cause instantaneous disappearance of the diode current. The decay of the diode current after the withdrawal of the driving signal depends on the diode internal RC constant. Hence, this decay is exponential, as would be expected from a RC network. The decay can be reduced if the LED is driven into reverse bias upon removal of the positive pulse. The experimental considerations of the LED properties from Chapter 2 and from this chapter are considered in Chapter 5.

The prospective LED pulsing techniques and drivers are also reviewed. The complementary resistor pair regenerative switch oscillator is considered as a most feasible option for the further development. This decision is prompted by the simplicity and timing capability of the circuit and is also based on the experimental examination of the techniques described in this chapter. The other reviewed pulse shaping techniques are also considered as the possible contributors to an amalgamated design that would achieve the set objectives. It was experimentally determined that the shorted turn technique was likely to provide largest advantage in terms of pulse shaping in this case. The circuit development is described in Chapter 6.

The following chapter (Chapter 4) provides the theoretical basis for the modelling of the LED characteristics from this chapter and Chapter 2.

Chapter 4

LED Modelling

The device modelling is a standard part of the design procedure. The intention in this case is to use the models as a tool that provides the information necessary to determine the characteristics of the electrical signal required for generation of the desired optical output. The modelling is considered from a theoretical perspective in this chapter.

The data obtained from experimental characterisation of the devices' performance is used for behavioural description of the devices. The observed characteristics do not necessarily fully describe the devices. Some device characteristics frequently cannot be observed directly. Modelling is an analogy formed in order to represent the complete device behaviour. This analogy allows simulation of device or system behaviour. Consequently, it is possible to predict the system response to a known input. An effective model should match the performance of the practical configuration it is intended to represent.

The device models are divided into two groups based on the way they are derived. The equivalent circuit models are based on the theoretical consideration of device characteristics. The other group of models are derived empirically from the observation of the experimental results and the fitting of those results with the model. These are 'black box' type models. The external behaviour is seen as a most important feature of such models. Consecutively the internal physical properties of the devices are often ignored.

The equivalent circuit models are further divided into d.c. and a.c. models depending on the frequency of operation. The *d.c.* models are used for the low frequencies (usually up to $10kHz$). The rest of the frequency spectrum is covered by the a.c. models. These account for parameters such as parasitic capacitances and inductances.

The dependency of the devices on input signal level is represented by the use of small and large signal models. The small signal models are utilised for the use in the circumstances where the change in circuit voltages and currents should only cause small alterations from the d.c.-bias operating point. These models are linearised portions of the complete device so that the incremental current is proportional to the incremental

voltage for the small change around the point of operation. The large signal models are designed to operate under conditions where input signals cause large variations in the device operating conditions. The non-linear behaviour of the active devices makes it particularly difficult to devise an accurate large signal model. Hence these are usually derived from the analytical expressions or from the empirical relationships fitted to the experimental data [127].

The types of the device models are shown in Figure 4.1.

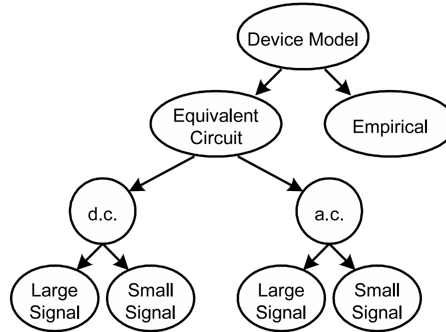

Figure 4.1: Types of models

4.1 OrCAD Models

The standard OrCAD (PSPICE) diode models are based on the theoretical considerations of the diode characteristics. The specific models are defined by the user-selected parameters. These parameters are derived theoretically. Such approach results in theoretical definition of the model that might not accurately resemble the performance of the practical device. Hence, in this case, the experimentally derived diode characteristics are used for definition of the model parameters. The resulting model should be a closer depiction of the real, rather than the theoretical, device.

PSPICE diode parameters (see appendix B), which define the diode models, are the standard component of the OrCAD package. The parameter selection used for definition of a model simultaneously defines the type of model used. The fewer the parameters used, the less accurate the model is when compared to its equivalent real device. However, inclusion of the particular parameters is not necessary in every application. The type of the application defines the complexity of the model. There is no need for the use of a large signal a.c. model if the diode is only to operate under the small signal *d.c.* conditions.

4.1.1 Ideal Diode Static Model

The ideal diode model is based around the ability to accurately represent the ideal diode current (Equation 2.29). The PSPICE performs this independently for two bias

conditions. Hence, the PSPICE form of the equation is of the form shown in table 4.1.

PSPICE equivalent equation	**condition**	
$I = I_s(e^{\frac{qV}{kT}} - 1) + V * GMIN$	for $V \geq -5\frac{kT}{q}$	Fwd bias & Rev bias for $V \geq Vthermal$
$I = -I_s + V * GMIN$	for $V < -5\frac{kT}{q}$	Reverse bias for $V < Vthermal$

Table 4.1: Ideal diode static model current

It should be noted that GMIN in table 4.1 is added by default in parallel with every p-n junction. Its default value is 10-12S and it cannot be set to zero. It is not important in terms of the diode characteristic description as it is a program (not device) parameter and is added to enhance computational efficiency. It also does not show any observable influence on the diode characteristic [121, pp160].

The saturation current (Is) is of opposite polarity from that of I. However, the measured value of the saturation current is considered by PSPICE as $-Is$, hence the negation symbol in the relationship between the diode current and saturation current is dropped out.

The d.c. forward characteristic in the PSPICE equation is determined by the saturation current only. However, Is is a constant in SPICE and as such does not properly model the voltage dependence of the depletion region current, which is due to the varying width of the depletion region. The complexity of the model increases for closer depiction of the real device.

4.1.2 Real Diode Static Model

Even though the experimental results for most junction diodes show a range of characteristics which are in agreement with the ideal diode equation, some discrepancies are present due to [93]:

- Carrier generation-recombination in the depletion layer
- High level injection
- Voltage drop associated with the electric field in the neutral regions
- Internal breakdown associated with high reverse voltage

The combination of these mechanisms results in more realistic diode models. Depending on which of the above mechanisms is considered during the modelling process, three different model types of the real diode are generated.

Real Diode: Small Bias - Effect of the Carrier Recombination-Generation

Idealised diode models assume constant electron and hole currents through depletion region [93]. The effect of this assumption is that the actions of the generation-recombination centres in the depletion region are ignored. Under forward bias conditions these centres contribute to the recombination process. Also when the depletion region is reverse biased, these centres act as source of free carriers. The effect of these two actions on the diode overall current is usually minimal. However, the activity of these centres needs to be considered when creating a precise model.

If the total current of a real diode (taking account of generation − recombination process) is given by Equation 4.1, where $I_{D(ideal)}$ is the ideal diode current and $I_{(r,g)}$ is the current caused by the generation-recombination process, then the current under reverse bias of the diode is generated predominantly in the depletion region. The current in the forward biased diode is dominated by the ideal diode diffusion current, especially as bias increases. In general, an expression that well describes the effects due to the generation-recombination processes is given by the empirical relation shown in Equation 4.2 where η, the emission coefficient, is usually about 2 if the recombination current dominates and is equal to 1 for the ideal diode behaviour [93]. The ideality factor (in PSPICE emission coefficient) η is the component introduced in the representation of the real diode - Equation 2.30. Equation 4.2 is an equivalent of Equation 2.29, but with the added ideality factor which takes into account the effect of the generation-recombination centres in the depletion layer. It is also a simplified version of the practical diode equation (Equation 2.30); it ignores the voltage drop across the diode series resistance and the current flow through the diode parallel resistance.

$$I_D = I_{D(ideal)} + I_{(r,g)} \tag{4.1}$$

$$I = I_s\left[\exp\left(\frac{qV}{\eta kT}\right) - 1\right] \tag{4.2}$$

The graphical representation of the electric components used to represent the small bias real diode model is shown in Figure 4.2a. The diode parasitic elements are ignored and the model relies purely on diode equation. The PSPICE form of the diode equation used for this model is shown in table 4.2.

PSPICE equivalent equation	**condition**	
$I = I_s(e^{\frac{qV}{\eta kT}} - 1) + V * GMIN$	for $V \geq -5\frac{\eta kT}{q}$	Fwd bias & Rev bias for $V \geq Vthermal$
$I = -I_s + V * GMIN$	for $V < -5\frac{\eta kT}{q}$	Reverse bias for $V < Vthermal$

Table 4.2: Small bias current of the real diode model

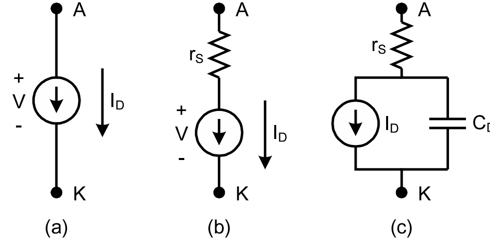

Figure 4.2: Real diode models: (a) small bias, (b) large bias and (c) large signal

Real Diode: Large Bias - the Ohmic Resistance and High Injection Effect

At higher bias levels the diode current deviates from the ideal characteristics due to the series resistance associated with the neutral regions and contacts, as well as due to any resistance associated with high injection level. These parasitic effects are modelled by the ohmic resistance, r_S, as shown in Figure 4.2b. Consequently the potential divider ($V_{DIODE} = r_S I_D + V$) is formed. The diode equations from table 4.2 are reused for this model. However, the voltage across the active section of the device is reduced by the amount of voltage drop across the parasitic series resistance.

Real Diode: Large Reverse Bias - Effect of the Junction Breakdown

When a sufficiently large reverse voltage is applied to a p-n junction, so that the electric field across the depletion region passes the critical breakdown point, then the carrier multiplication effect occurs in the depletion region [90]. This is when a minute increase in reverse voltage magnitude causes significant increase in reverse diode current. In order to include this phenomenon into the diode model, the diode equation becomes of the form shown in table 4.3.

PSPICE equivalent equation	**condition**	
$I = I_s(e^{\frac{qV}{\eta kT}} - 1) + V * GMIN$	$V \geq -5\frac{\eta kT}{q}$	fwd & rev bias for $V \geq Vthermal$
$I = -I_s + V * GMIN$	$-BV < V \leq -5\frac{\eta kT}{q}$	reverse bias up to breakdown
$I = -IBV$	$V = -BV$	at breakdown
$I = -I_s(e^{\frac{q(BV+V)}{kT}} - 1) + \frac{qBV}{kT}$	$V < -BV$	past breakdown

Table 4.3: Large reverse bias current of the real diode model

4.1.3 Large Signal Model

The small signal model with its linearised portions of the diode characteristics is not suitable for simulation where input signals cause large variations in the operating conditions. Consequently, a large signal model is used in order to allow the observation of the diode behaviour in a variety of circumstances.

The key aspect of the large signal diode models is charge storage. If there was no charge storage, the devices would be infinitely fast as there would be no charge inertia and the currents could be changed in zero time [93, pp19] (see 'Capacitance - Voltage relationship' in Section 2.2.3). The charge storage in the depletion region due to concentration of the doping atoms and charge storage due to minority carrier charges injected into the neutral regions are shown in Equations 4.3 and 4.4 [90, 93].

$$Q_j = \sqrt{\frac{2q\varepsilon_S(v_{bi} - V)}{\frac{1}{N_A} + \frac{1}{N_D}}} \tag{4.3}$$

$$Q_d = (Q_n + Q_p) = \tau_D I_D \tag{4.4}$$

The stored charge Q_n and Q_p are defined in Equations 2.40 and 2.41. Combining the Equation 2.32 with the Equations 4.3 and 4.4 the PSPICE proffered versions of the diode capacitances can be derived - Equations 4.5 and 4.6.

$$C_j = \frac{dQ_j}{dV} = \frac{C_j(0)}{\sqrt{1 - \frac{V}{V_{bi}}}} \tag{4.5}$$

$$C_d = \frac{dQ_d}{dV} = \frac{q}{\eta kT}\tau_D I_S e^{\frac{qV}{\eta kT}} \tag{4.6}$$

For reverse bias and small forward bias Q_j is the dominant charge storage. For moderate forward bias and beyond the injected charge Q_d dominates [93]. The crossover of the two types of capacitance dominant behaviours occurs at the low level forward bias. The Equation 4.5 becomes invalid as the voltage across the junction approaches the built in potential. At this point the charge stored in the depletion region is non existent (see Equation 4.3) driving the junction capacitance into theoretical infinity. The diode capacitance is the sum of the two capacitances (Equation 4.7).

$$C_D = C_j + C_d = \frac{d(Q_j + Q_d)}{dV} = \frac{dQ_D}{dV} \tag{4.7}$$

Thus the diode large signal can be represented as in Figure 4.2c. The stored charges Q_j and Q_d that are of the main interest for calculations of the diode capacitance. The PSPICE definition of the stored charge is shown in table 4.4.

where F_1, F_2 and F_3 are SPICE constants determined by the coefficient for the forward bias depletion capacitance formula (FC) and grading coefficient (m) [93] and

$\mathbf{Q}_D=$	$\mathbf{Q}_d$	$+\mathbf{Q}_j$	condition
$Q_D =$	$\tau_D I_D$	$+C_j(0)\int_0^{V_D}(1-\frac{V}{v_{bi}})^{-m}dV$	for $V_D < FC * v_{bi}$
$Q_D =$	$\tau_D I_D$	$+C_j(0)F_1 + \frac{C_j(0)}{F_2}\int_{FC*v_{bi}}^{V_D}(F_3+\frac{mV}{v_{bi}})dV$	for $V_D > FC * v_{bi}$

Table 4.4: PSPICE stored charge definition

are defined as:

$F_1 = \frac{v_{bi}}{1-m}(1-FC)^{(1+m)}$, $F_2 = (1-FC)^{1+m}$ and $F_3 = 1 - FC(1+m)$

As the capacitance is defined as rate of change of charge with respect to voltage change (Equations 4.5 and 4.6), the above charge definitions results with the PSPICE charge characterisations as shown in table 4.5.

$\mathbf{C}_D=\frac{dQ_D}{dV}=$	$\mathbf{C}_d$	$+\mathbf{C}_j$	condition
$C_D =$	$\tau_D\frac{dI_D}{dV}$	$+C_j(0)(1-\frac{V}{v_{bi}})^{-m}$	for $V < FCv_{bi}$
$C_D =$	$\tau_D\frac{dI_D}{dV}$	$+\frac{C_j(0)}{F2}(F3-\frac{mV}{v_{bi}})$	for $V > FCv_{bi}$

Table 4.5: PSPICE diode capacitance

with m being equal to 0.33 for a linearly graded junction or 0.5 for an abrupt junction and FC being a factor between 0 and 1. FC determines the way in which the junction capacitance is calculated when the diode is forward biased. This is required because of the collapse of the theoretical approximation of the junction capacitance as the forward bias voltage approaches the built in junction potential value [93, pp23]. The PSPICE equivalent parameter names for the above equations are shown in appendix B.

4.2 Behavioural Models

The behavioural models are based on the information obtained from experimental observations of LED external behaviour. The proposed relationships between measured variables are confirmed through data analysis (curve fitting). This process yields a set of simple parameters that are consequently used to mimic the established relationships. The amalgamation of a mixture of relationships into an effective unit corresponds to a behavioural model of a device.

Instead of relying on limited standard diode models, the purpose built behavioural models can be created. The models are based on the experimentally obtained relationships between diode current and voltage, capacitance and voltage and current and light intensity. The electrical characteristics of the models are based on the diagram

shown in Figure 4.3. Equation 2.30, derived from this Figure, is used to represent the steady state current flow through the device. The parasitic capacitances are considered for the purpose of predicting the device transient response. It is assumed that the capacitive current does not contribute to the light generation. This assumption is not important when considering the steady state current flow. However, the capacitive current is an important factor when considering the frequency response of the devices. Consequently, large ratio between capacitive and resistive currents can limit or even prevent the fast generation of light.

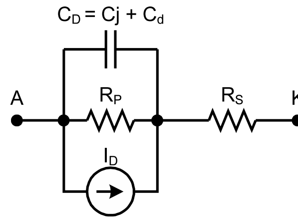

Figure 4.3: Complete practical diode model

The LED optical properties are derived from the experimentally determined current – light intensity relationship. As this relationship is established at steady state conditions it is assumed that the measured current is purely resistive. Therefore, it is assumed that this relationship relates to the resistive current, not device current, even at higher switching speeds when the capacitive current is present.

The model was derived with use of the generally accepted theoretical relationships (Section 2.2). The model parameters are obtained from the curve fittings (described in Section 5.1). The encountered discrepancies between the experimental findings and anticipated theoretical predictions are incorporated into the relationships so that the model evolves accordingly (Section 5.2). The plausible explanations for the discrepancies are sought.

4.3 Chapter 4 Summary

The methods of modelling LEDs were covered in this chapter. These include the standard PSPICE models and the custom built behavioural models. The model parameters are derived from the experimentally determined relationships (Section 5.1). The acquired set of parameters is incorporated into mathematical expressions defined by the final established relationships between the observed variables. The theoretical expressions for the LED characteristics (Section 2.2) were altered to fit the experimentally obtained data. Hence, the models are orientated towards the practical devices as opposed to their theoretical predictions. These are practically realised in OrCAD and MATLAB software packages. The obtained models are dealt with in Section 5.2.

Chapter 5

Experimental and Modelled LED Characteristics

Even though the shape of the LED output pulses is generally governed by the driving signal it is also restricted by the LED characteristics. This is especially the case at higher frequencies as instantaneous switching between the on and off states is not possible to achieve (see Section 3.3). It is the importance of the transient response of the LEDs that has prompted the need for experimental determination of the LED characteristics. The LEDs used in this case are Agilent HLMP-CB15 [128]. These devices have been used in the ANTARES project. They have proved to be the most suitable components available on the market at the time when the ANTARES LED drivers were built. It was decided to continue developing the drivers for the same devices so that any potential improvements can be directly compared to the previous work of the same type.

Section 5.1 looks at the electrical and optical characteristics of the chosen LEDs. These characteristics are relevant for the pulsing operation of the chosen devices. The identified deviations of the experimental characteristics from the theoretically anticipated relationships are analysed. Consequent hypothetical explanations for the discovered differences are presented in this section. Possible effects of the unexpected properties are considered.

Section 5.2 concentrates on generation of LED models based on the experimental findings. Three types of models are generated and their characteristics are compared.

5.1 Methods and Results

The LED characteristics that were found most dominant for the application are tested. The importance of device capacitance for switching characteristics prompted the measurement of the capacitance - voltage relationship. The somewhat indistinct current -

voltage relationship from the manufacturer's data sheet prompted check of this characteristic. The LED output spectrum followed in an attempt to describe certain discrepancies occurring in the previous measurements on the LEDs. A less common determination of LED photo-detection characteristics was conducted amid the attempts to explain the unexpected abnormalities occurring in the other LED characteristics.

Two groups of the LEDs are tested. They are of the same type [128] and are obtained from the same source (FarnellInOne) at two different occasions. It is not known if the LEDs from a group come from the same manufacturing batch. In order to distinguish between the two, the groups are named BATCH-1 and BATCH-2 further in the text. Each batch contains twenty LEDs and they are labelled numerically from 1 to 40.

5.1.1 Capacitance - Voltage Relationship

The importance of the capacitance in LED switching was described in Section 3.3. Consequently the capacitance – voltage relationship is deemed an important characteristic that needs to be determined. The measurements of the internal LED capacitance with respect to the changing voltage across the LED were performed using a Marconi TF1313 Universal Bridge [129]. The voltage is applied with an external bias circuitry – constructed as shown in Figure 5.1. The available measuring frequencies are $1kHz$ and $10kHz$. All the capacitance measurements are obtained at $1kHz$ as this frequency offers improved measurement accuracy [129]. The LED under test forms a part of the bridge as shown in Figure 5.2. The capacitance reading is taken once the currents flowing through different branches of the bridge are balanced using the external controls. The reading represents the capacitance of the device (including the possible package parasitic capacitance). The effect of the parasitic lead capacitance is established to constitute a negligible portion of the total reading. The maximum value of the parasitic capacitance contributes to the total capacitance reading in order of less than 0.34%. The lead parasitic capacitance can be established by physically cutting the top end of the LED enclosure and breaking off the junction prior to capacitance measurement of the remainder of the device.

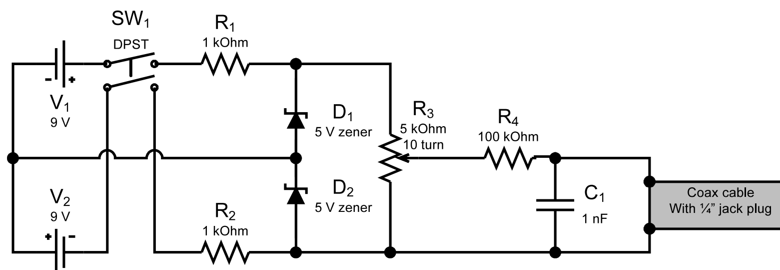

Figure 5.1: Marconi TF1313 bridge bias circuit

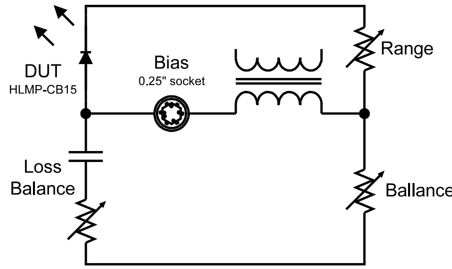

Figure 5.2: Simplified TF 1313A Bridge Diagram

The external bridge bias circuit (Figure 5.1) is constructed in order to extend the bias range for the capacitance measurement. A standard biasing circuit delivers output necessary for reverse bias only ($-4.5V$ to $-1.5V$). Even though the biasing circuit provides swing from $-4.5V$ to $4.5V$ it is not possible to measure LED capacitance above $2V$ bias with this arrangement because of dramatic increase in diffusion capacitance above this bias level. The exponential increase of the current flowing through the device makes it impossible to keep the test bridge balanced because of the exponential rise of the diffusion capacitance.

The effect of the changing *d.c.* bias on the bridge can be investigated in order to establish if the measurements are affected by the bias alterations. This effect is verified with the *d.c.* bias circuit supplying current while no LED is present in the bridge. The maximum change in current provided to the bridge for the voltage supply swing from $-4.5V$ to $4.5V$ is $20nA$. The possible error introduced by this phenomenon is insignificant.

The above measurement procedure is performed on two batches of the LEDs (see Section 5.1). The results are expected to follow the LED behaviour described in Chapter 2.2.3. That is, the capacitance behaviour should follow the relationship from Equation 2.36 (and consequently Equation 2.37) at reverse bias voltages and its trend should be a mixture of the relationship from Equations 2.36 and 2.43 in forward bias region. The exponential behaviour from Equation 2.43 should become dominant at larger forward biases when diffusion capacitance takes over and the junction capacitance vanishes (see Chapter 2.2.3). The experimentally determined C-V relationship is shown in Figure 5.3.

A number of discrepancies between the measured and theoretical C-V relationships is evident from examination of the graphical data (Figure 5.3). The internal capacitance for two LEDs (labelled 39 and 40) is significantly higher that that of the rest of the LEDs, even though their shape is generally comparable. Closer inspection of the remainder of the curves shows a distinctive difference between the curves belonging to two different batches, as shown in Figure 5.4 (the LEDs 38, 39 and 40 are omitted from Figure 5.4b). There are also two distinguishable groups of the curves exhibited by the LEDs in BATCH-1 (Figure 5.4a). There are six curves in BATCH-1 C-V char-

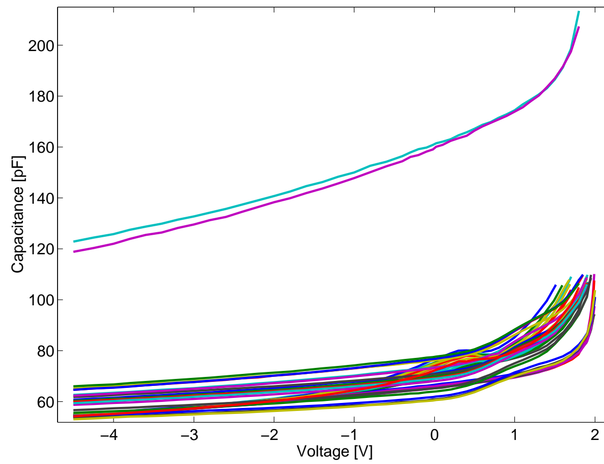

Figure 5.3: Capacitance - Voltage relationship all tested LEDs

acteristic that closely resemble the anticipated form. The reverse bias capacitance for these LEDs appears to have the shape dictated by Equation 2.36 while the forward bias capacitance appears to become exponential as anticipated due to the behaviour of the diffusion capacitance. The remainder of the curves from BATCH-1 exhibit generally similar trend, but with the exception of having a strong inflection point in their C-V characteristic (further in the text these LEDs are called HUMP LEDs and the other six LEDs from BATCH-1 are referred to as NO-HUMP LEDs). The plotted data for the BATCH-2 LEDs shows similar behaviour to those of HUMP group of LEDs with the exception of their hump section being less dominant and shifted to the forward bias. Additionally the capacitance spread of the curves in reverse bias is significantly larger than it is for the BATCH-1 LEDs. In this case the spread is by up to approximately 20% at the highest reverse bias.

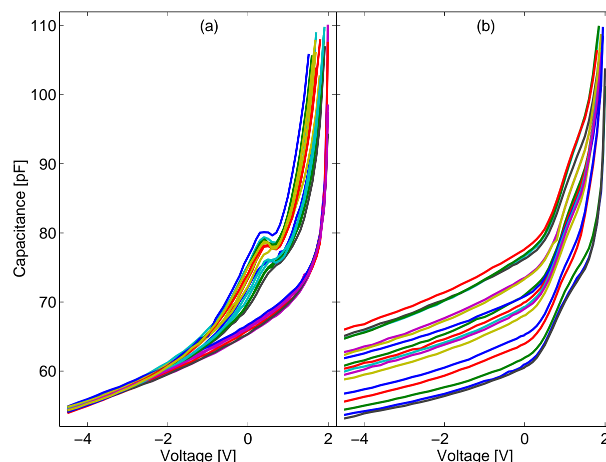

Figure 5.4: Capacitance - Voltage relationship: (a) batch 1, (b) batch 2

There is also an additional curve (LED 38) that considerably deviates from the

general shape adopted by the remainder of the curves (as shown in Figure 5.5).

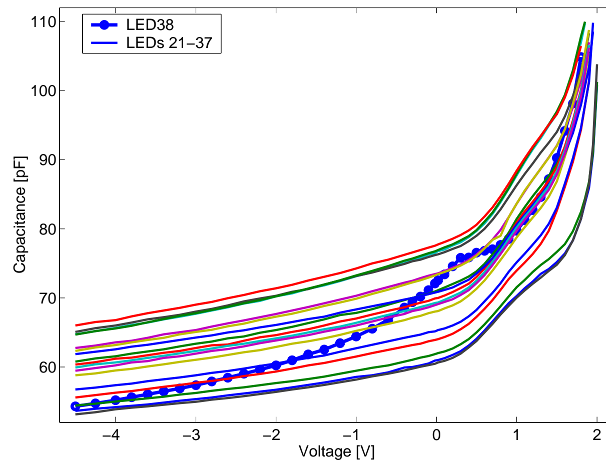

Figure 5.5: Capacitance - Voltage relationship: LEDs 21 - 38

A standard way of representing C-V characteristic is by plotting inverse of the capacitance squared versus voltage (Equation 2.37). As it is only the reverse bias condition that is normally considered, the commonly displayed capacitance is depletion capacitance. Such plot allows extrapolation of LED impurity concentration. This method is not used in this case, but the relevant plot is shown for reference purposes in appendix C.1. It should be noted that the biasing arrangement for the capacitance measurement in this case yields a combination of depletion and diffusion capacitance. The capacitance is tested over the extended bias with the aim of describing the complete behaviour of the LEDs over a range of conditions. It was considered that the diffusion capacitance ought to be included into such investigation. It was also discovered that the understanding of the capacitance behaviour in the low forward bias is not definite. The available models are scarce and slightly ambiguous when it comes to the transfer of dominance from the depletion to the diffusion capacitance at the low forward bias [93]. Hence, an attempt was made to investigate capacitance in this region.

The above analysis is a product of graphical data observations and hence is not exact enough to provide unambiguous conclusions about the discrepancies between the theoretical and practical LED characteristics. The data is therefore analysed further.

From the measurement of the parasitic capacitance (described earlier in this section) it is concluded that this capacitance could not generate such a significant discrepancy between theoretical and practical LED capacitance. Consequently, the parasitic effect is ignored in this analysis. It is assumed that the depletion capacitance is the only relevant contributor to the LED reverse bias capacitance. The combination of the depletion and diffusion capacitances in forward bias generates the LED total capacitance. It follows that the discrepancy between the theory and practice must be a product of one or both of the capacitive components. In order to investigate the reasons for the

unexpected LED capacitance behaviour the capacitive components are reconstructed following the theoretical predictions and fitted to the experimental data. That is, the diode capacitance behaviour (see Section 2.2.3) is modelled and fitted to the measured data. The depletion capacitance is constructed using the relationship from Equation 2.37 and fitted to the measured data (see appendix C.2). The depletion capacitance model values are then subtracted from the measured data and an exponential function representing diffusion capacitance is fitted to the remainder (see appendix C.3). The model of the diffusion capacitance is then subtracted from the first remainder and the second remainder is generated. The shape of the final remainder resembles Gaussian distribution curve and this distribution is found to be adequate for the model (see appendix C.4). The three capacitive components are then added together to form the LED capacitance model (Figures 5.6 - 5.10). The difference between the models and the data is the fitting error shown in appendix C.5.

The above fitting is performed in MATLAB using its unconstrained nonlinear optimization function (fminsearch). It is based on a simplex search method where the stepwise progress is achieved from one feasible solution to another in such a way that the value of the fitting function increases [130]. The initial step is defined by the initial values. The following points depend on the optimality test, which results in a location of possible better feasible solutions [130]. If such location is available, the transition to the new point is completed. The simplex search method specific to MATLAB is defined by Lagarias *et al.* [131]. The comparison of the function values for the new and the old point results in a substitution of the point that is further away from the fitting data. Subsequent points generate the new simplexes. The procedure is reiterated until the diameter of the simplex falls within the specified tolerance level.

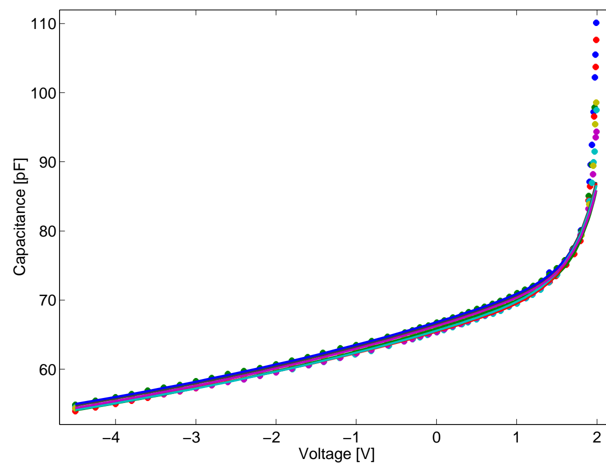

Figure 5.6: Capacitance modelling for NO-HUMP LEDs: *** measured data, ___ model

The main unexpected feature that appears in the measured LED C-V relationship is the hump feature that appears in some of the tested LEDs. A conclusion from

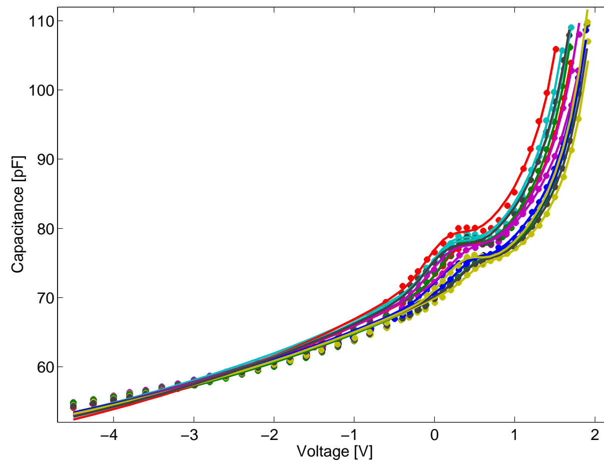

Figure 5.7: Capacitance modelling for HUMP LEDs: *** measured data, ___ model

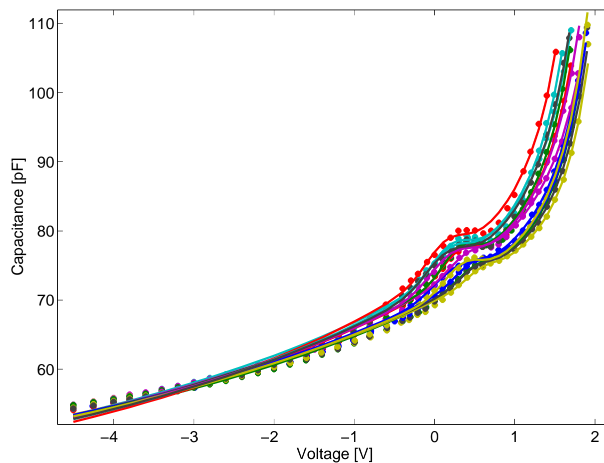

Figure 5.8: Capacitance modelling for BATCH 2 LEDs (21-37): *** measured data, ___ model

the graphical analysis of the measurements suggests that the hump for the BATCH-2 LEDs is less dominant and shifted to the forward bias. The plot of the two humps for the two batches (Figure 5.11) indicates that the reason for the BATCH-2 hump to be less dominant is the exponential rise of the diffusion capacitance in the forward bias, which is where this hump occurs. In fact, when isolated from the other capacitances, the two humps are comparable (Figure 5.11). As the two features are comparable in size and shape it is reasonable to assume that they are the products of a single effect. It is also assumed that the effect would have to be contributing to either of the two dominant LED capacitances as well. Figure 5.11 shows that the hump for the HUMP LEDs partially occurs in the reverse bias while it is purely in the forward bias for the BATCH-2 LEDs. Consequently, as the depletion capacitance is linked with both biases and the diffusion capacitance exists only in the forward bias, it is assumed that the effect that causes the humps is correlated to the depletion capacitance. The

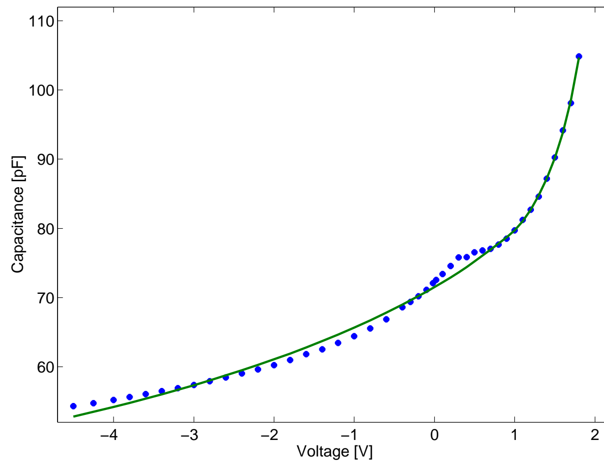

Figure 5.9: Capacitance modelling for LED 38: *** measured data, ___ model

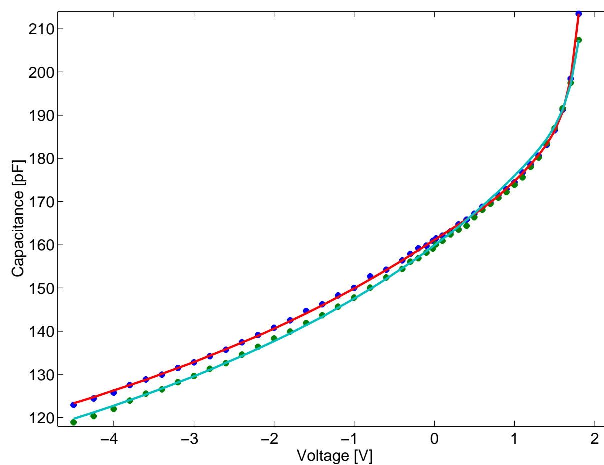

Figure 5.10: Capacitance modelling for LEDs 39 and 40: *** measured data, ___ model

Equations 2.34 to 2.37 suggest that in this situation the only reasonable variable that causes variation in depletion capacitance is depletion layer width. The width is directly controlled by the impurity concentration. Therefore it is concluded that it is the uneven distribution of the impurities in the active layer of the device that cause this hump effect. This is a reasonable assumption considering all the difficulties experienced with the LED manufacture that are still unresolved (see Section 2.1).

It should be noted that the hump characteristic is more consistent for the devices from the BATCH-2 than it is for the devices from BATCH-1. This behaviour is evident from Figure 5.11.

An alternative hypothetical explanation for the existence of the capacitive hump is based on the material structure of the devices. With the reference to Figure 2.10, three distinctive sections are identifiable in the active region of this device. Those are the SQW itself and two isotype junctions (GaN-AlGaN), one on each side of the SQW. Each one of those sections can be roughly represented by the model of Figure 4.3.

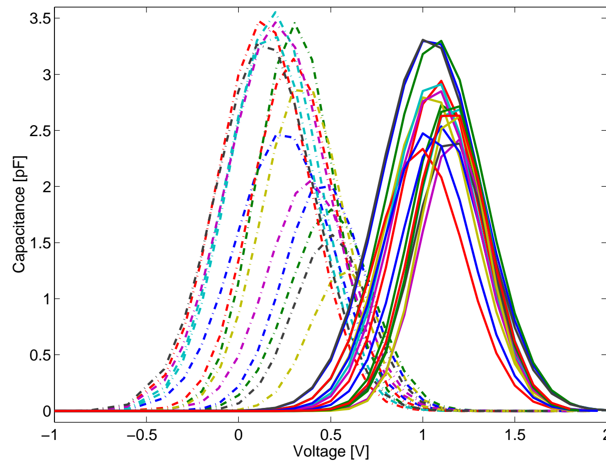

Figure 5.11: Capacitive hump comparison: _. HUMP, __ BATCH 2 (LEDs 21 to 37)

When the device is reverse biased its current source, the series resistance and the diffusion capacitance can be neglected. Therefore the structure is electrically characterised by a RC network as the identified sections are connected in series. The complexity of the model increases if the junctions are to be accurately represented. The isotype junctions can be modelled as back-to-back diodes and consequently each of those is shown as a series connection of two parallel resistor-capacitor combinations [132]. The SQW is modelled as a series capacitive network with an additional parallel capacitance [133]. If taken in very simple terms, the device consists of three capacitive sections. Each one of those should contain certain amount of depletion capacitance when the device is reverse biased. As the bias approaches zero voltage the two side capacitances are potentially likely to colapse earlier than the SQW capacitance. This means that these two side capacitances would increase in value (to theoretical infinity) and then suddenly collapse as their local depletion capacitance disappears and the local diffusion capacitance becomes dominant. This type of effect could theoretically generate the observed local maxima in the capacitance of the complete device. If so, this hypothetical analysis further confirms that the existence of the humps is generated by the depletion capacitance.

The importance of the LED capacitance can be further emphasised by the observation of the optical output generated by the devices with different capacitive characteristics. It is established that the LEDs with significantly increased internal capacitance (numbered 39 and 40) generate similar fast switching optical pulses as the other devices, but they need higher driving voltage in order to generate fast switching light. The required increase in driving signal voltage is in order of 26% to 28%. The irregularities in the capacitive properties could potentially prevent the generation of fast switching light. (The findings are generated using the circuits from Chapter 6).

5.1.2 Current - voltage relationship

Measurement of the LED I-V characteristic was performed indirectly by measuring the voltage drops across the LED and across a series resistor (Figure 5.12). The voltage drop across the series resistor is converted into current flowing through the LED.

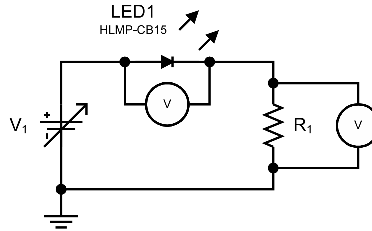

Figure 5.12: I-V characteristic - experimental setup

The experimentally determined I-V characteristic is shown in Figure 5.13. The same is shown on logarithmic scale in Figure 5.14. The graphical data in Figure 5.13 shows reduced current flow through the LEDs from BATCH-1 at higher voltages. Additionally, the low bias behaviour (Figure D.1 – appendix D) depicts the differences between the three groups of LEDs. The NO-HUMP group conducts the lowest amount of current for a given low-level voltage. This is followed by the HUMP LEDs. The current flowing through the BATCH-2 LEDs for the same voltage level is significantly higher. This can be seen in Figure 5.14, but is clearer when shown on linear scale up to a fixed bias voltage point (Figure D.1).

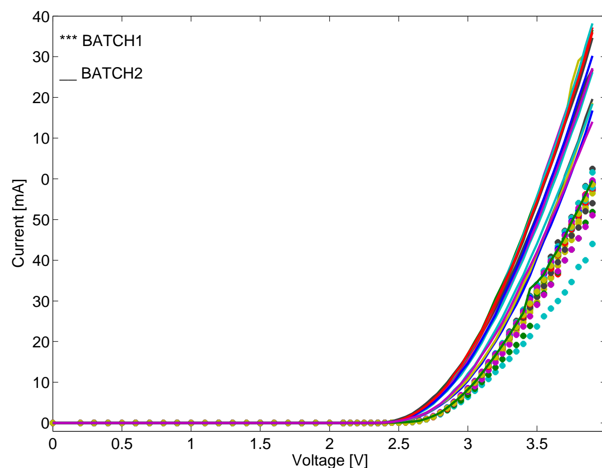

Figure 5.13: LED I-V relationship

The comparison of the two logarithmic scale relationships would suggest irregular behaviour of the LEDs. Assuming that the LED current is exponential, the logarithmic scale of this relationship should generate a linear graph. However, two very distinct knees are evident. These can be explained by considering the practical blue LED characteristics (Equation 2.30). The mathematical analysis of the equation (appendix A.2)

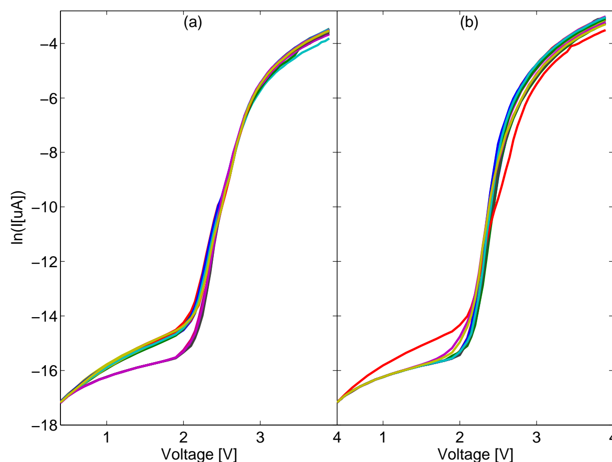

Figure 5.14: LED logarithmic I-V relationship: a) BATCH1, b) BATCH2

results in the simulated practical diode I-V relationship shown in Figure 2.6. This Figure exposes that the voltage drop across the diode series resistance and the current flow through the diode parallel resistance de-linearise the expected theoretical I-V relationship. The experimentally determined I-V characteristic resemble the relationship shown in Figure 2.6. The inspection of the I-V relationship (appendix A.1) provides an insight into linear sections of the relationship. The knees are formed in the areas where the linear sections have comparable dominance over the I-V relationship.

The I-V fitting procedure employs the identical method as the C-V fit. It uses MATLAB unconstrained nonlinear optimisation function (fminsearch). The initial fitting attempt used the standard diode equation (2.29) and its practical derivative (4.2). The generated fitting error is expectedly considerably large as the experimental data (from Figure 5.14) is clearly not dominated by the exponential behaviour as those two equations are. The practical diode equation (2.30), which accounts for the voltage drop across the series LED resistance and the current flow through the parallel diode resistance, is used for the fit instead. The equation is applied in the form described by the Equation A.26 from appendix A.2. The new fitting error is considerably improved in relation to the error generated by the previous attempt. The logarithmic scale analysis of the fitted data shows that though the model is relatively acceptable, it does not fit the data to the same level of accuracy for all devices. It was concluded that this issue arises from the execution of the fitting method in MATLAB rather than from the model inaccuracy. The fitting is therefore improved by fitting the logarithmic value of the expression from Equation A.4 to the logarithmic value of the measured diode current. The resulting error is reduced on both scales, linear and logarithmic. The result of the fitting procedure is the derivation of the practical diode defining parameters for the LEDs in question. The parameters are saturation current, ideality factor and diode series and parallel resistance. The plots of the parameters for different devices are

shown in appendix D. The parameters for the previously identified LED groups are shown using different symbols so that the parameter variations for different groups are evident. The parameters are later used for the correlation analysis in Section 5.1.6.

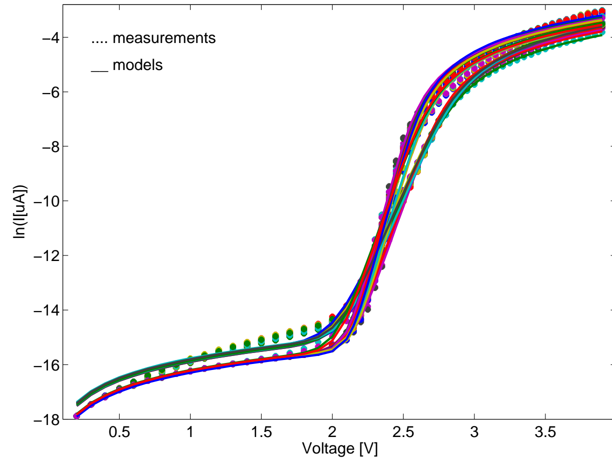

Figure 5.15: LED equation model: ln(I) - V

5.1.3 LED Output Spectrum

The relative light intensity is measured with respect to the LED emission wavelength. The narrow sections of the wavelengths emitted by the LED are selected by a spectrophotometer and the intensity is measured for the selected wavelength. The coupling between the LED and the spectrophotometer is not adequate for comparison of the output power for different LEDs. However, the experiment is capable of providing sufficiently accurate measurement of the relative light output versus output wavelength.

The LED relative output spectrum is shown in Figure 5.16. The spectrum is experimentally measured in order to identify possible discrepancies between the LEDs used in the previous sections of this chapter. The aim is to check on possible emission variations caused by the same phenomena that result in differences in the C-V relationships. It is determined that the peak emissions appear at approximately the same wavelength within an accuracy of $4nm$. The approximate investigation shows that the slight wavelength shifts of the peak emissions do not appear to be correlated with the previously established device groupings. This central wavelength for which majority of the peaks happen ($472nm$) is identical to that stated in the LED data sheet [128].

The skewness and kurtosis of the emission spectrum are examined. The two distribution properties are considered for the purpose of examining if the optical spectrum is possibly influenced by the previously identified physical irregularities. The skewness is the distribution third moment and is defined in Equation 5.1 [134]. It is the measure of distribution symmetry. A positive skewness value identifies distribution stretching farther to the right, while a negative value represents distribution with the values smaller

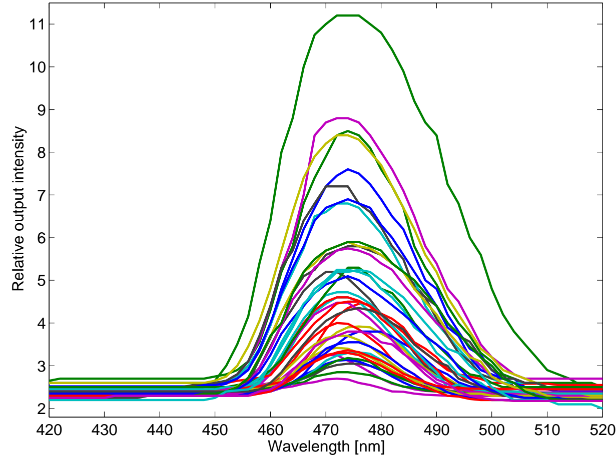

Figure 5.16: LED output spectrum

than mean value being more dominant [134]. The kurtosis is the distribution fourth moment defined by Equation 5.2 [134]. It describes the peak of a distribution. A large positive kurtosis value is related to a very sharp peak while a large negative value describes relatively flat peak [134]. The Gaussian distribution has both a skewness and kurtosis equal to zero.

$$Skew = \frac{1}{N}\sum_{i=1}^{N}\left[\frac{x_i - \bar{x}}{\sigma}\right]^3 \tag{5.1}$$

$$Kurt = \frac{1}{N}\sum_{i=1}^{N}\left[\frac{x_i - \bar{x}}{\sigma}\right]^4 - 3 \tag{5.2}$$

The skewness and kurtosis of the examined LEDs are shown in Figure E.1 of appendix E. Generally, there is a very little difference between these parameters for the previously identified LED groups. Regardless of the apparent missing link between these parameters and the already identified LED groups, these parameters are used for the correlation analysis in Section 5.1.6.

5.1.4 Current - Output Light Intensity Relationship

The relationship is established by measuring the intensity of the light emitted through the internal LED lens to the front of the device. Minor mechanical adaptations are performed in order to achieve adequate light coupling from the LEDs into the photodetector. It is ensured that no light escapes from the path between the LED and the photodetector. The light that is emitted through the back panel of the LEDs is not collected. The back panel light is let to escape as it is aimed to measure the amount of frontally emitted light. The optical power detected by the detector is used to express the LED intensity. The voltage dropped across a 100Ω series resistor is used to

calculate the current flowing through the LEDs. All the measurements are performed with the measuring wavelength window being set to $472nm$ - the LED peak emission wavelength.

It is expected that the measurements would generate graphs showing approximately linear relationship between the amount of current flowing through the LEDs and their optical output. This approximately linear behaviour is commonly subject to a linear approximation. The results shown in Figure 5.17 confirm that this approximation is possible.

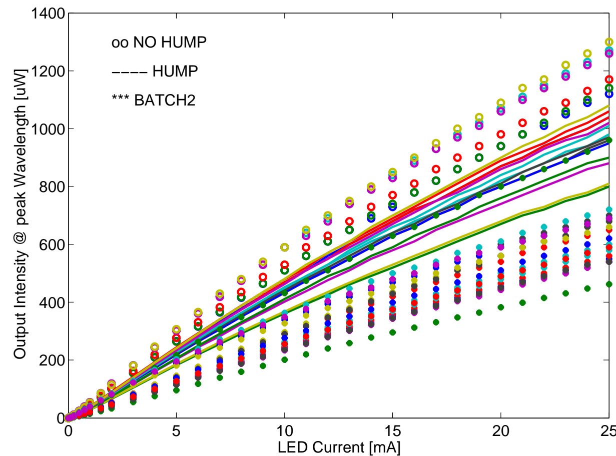

Figure 5.17: LED output light intensity for varying current at peak emission wavelength

The results, presented in Figure 5.17, show the additional discrepancies between earlier identified LED groups. The inspection of the results shows that the NO-HUMP LEDs provide higher optical output intensity than the LEDs from the HUMP group do. Additionally BATCH-2 LEDs emit fewer photons for a set current flow than it is the case with the LEDs from BATCH-1. The observations are statistically analysed using the curve fitting. It is assumed that the relationship between the LED current and intensity should be roughly linear (see Section 2.2.4). The linear approximations are fitted to the above measurements. The slopes of the linear approximations are shown in Figure F.1 of appendix F. The previously identified LED groups are further reinforced with these results as there are clear differences in gradients between different groups shown. The identified intensity gradients are used in the correlation analysis in Section 5.1.6.

5.1.5 LED as a Photodetector

The $250W$ light bulb incorporated in a slide projector is used as a light source in the experiment because of the high light intensity that is provided by this source. The light output from the projector is collected by a lens and is focused at the monochromator

input. After calibration and accounting for a possible error in the form of wavelength shift, the monochromator is controlled externally by Spectrometer Control And Data Acquisition System software (SCADAS). This is a single beam scanning spectrophotometer controlled by a PC. The wavelength of the output light is scanned from 350nm to 500nm in steps of 5nm. The light is passed through the series of filters in order to remove unwanted higher spectral orders transmitted by the grating [135]. This output light from the monochromator falls onto the LEDs and the potential developed across the LED (DUT) is measured with a Digital Voltmeter (DVM). All of the components in the experiment are aligned on an optical bench. The experiment is conducted in a darkened environment in order to avoid interference from the external light sources with the measurements. The system configuration is shown in Figure 5.18. The purpose of the experiment is to compare the photogenerated LED voltage-wavelength relationships. The aim is to identify possible groups of curves that might overlap with the groups that emerged from the C-V measurements from Section 5.1.1.

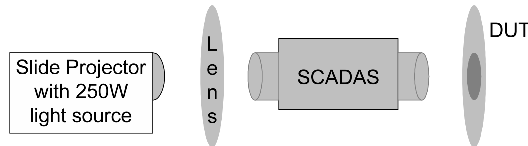

Figure 5.18: LED as a photodetector - measurement setup

The measured results are shown in Figure 5.19a. The measured voltage levels vary by a factor of four at their peak levels. It is assumed that the variations are due to inaccurate device coupling. The variations are most certainly not related to the previous device grouping. The curves are normalised with respect to the peak detected voltage. The measured values are represented as a percentage of the relevant peaks. The normalised results are shown in Figure 5.19b. The peaks for 38 of the devices occur at 420nm (with 2.5nm accuracy). Two curves that peak at 425nm and 430nm are detected by LED 39 and 40. These two devices exhibit significantly increased internal capacitance. The visual curve inspection indicates that there are two distinct groups of slopes related to the BATCH-1 devices (see Figure G.2 - appendix G). The two groups correspond to the two groups that emerged from the C-V measurements (i.e. HUMP and NO-HUMP).

The most concerning issue arising from the above measurements is a significant wavelength shift for the peak emission and detection. The peaks of the emitted spectra, which occur at 472nm, shift to 420nm when the LEDs are used as photodetectors. This considerable and somewhat unexpected shift is assumed to be caused by the bulk InGaN used as the active layer in the LEDs. It is reported that the blue LEDs exhibit this wavelength shift [136]. This property can be exploited if the LEDs are used as wavelength selective photodetectors. The photodetection spectra is reported

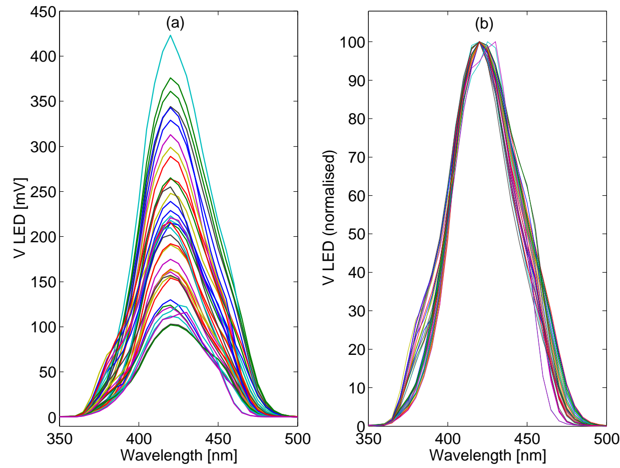

Figure 5.19: LED used as photodetector: a) as measured, b) normalised output voltage

to coincide with the pulsing emission spectra of the devices [136].

The skewness and kurtosis of the above curves is determined in the same manner as with the LED output spectrum in Section 5.1.3. The resulting values for these parameters are shown in Figure G.1 in appendix G. In addition to determination of these values, the curve fitting is also performed on the measured data. The curve fitting is presented in appendix G.

5.1.6 Correlation

The most evident unforeseen characteristic generated by the experimental determination and analysis of the LED physical properties is the hump appearing in the LED C-V characteristic. The inconsistent behaviour of the hump and its possible effect on LED functioning is of a particular interest. It is also believed that the observation of such an unwanted property could improve our understanding of the manufacturing processes of the devices. Assuming that this property appears on regular basis, it is proposed that the observation of this theoretically unpredicted property could potentially be exploited for quality control purposes.

A conclusion from the analysis of the C-V characteristic (Section 5.1.1) is that this anomaly is caused by the varying impurity concentration. It is reasonable to expect some crystal imperfections considering that the crystallography of the materials used for manufacture of these devices is yet to be perfected (Section 2.1). The inconsistent impurity concentration causes uneven depletion layer width variation for an even change of biasing voltage. This could potentially create anomalies as the one detected in this case. This hypothesis (detailed in Section 5.1.1) is analysed further.

As hump causes the capacitance of the NO-HUMP LEDs to be smaller than that of the HUMP LEDs at low forward bias it follows that the NO-HUMP LEDs should also have wider depletion layer width. The wider depletion layer width is externally

observed by the need for larger biasing voltage for conduction of the same amount of current (Figure D.1 in appendix D).

The additional argument that potentially supports the above hypothetical reasoning for the capacitance anomaly comes from the observation of the curves generated by the LEDs when operating as photodetectors. This mode of operation relies on the incident photons delivering sufficient amount of energy to the electrons in the valence band so that they are knocked out to the conduction band. The generated free electron-hole pairs result in a current. There is a possibility that a non-uniform doping concentration in the material alters the number of electrons in the conduction band being capable of absorbing a photon of certain energy. Such phenomenon would alter the absorption spectrum of the devices and hence the uneven non-Gaussian curves would be produced as a result of the LEDs being used as photodetectors. There is a possibility that the irregularities in the curves obtained by the LEDs when they are absorbing light (appendix G) are caused by this non-uniform impurity concentration.

The relationships between different parameters drawn from the LED experimental data are analysed. The parameters used for this analysis are listed in table 5.1. They are sorted in a 40×16 matrix. The rows of the matrix represent the individual devices and the columns are reserved for various parameters from table 5.1. The analysis is preliminarily performed on all 40 devices, but is then reduced to 37 of them. The analysis proved that the considerably atypical behaviour of the last three devices significantly alters the correlation between the LED parameters. They are therefore excluded from the correlation analysis and the size of the parameter matrix is therefore reduced to 37×16.

The matrix is first normalised so that any possible systematic error is removed from the data. The normalised data is then analysed using singular value decomposition. This method generates a diagonal matrix S of the same dimension as the input data matrix and two orthogonal unitary matrices: U and V. The diagonal elements of the matrix S are non-negative and are sorted in decreasing order. These elements are also the singular values of the original parameter matrix. The singular values are defined as a square root of the eigenvalues of the product between the original matrix and its transpose. The decomposition properties are such that the following relations are satisfied $A = U * S * V^T$ and $S = U^T * A * V$ where A is the original input data matrix. The algorithm used by MATLAB for calculation of the singular value decomposition is defined by Anderson *et al.* [138]. The results of the singular value decomposition are shown in Figure 5.20. The horizontal axis is formed by the strongest eigenvector (first column of U matrix). The second strongest eigenvector is plotted on the vertical axis (second column of U matrix). The plotted data shows that a result of the statistical analysis is a distinctive LED clustering. The generated clusters coincide with the groups of LEDs that were originally identified through the capacitance measurement,

LED Characteristic	Source
Built in voltage	Depletion capacitance fit
Scaled impurity concentration	Depletion capacitance fit
Scale of diffusion capacitance	Diffusion capacitance fit
Diffusion capacitance exponential coefficient	Diffusion capacitance fit
Hump amplitude	Hump capacitance fit
Hump position	Hump capacitance fit
Hump standard deviation	Hump capacitance fit
Saturation current	I-V fit
Internal series resistance	I-V fit
Ideality factor	I-V fit
Internal parallel resistance	I-V fit
Emission spectrum skewness	Output spectrum distribution analysis
Emission spectrum kurtosis	Output spectrum distribution analysis
Intensity gradient	Current - Intensity fit
Photodetection skewness	Absorption spectrum analysis
Photodetection kurtosis	Absorption spectrum analysis

Table 5.1: Correlation Parameters

but then also confirmed through the rest of the experimental inspection.

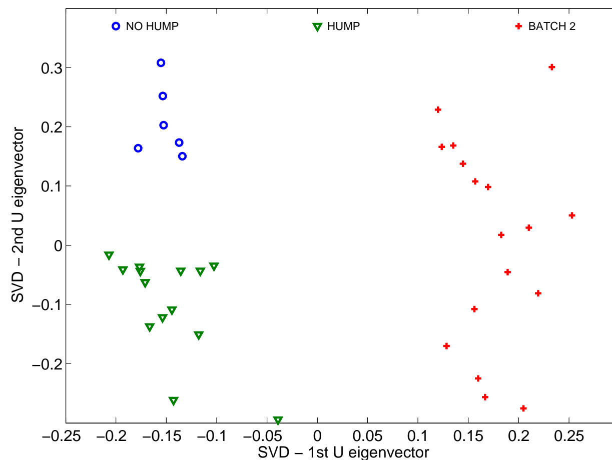

Figure 5.20: SVD analysis of correlation parameters

The correlation for the parameters of table 5.1 is also established. The correlation coefficients are determined on the normalised values of the above parameters. The list of strongly correlated LED parameters is shown in table 5.2. The correlation coefficients with absolute values of over 0.75 are considered.

The key elements sought from the resulting correlation coefficients are the relationships between the capacitive humps and the standard LED parameters. The results of the correlation analysis show the reasons for the existence of the capacitive hump. Table 5.2 shows that the strongest hump correlation is expressed towards the impurity

Coefficient	Parameters	
0.9851	Emission spectrum skewness	Emission spectrum kurtosis
-0.9760	Scale of diffusion capacitance	Diffusion capacitance exponential coefficient
0.9735	Hump position	Scaled impurity concentration
0.9249	Hump position	Built in voltage
0.9193	Scaled impurity concentration	Built in voltage
0.9026	Scale of diffusion capacitance	Scaled impurity concentration
0.8713	Photodetection skewness	Photodetection kurtosis
0.8539	Hump position	Scale of diffusion capacitance
-0.8517	Internal series resistance	Scale of diffusion capacitance
-0.8516	Intensity gradient	Scale of diffusion capacitance
0.8506	Scale of diffusion capacitance	Built in voltage
-0.8457	Diffusion capacitance exponential coefficient	Scaled impurity concentration
0.8397	Intensity gradient	Diffusion capacitance exponential coefficient
0.8367	Intensity gradient	Internal series resistance
0.8111	Internal series resistance	Diffusion capacitance exponential coefficient
-0.8027	Diffusion capacitance exponential coefficient	Built in voltage
-0.7889	Internal series resistance	Scaled impurity concentration
-0.7852	Hump position	Diffusion capacitance exponential coefficient
-0.7697	Ideality factor	Internal series resistance
-0.7540	Internal series resistance	Built in voltage
-0.7532	Internal series resistance	Hump position

Table 5.2: LED parameters correlation coefficients

concentration and is followed by the relation to the built in voltage. Both of those parameters are extracted from the depletion capacitance fit. This confirms the previous suggestion that the hump is a result of the depletion capacitance. It also supports the assumption that the hump is directly caused by a possible abnormality in the impurity concentration. The slightly weaker correlation of the capacitive hump position to the LED diffusion capacitance parameters would mean that the hump is linked to either LED current or the minority carrier lifetime (considering that the charge that causes the diffusion capacitance is a mathematical product of the two). The minority carrier lifetime and the diode series resistance, to which the hump is correlated in a lesser degree, are potential results of the material impurities. This correlation analysis reinstates the previous conclusion that the potentially non-uniform impurity concentration has generated the capacitive humps.

5.2 Modelling Results

The theoretical basis of the models is presented in Chapter 4. The used modelling software packages are OrCAD and MATLAB. The intention is to generate LED models in order to help determine the requirements for the LED driving signals. The generated models are presented in this section.

5.2.1 OrCAD Model Editor

The standard PSPICE (OrCAD) diode models are defined by the generally accepted diode theory (Section 4.1). The selected parameters are responsible for appropriate representation of the real device. However, optical devices are not supported. This limitation generates the need to reuse the existing signal diode models for creation of an adequate representation of the optical devices. This is achieved through the use of the supplementary circuitry.

The LED model in this case is based on the use of diode current as a defining parameter for the optical characteristics of the device. The light intensity is defined in terms of the current flow. This is relatively simple to achieve for a steady d.c. signal. However, the fast signal transitions proposed in this work demand the inclusion of the device capacitance into the model. This is performed with the use of two signal diodes connected in parallel (as shown in Figure 5.21). The two signal diodes have a very similar set of the parameters, all of which are obtained with the use of the OrCAD model editor. However, diode D_1 is used to model electrical characteristics while diode D_2 models its optical performance.

Diode D_1 allows undisturbed electrical operation of the LED driving circuit. This is achieved by an inclusion of the capacitive parameters into this part of the model

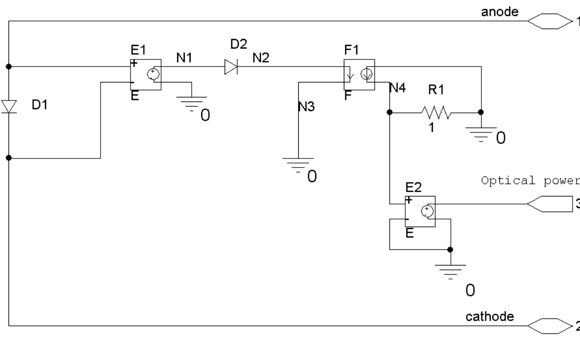

Figure 5.21: LED model - using OrCAD model editor and schematic entry

so that the optical transient response of the model is realistic. These parameters do not contribute to the light generation. The diode D_2 is buffered from the rest of the model by the use of voltage controlled voltage source E_1. This allows for mathematical manipulation of the voltage dropped across the diodes with no interruption to the driving circuit. As the cathode of the diode D_2 is connected to ground through the current controlled current source (F_1) the two diodes are effectively connected in parallel. The current that flows out of F_1 is then converted to optical power. The constant of proportionality between the current and light intensity is equal to unity for graphical purposes. The real constant of proportionality varies for different devices and is implemented with the use of a mathematical expression in the PSPICE netlist. The resulting PSPICE netlist is shown in the appendix H. The parameters derived from the model editor and used to describe the LEDs are shown as a part of the .LEDMOD statements.

5.2.2 OrCAD Behavioural Model

The generated OrCAD behavioural model relies on Equation 4.2. A large signal real diode model (Figure 4.2c) is implemented. It relies on current-voltage, capacitance-voltage and current-light intensity characteristics. This approach allows observation of the effects that each specific LED parameter has on the performance of the device as a whole. The prospective use of the model in PSPICE environment potentially enables assessment of the electronic driver behaviour with specific changes in the LED characteristics.

The experimental curve fitting is performed. As the current equation is simplified, it was found that the saturation current is dependant on the voltage applied to the device. This is anticipated as the diode parallel resistance is ignored in the diode equation used in this case. The junction capacitance is fitted as in Equation 5.3 (x_a is a scaling factor), which corresponds to the theoretical Equation 2.36. The diffusion capacitance is expected to be exponential and is modelled as in Equation 5.4, where

x_b and x_c are scaling factors. The resulting diode internal capacitance is modelled as a current source. The value of the current, sourced by the capacitor, is derived as in Equation 5.5 where $C(V)$ is the intrinsic capacitance and is a sum of the junction and diffusion capacitances. The current-intensity relationship is approximated to be linear.

$$C_j = x_a\sqrt{\frac{1}{v_{bi} - V}} \tag{5.3}$$

$$C_d = x_b \exp(x_c V) \tag{5.4}$$

$$I_C = C(V)\frac{dV}{dt} \tag{5.5}$$

The parameters obtained from the fitting procedure are employed in the LED model shown in Figure 5.22. These parameters are related to a specific device and would change for a different type of LED. However, the model itself should generally be applicable to devices of the same structure.

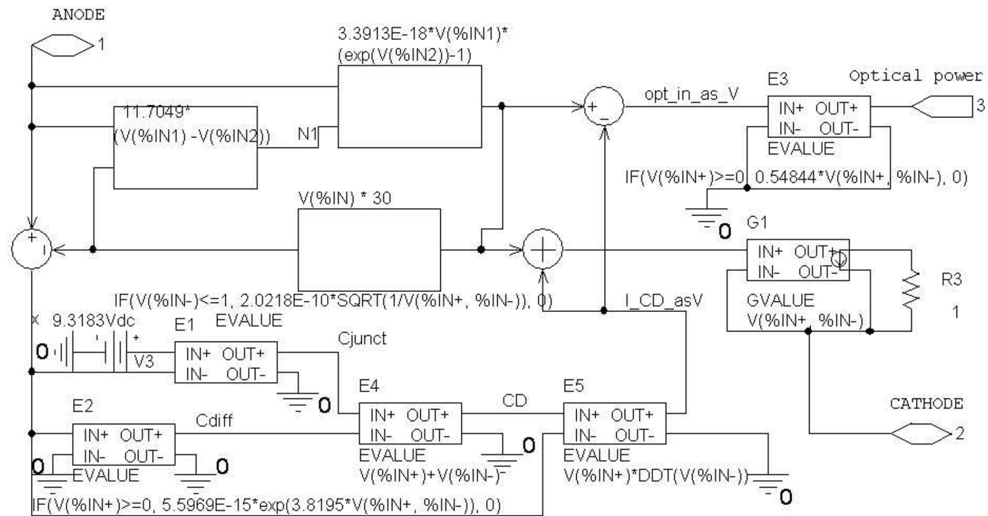

Figure 5.22: LED behavioural PSPICE model

The current flowing from the diode's current source is modelled mathematically with the use of the three blocks in the top left corner of the model. The voltage drop across the internal diode dynamic resistance is subtracted from the device voltage. The resultant is used as an input for the calculation of the capacitive current. The capacitance is represented in the form of current source (Equation 5.5). The junction and diffusion capacitances are modelled by the blocks E_1 and E_2 respectively. The outputs from those two blocks are true capacitances. The two are added by the block E_4, whose output represents the total device capacitance. This is multiplied by dv/dt, inside block E_5, in order to represent the capacitance as a current source. This current is added to the modelled diode current and the resultant current flows out of the device through the cathode. The same capacitive current is also subtracted from the diode's current source current and manipulated further (E_3) in order to obtain optical power

at 'Optical Power' port.

The main limitation of the model results from incomplete modelling of the diode equation. This would have been acceptable had the modelled device been a p-n homojunction. However, the issues brought in with the use of heterostructure limit the usability of the model. This is specifically noticeable in terms of parallel diode resistance. The additional shortcoming of the model is that the capacitive hump is not modelled. The reason for exclusion of this feature is that the original intent was to model a device that would be used for circuit optimisation and the hump was considered as an accidental feature that could be ignored.

5.2.3 MATLAB Behavioural Model

The model orientated towards the numerical analysis is based on the model of Figure 4.3 and is constructed in MATLAB (Simulink). The advantage brought in by this model is its increased computational power and improved accuracy. This is particularly evident in the diode equation where Lambert-W function (defined in [137]) is used in order to improve the modelling parameters and provide more realistic representation of the device. Consequently the parasitic resistances, which play a significant role in the blue LEDs, are accounted for. The basis of the model is very similar to the one of the PSPICE behavioural models. However, the emphasis in this case is put on the particular physical parameters so that their influence on the device performance can be observed in isolated situations. The top layer of the model is shown in Figure 5.23. Figure 5.24 presents a lower modelling layer which is responsible for the evaluation of the LED steady level d.c. behaviour. The other low layer, shown in Figure 5.25, is used to determine the capacitance and the capacitive current generated by the device when experiencing fast changing driving signals. The capacitive behaviour is derived in the same manner as for the PSPICE behavioural model. That is, Equations 5.3, 5.4 and 5.5 are reused in order to determine the two capacitances and the capacitive current respectively. If the hump behaviour is detected in the LED capacitance – voltage characteristic, then the model section shown in Figure 5.26 is added to the layer shown in Figure 5.25. The hump capacitance is in that case added to the other two LED capacitances.

5.2.4 Model Comparison

The modelling in this case was used as an auxiliary tool that carried the potential of enhancing the optimisation of the electronic circuit design. As it was intended to be used as a helping tool the modelling experienced few unexpected turns. The resulting models were not utilised to the originally planned extent, but have proved to be valuable in terms of understanding of the LED performance. The differences

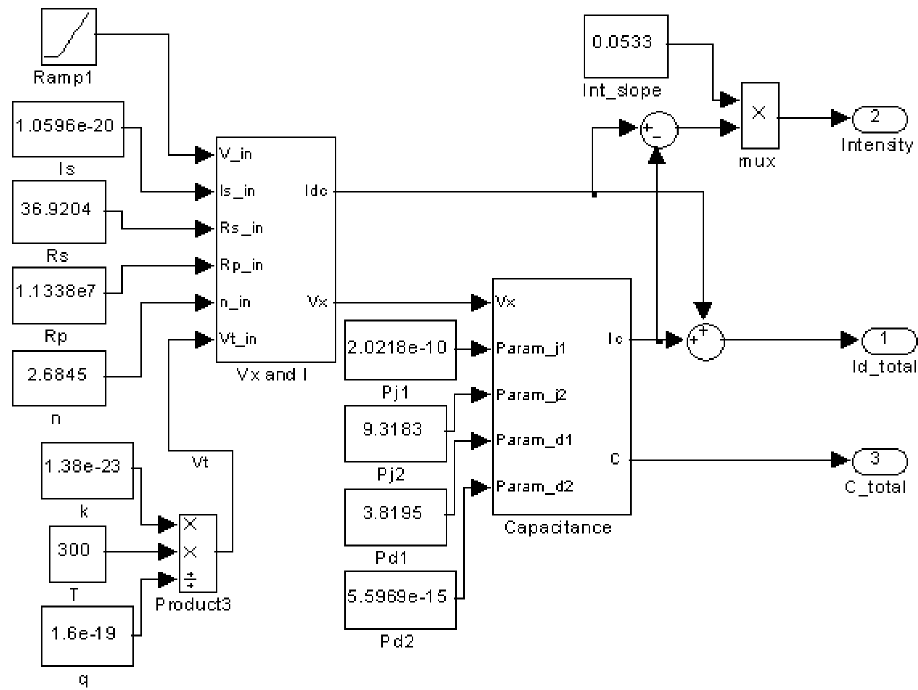

Figure 5.23: LED behavioural MATLAB model - top level

between the resulting three models are a product of this need for study of the specified device and its performance.

The OrCAD (editor) model is a product of the software package, which does not support the optical devices. The additions to the existing signal diode models allow certain amount of integration of the optical devices with this admirable circuit design orientated package. The result is a model that is of adequate quality for standard applications where the LEDs are not driven by fast switching signals. However, the use of the model editor reduces the user controllability. This is because the model editor uses the standard theory to predict the behaviour of the device (as described in Section 4.1). Consequently the model is a crude representation of the real device if it is to be driven by the fast altering signals. This limitation of the model was improved by the OrCAD behavioural model, which allows greater control of the specific characteristics of the modelled devices. At the same time, the usability in the circuit simulation environment is maintained. Consequently, this model is a more realistic representation of the LEDs in question. However, the mathematical limitations of the software package prevent the accurate modelling of the LED current equation. This should not be the case had the standard p-n homojunction device been used. The problem is possible to resolve in OrCAD, but it was considered at the time that the benefits to the project would be more significant if MATLAB was employed. Consequently, the final model is the most accurate of the three in terms of diode equation and the diode internal

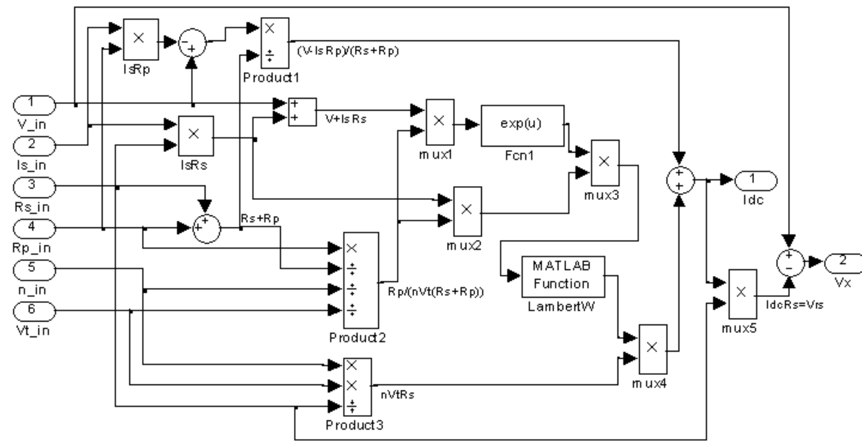

Figure 5.24: LED behavioural MATLAB model - steady current and internal voltage block

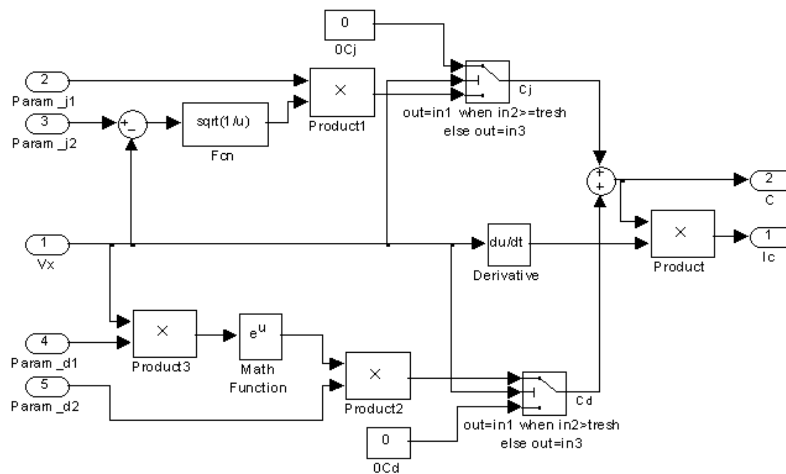

Figure 5.25: LED behavioural MATLAB model - capacitance and capacitive current block

capacitance.

5.3 Chapter 5 Summary

The LED characteristics were considered in this chapter. They are important because they largely determine the characteristics of the optical output. The LED capacitance is considered in detail, as this characteristic can potentially limit the generation of light. This is established theoretically, but is also evident from the fact that some of the devices that fail to produce fast light pulses also have increased capacitance. The unforeseen abnormalities in the LED capacitive behaviour are analysed and it is concluded that these are generated by inability to provide tight control of the crystal formation during the manufacture of the LEDs.

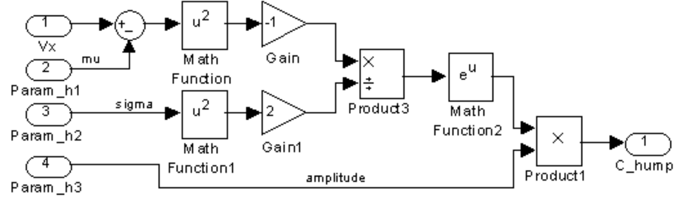

Figure 5.26: LED behavioural MATLAB model - auxiliary hump capacitance block

The modelling results were also described in this chapter. The device modelling became a part of the research as a result of standard design procedure. It was originally intended to generate LED models in order to help determine the electrical pulses that would be adequate for the specified optical pulse generation. The use of the models was considered for the circuit optimisation. The early simulations showed a significant improvement in circuit performance. However, this success could not be matched experimentally. It was concluded that the inadequate modelling of the parasitic properties of the circuits prevented realistic representation of the circuitry. This difficulty experienced with the circuits' parasitic properties was the reason for abandonment of this strategy. The software package used for the simulations is OrCAD. The models are completed in this package as well as in MATLAB, but they were not exploited to the originally planned extent.

Chapter 6

Optical Pulse Generation

The PMT array used in ANTARES requires regular calibration. This is achieved using a pulsed LED, which is electronical switched at high speed (Figure 3.1). The circuit drives a blue LED when triggered by a microcontroller request. The optical flashes produced are designed to mimic the Cherenkov radiation emitted by a muon. The existing electronic switching cicuits are studied and techniques for enhancing their performance are investigated. The switching principles of the circuit operation are confirmed through the simulations (Section 6.1). A totem pole configuration (Section 6.2) is devised. However, in practice this circuit failed to meet the expected performance. The further improvements to the driver are in Section 6.3. The same principles are reused for multiple optical output generation (Section 6.4).

We have concentrated on use of blue LEDs because they are appropriate for our application. Blue LEDs are among the most difficult LEDs to pulse because of their large energy bandgap and high internal capacitance. This leads to an assumption that our techniques will be applicable to LEDs emitting at longer wavelengths. We have preliminarily checked this assumption by applying our techniques to inexpensive off the shelf $5mm$ and $3mm$ green, yellow and red LEDs. The devices generate fast optical pulses as expected.

6.1 Investigation of the Current Arrangement

The circuit of Figure 3.1 can be simulated using OrCAD (PSPICE). However, this software package does not support the use of optical emitters. Consequently, the LED is represented by a signal diode with closely matching electrical characteristics. The optical behaviour of the LED can be deduced from analysis of the electrical signals (Section 5.2). The simulated LED current for the given circuit is shown in Figure 6.1. Signal ringing appears as a part of the output electrical signal because of the used filtering inductance at the driving input and pulse shortening inductor in parallel with the LED (L_1 and L_2 in Figure 3.1 respectively). Even though the ringing changes

the diode bias from reverse into forward and vice-versa, the magnitude of the swing is heavily damped and as such does not cause the LED to emit.

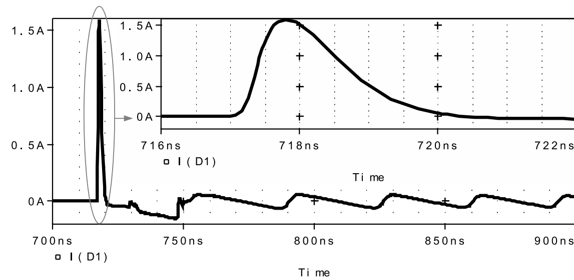

Figure 6.1: Simulated output electrical pulse

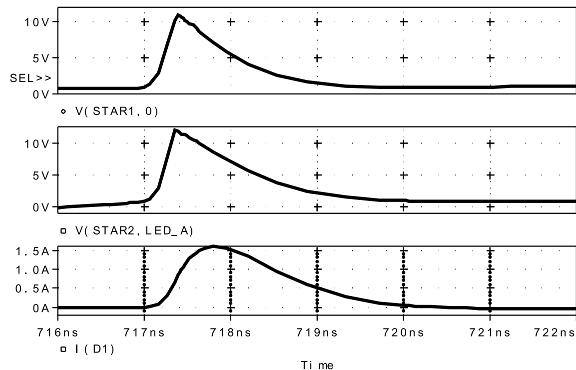

Figure 6.2: Simulated transistor waveforms: top - PNP emitter-base voltage, middle - NPN base-emitter voltage, bottom - LED current

The controlling voltages for the complementary transistors at the time when LED conducts current are shown in Figure 6.2. The signal on the top is V_{EB} of the PNP transistor (Q_1) from Figure 3.1, while the signal in the middle of the Figure is V_{BE} of the NPN transistor (Q_2) from the same Figure. The graph shows that the transistors are simultaneously in either on or off state. The switching action from Figure 6.2 is described in Section 3.4. At the conclusion of the switching action both transistors return to the stable off state. This rapid and efficient switching forms the basis for high speed pulse generation.

Development of this simple regenerative switch and the application of established pulse shaping techniques are considered for creation of electrical signals suitable for the LEDs. Further optimisation is aimed at generating required optical signal (approximately $1ns$ rise time and $3ns$ FWHM – Chapter 1). An essential feature sought from the electrical pulse is its rise time. For reasons explained in Section 3.3 it is believed that the rise time of the optical pulse closely follows the rise time of the electrical drive pulse. This rise time is limited by the switching characteristics of the active devices

used in the circuit. This resemblance, however, does not emerge in the case of the fall time (see Section 3.3). The optical decay can be reduced by reverse biasing the LED as soon as the driving pulse is removed. This is achievable using either the shorted turn technique (Section 3.2.6) or the pulse shortening inductor in parallel with the LED (Section 3.1.4).

6.2 Totem-Pole Drivers

The totem-pole configuration is often used to turn the devices on and actively drive them off. They are high current drivers specifically designed to charge rapidly and discharge the input capacitance of the semiconductor devices [139] and hence improve switching times. Implementation of such configuration is tested here.

The modifications of the initial circuit (Figure 3.1) are aimed at improving the switching times and hence reducing the width of the electric pulse delivered to the LED. The modified circuit (Figure 6.3) is supplied with the positive *d.c.* bias and triggered by a positive going signal, which is superimposed on the supply signal. The discharging of capacitor C_2 is achieved by the regenerative action of transistors Q_1 and Q_2. This provides a fast rising edge signal to the LED. It is intended to actively drive off the electrical signal supplied to the LED using a hybrid form of the totem pole combination of transistors Q_2 and Q_3. This should minimise the effect of the minority carrier lifetime on the optical decay expansion (Section 3.3) as the LED is being actively driven off instead of it being allowed to turn off naturally.

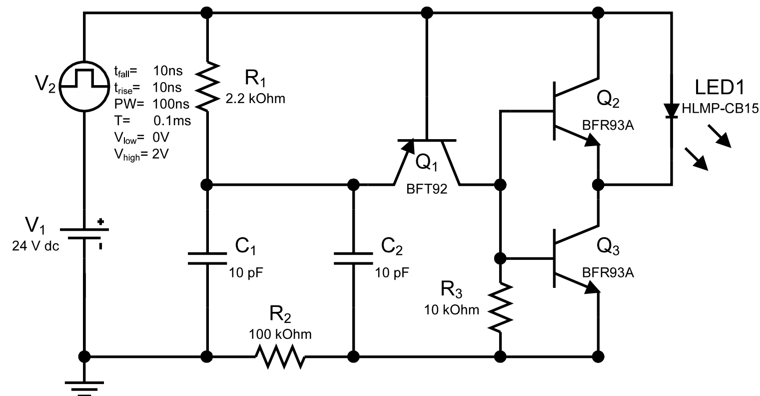

Figure 6.3: Totem-Pole configuration

There are potentially two significant advantages emerging from this circuit configuration: timing and power. Primarily, the electrical pulse driving the LED would be sharpened. The rising edge of the signal would not be altered as it depends on the switching characteristics of the active devices. However, the faster pulse decay, caused by active drive off, would automatically remove the need for any sequential filtering. The elimination of the filtering is preferable as it would allow more efficient energy

transfer from the source to the load with the minimal introduction of the new components into the circuit. The simulation confirms the circuit's operating principle. The simulated electrical pulse flowing through the LED is shown in Figure 6.4.

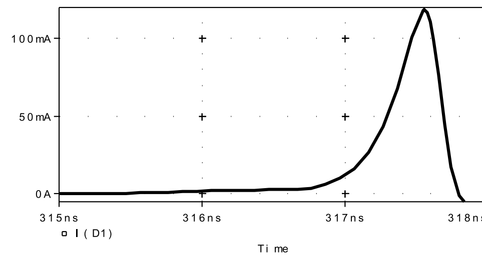

Figure 6.4: Simulated LED current for Totem-Pole configuration

A slow speed prototype is constructed using the pin-and-hole components. The passive components are selected appropriately for the initial slow switching speed. The prototype follows the expected principles of operation and produces the anticipated results. The pulses are generated by the regenerative action of the complementary pair and with the help of the additional transistor (Q_3) which speeds up the switch off time. The LED produces expected optical pulses.

A high speed prototype is constructed using surface mount devices (SMD) with the values as shown in Figure 6.3. The prototype is aimed at developing fast switching electric signals. The LED would convert these into optical pulses that would closely match the initial specified requirements. However, it is found that the circuit does not function in the same manner as its slower pin-and-hole counterpart. The currents that flow through the NPN transistors and the LED do not behave as predicted by the model. A few of the active components were damaged during the testing process. The transistors do not support the high transient currents and as a result they were damaged. Consequently, this circuit does not generate the required regenerative action needed to produce the pulses. The discrepancies from the expected and actual behaviour could not be rectified by the use of different types of transistors. As the efforts to improve the circuit performance failed to result with a reliable system, it was decided to continue the development based on an alternative configuration (as shown in Section 6.3).

It is determined that the conventional totem-pole configuration would need to be employed, as shown in Figure 6.5. The combination of C_3 and R_4 differentiate the initial pulse producing a fast falling edge which improves device turn off and the pulse width. The generated electrical and optical pulses are shown in the upper and lower section of Figure 6.6 respectively. The measurements are taken as described later in Section 6.3.3. It was felt that an alternative solution was required and that further optimisation would be necessary in order to generate more adequate pulses.

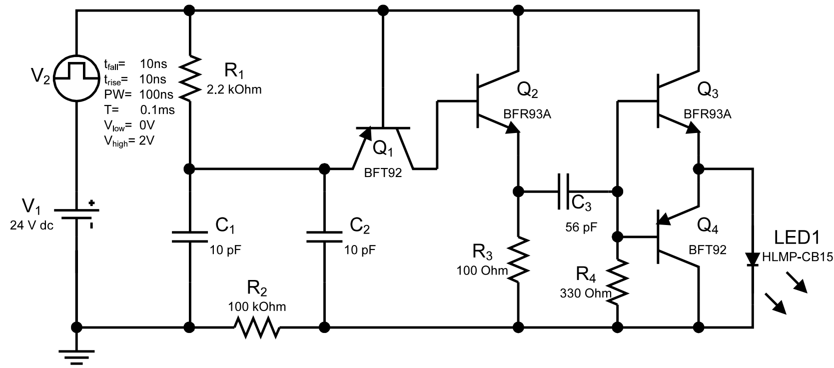

Figure 6.5: Full Totem-Pole configuration

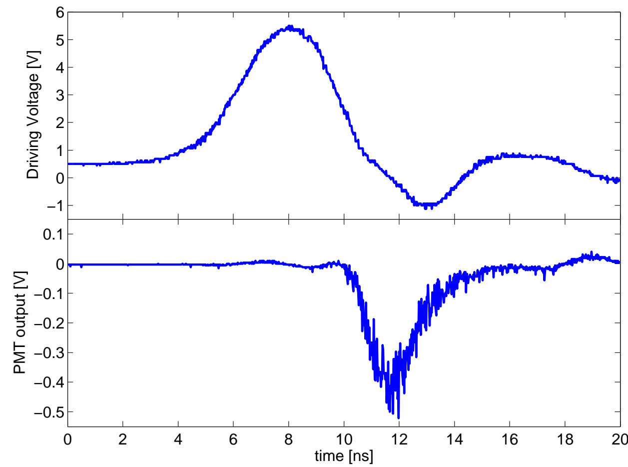

Figure 6.6: Experimantally obtained totem-pole output signal

6.3 Single Output Configurations

The single output drivers are configured so there is a single LED used per driver. Consequently, the output is a single optical signal. These, originally intended, drivers are of the main interest. However, the possibility of using a multiple output drivers and their potential for the reduction of size, complexity and cost is rationally exploited resulting in development of multiple output drivers (Section 6.4).

6.3.1 Switching Configuration

The previously considered cross coupled pair of complementary transistors is reused. The redeveloped free running oscillatory circuit is shown in Figure 6.7. The specified component values are designed to produce pulses with a rise time of $2.9ns$ at a repetition frequency of approximately $23kHz$. The component values (especially C_1) are chosen to optimise speed of the pulses. The repetition rate is arbitrary and is determined by R_1, R_2, R_3 and C_1.

Initially C_1 is uncharged and hence has zero voltage across it. Transistors Q_1 and

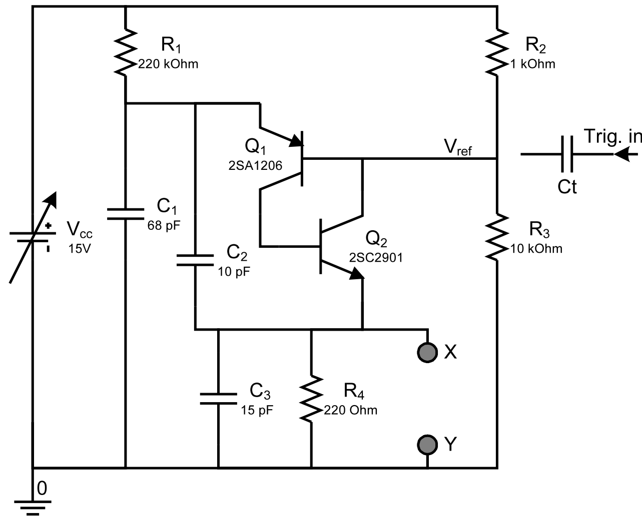

Figure 6.7: New driver standard configuration

Q_2 are both in the off state. The potential V_{ref} is then defined by the potential divider formed by R_2 and R_3. Capacitor C_1 charges through R_1. When the voltage across this capacitor exceeds V_{ref} by the amount of base-emitter voltage of transistor Q_1 the same transistor starts to conduct. This turns on Q_2 which causes V_{ref} to fall quickly turning Q_1 fully on. This action provides a low impedance path for capacitor C_1 to discharge through R_4 and C_3 causing the regenerative switch to return to its initial condition. The values of C_3 and R_4 have been established empirically to give optimum results when driving an Agilent blue LED of type HLMP-CB15 [128] and the pulse forming network attached to the circuit board between points X and Y. The free running period is controlled by the time constant R_1C_1 and the magnitude of V_{ref}. The rise time of the output pulse developed across R_4 is a function of the switching speeds of Q_1 and Q_2 while the turn off time is dictated by the discharge current path formed by Q_1, Q_2, R_4 and the value of C_1. Capacitor C_2 provides a small amount of feedback which enhances the initial 'turn on' time of the pulse.

By varying the supply voltage, V_{CC}, a family of output curves (measured across R_4) can be produced as shown in Figure 6.8 where the curves A to E correspond to different supply voltages. The ringing on the graph is assumed to be caused by parasitic impedance and non-uniform impedance mismatch of the probe cable.

By removing R_3 and connecting a capacitor C_t to point V_{ref} the device can be externally triggered by a negative pulse. The points X and Y in Figure 6.7 are the positions where the LED and its associated pulse forming network is connected.

6.3.2 Pulse Shaping

Figures 6.9 illustrate the four pulse shaping circuits considered. In each case, the points X and Y correspond to those in Figure 6.7. Diode pulse shaping is achieved

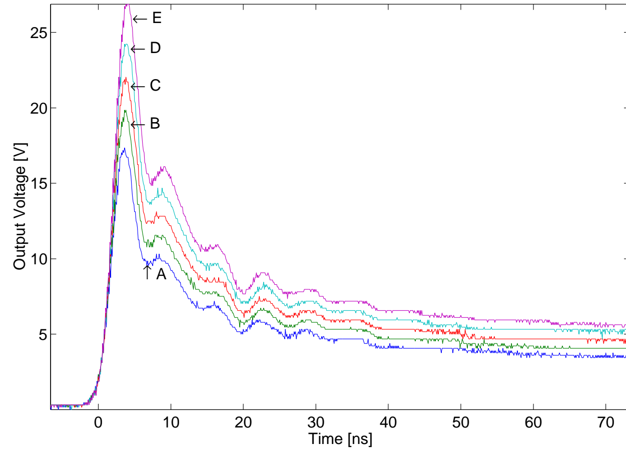

Figure 6.8: Regenerative switch output

by using fast signal diodes (e.g. Phillips 1N4148). These diodes are characterised by a fast recovery time, typically $4ns$ and a very low diode capacitance of $4pF$ at zero bias voltage. By incorporating two diodes in a simple circuit, Figure 6.9a, the inherent output of the regenerative switch is modified. The LED drive voltage rise time is dictated by the switching speed of the regenerative switch but the fall time is controlled by R_5 in series with D_2. The LED initially conducts and then the diode D_2 clamps the drive signal to ground. The inclusion of D_1 in the circuit sharpens the turn on step. The magnitude of resistor R_5 can be used to alter the time response of diode D_2. Hence, it affects the amount of energy delivered to the LED. The switching off action of the LED is controlled actively, but the device is not driven into reverse bias upon removal of the driving pulse.

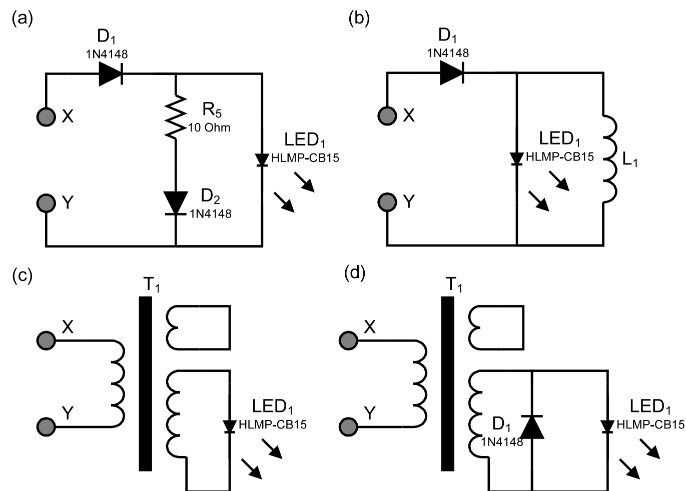

Figure 6.9: Pulse shaping and LED coupling configurations: (a) switching diode shaping, (b) carrier sweep out, (c) shorted turn and (d) shorted turn clipped

In Figure 6.9b, a small inductor L_1 is placed in parallel with the LED forming a

resonant circuit. This allows the voltage across the LED to swing negative. Its shape is controlled by the amplitude of the initial pulse and the voltage dependence of the depletion capacitance of the LED. In general terms it is a damped oscillator. L_1 is constructed from six turns of $0.54mm$ diameter enamel covered copper wire wound on a $5mm$ diameter former. The coil is self-supporting on the circuit board. It has value of $0.19\mu H$ measured at $100kHz$.

The transformer in the circuit Figure 6.9c is fabricated by a bifilar winding of three turns of $0.54mm$ enamel coated copper wire on a toroidal former (Ferroxcube, type TN9/6/3-4C65). An additional two turns of the same type of wire are placed centrally and directly on top of these windings. These additional turns are shorted together. This configuration forms a pulse transformer whose self-inductance is $0.50\mu H$ measured at $100kHz$. A pulse transformer with shorted turns effectively differentiates the input drive pulse. This is caused by the prompt collapse of the magnetic flux within the ferrite core due to the influence of the shorted turns which act as a very low impedance secondary winding. The result of this action is a rapid negative swing. At the operational frequency of the circuit, the physical properties of the ferrite core are at the upper limits of their specification. On the negative swing of the drive voltage the waveform is a function of the inductance of the transformer and the LED capacitance. Modifying this circuit by the inclusion of a clamping diode D_1, Figure 6.9d, restricts the negative swing and subsequent overshoot.

6.3.3 Measurement Technique

The photomultiplier tube (Hamamatsu R7400U) and its associated circuitry are housed in a small metal box (Hamamatsu H6780 PMT module). Typical rise time and electron transit times for the PMT are $0.78ns$ and $5.4ns$ respectively. A coupling assembly is used to interface light sources to the optical window of the photomultiplier tube. The LED is held $4mm$ from the optical window. The gain of the PMT is controlled by a potentiometer which allows the output voltage of the PMT to be adjusted and maintained at a constant level for a wide range of optical intensities. Figure 6.10 is a schematic showing the equipment layout used for evaluation of the drive and optical pulses. The oscilloscope bandwidth is $500MHz$ with the sampling rate of 2 Giga-Samples per second. The type of the probes used in the experiment is Tek P6137 and their capacitance is 10.8 pF. Data were collected and stored in a spreadsheet using Agilent IntuiLink 54600 software. The data is taken from a still measurement. The captured screen data is sampled at 1000 samples per screen shot. This increases the apparent sampling rate. The jitter obtained from the graphs in the following section are the result of this apparent sampling rate which gives the feel of the signals being sampled at the rate faster than actual. MATLAB is used for data plotting.

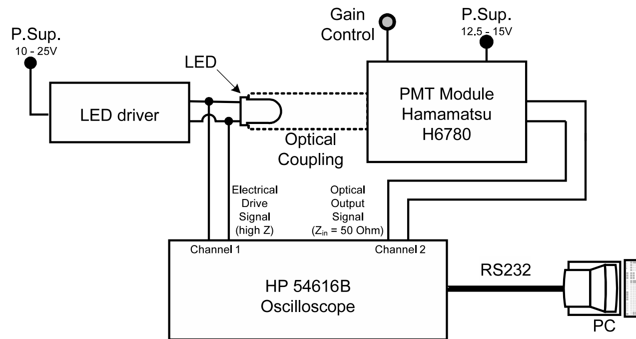

Figure 6.10: Measurements - experimental configuration

6.3.4 Results and Discussion

The narrowest pulses achieved experimentally without pulse shaping have $5ns$ FWHM. The minimum voltage required to stimulate light production using such driving pulses is $5.2V$. When the oscilloscope probe was connected to the circuit, this condition was satisfied for a V_{CC} of $15V$. The amplitude of all of the LED drive pulses are controlled by varying the magnitude of V_{CC} in three steps of $2V$ from the point when the circuit starts generating an optically significant signal. This corresponds to a drive voltage of $12V$ for circuit in Figure 6.9a, $13V$ for the circuit in Figure 6.9b and $17V$ for the circuits in Figures 6.9c and 6.9d. Figures 6.11-6.14 show the measured input drive signal and the observed optical signal for the four circuits illustrated in Figures 6.9a-d. In each Figure the curves $A - D$ correspond to first optically significant signal (A), $+2V$ (B), $+4V$ (C), $+6V$ (D).

From Figure 6.11, it can be seen that a simple diode pulse shaping technique can produce a well defined LED driving pulse. By altering V_{CC} over the stated range of voltages, the current flowing through the LED is altered accordingly. Curve A at the bottom of Figure 6.11 shows a well defined optical pulse which closely mirrors the drive pulse. The delay between the two pulses is caused by the time taken to produce the optical pulse and the electron transit time of the PMT. As the drive voltage is increased there is a corresponding increase in the decay time of the optical pulse B, C and D. Higher drive voltages inject more carriers into the LED. The recombination time taken for these to be neutralised by a fixed number of photon producing traps within the fabric of the LED is also increased. Hence longer decay times are seen in the optical pulse.

In Figure 6.12 it can be clearly seen that swinging the drive voltage negative significantly reduces the decay time of the optical pulse. In effect, this technique removes the excess carriers from the LED's active region. This is analogous to discharging the diffusion capacitance of the LED. The negative portion of the drive pulse is slow to reach its maximum voltage and has an extended duration of 2.5 times that of the drive pulse. This shape is not optimal for the efficient removal of the excess carriers.

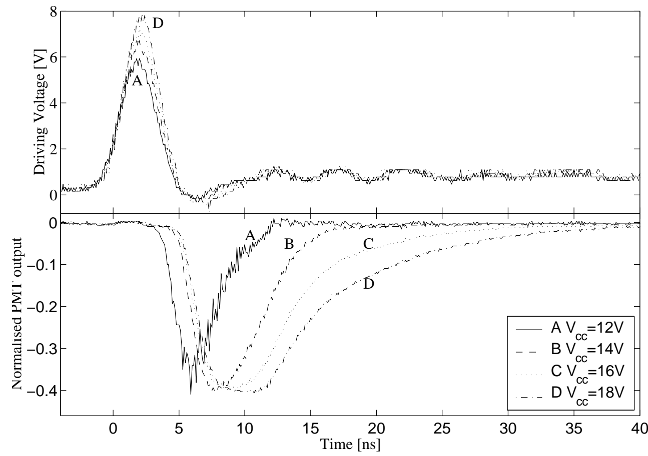

Figure 6.11: LED driving and optical output signals - diode shaping

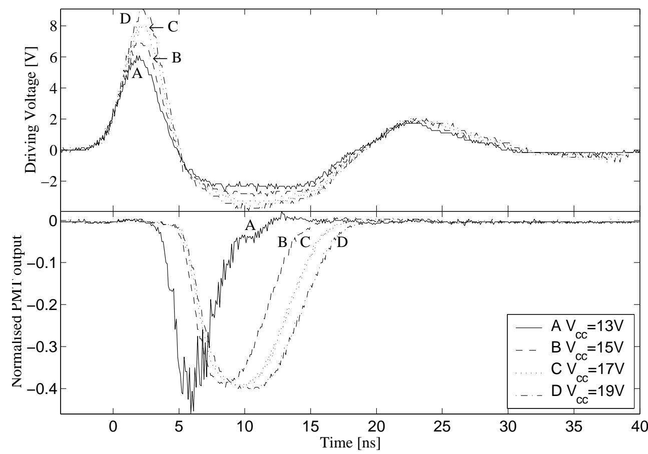

Figure 6.12: LED driving and optical output signals - inductive swing

A transformer with shorted turns (Figure 6.13) effectively differentiates the input drive pulse. This is caused by the magnetic flux within the ferrite core collapsing quickly. A rapid negative swing results from this action. It can be seen from this graph that the optical decay occurring within the LED is markedly improved. Again, the changing depletion capacitance affects the negative waveform. A problem with this basic circuit is that the negative voltage swing can exceed the reverse breakdown voltage of the LED.

The final circuit uses a 1N4148 switching diode to restrict the magnitude of the negative swing by clamping (Figure 6.9d). Its effect can clearly be seen in Figure 6.14 where the negative scale is different from that of Figure 6.13. While the optical output curves of this Figure are similar to those shown in Figure 6.13, the danger of electrical damage to the LED has been reduced.

The measurements of both the electrical and optical $10-90\%$ rise times, FWHM and $90-10\%$ fall times were made from data used to plot Figures 6.11-6.14 and are shown

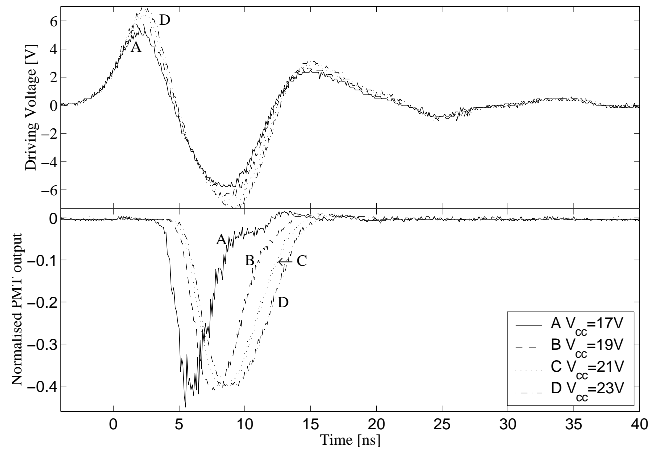

Figure 6.13: LED driving and optical output signals - shorted turn

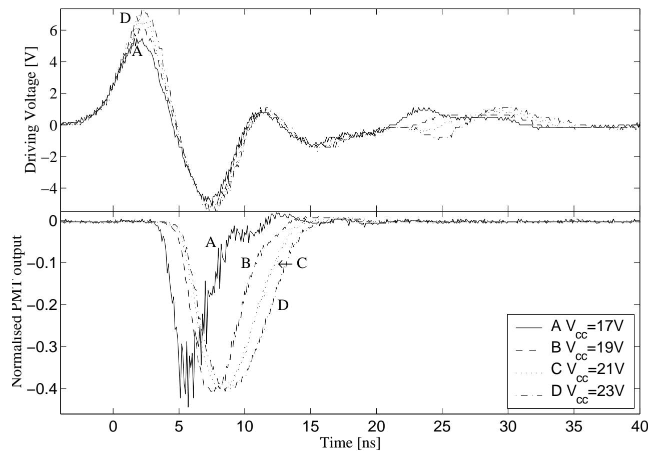

Figure 6.14: LED driving and optical output signals - clipped shorted turn

in table 6.1. Only the best (plot A) and worst (plot D) parameters have been tabulated for the various pulse forming circuits, Figure 6.9. It can be observed that in all cases the positive component of the drive voltage have similar timing characteristics. In the simple circuit (Figure 6.9a) it can be readily seen that for a low LED drive voltage (hence current) the optical pulse closely follows the stimulating voltage. The delay between the drive voltage and the optical pulse is the time taken for the blue LED to produce its optical signal and be detected by the PMT. The light generation is dictated by the structure of the device and the quantum processes involved. At higher drive voltages (larger currents) the time for the excess carriers to recombine with the fixed number of traps within the semiconductor junction extends the optical decay time.

By allowing the drive voltage to swing negative (Figure 6.12) the excess carriers can, to some extent, be removed from the active region thus speeding up the optical pulse. The simple inductive circuit used to achieve this, Figure 6.12, has a slow negative time response and as such is inefficient in carrying out this task. Circuits (Figure 6.13 and

Circuit and Curve		Best - plot A		Worst - plot D	
		electrical	optical	electrical	optical
	time	[ns]	[ns]	[ns]	[ns]
6.9a	rise	2.24	2.12	2.04	1.91
and	FWHM	3.45	3.81	3.56	13.90
6.11	fall	3.10	3.80	2.96	34.29
6.9b	rise	2.04	1.75	2.07	1.85
and	FWHM	3.28	3.27	3.22	8.73
6.12	fall	1.96	2.23	2.05	9.62
6.9c	rise	2.07	1.65	1.99	1.91
and	FWHM	3.79	3.14	3.80	4.36
6.13	fall	1.96	1.87	1.80	3.99
6.9d	rise	3.07	1.85	3.01	2.00
and	FWHM	3.69	3.02	3.67	6.23
6.14	fall	1.88	2.21	1.81	5.97

Table 6.1: Timing results - as measured

6.14) and their corresponding graphs show a fast falling negative component in the drive pulse and this is reflected in a well defined and much quicker optical signals.

6.3.5 Error Treatment

It should be noted that the oscilloscope probes used in this work have an input capacitance of $10pF$. When a measuring probe was connected to the regenerative switch and LED combination, it loaded the circuit reducing the drive power to the LED. Throughout all the measurement of drive voltages, the same probe was coupled to the LED leads but no effect was observed on pulse shape or timing. The optical output measurements were made from the PMT module with the scope set to 50Ω input impedance. No oscilloscope probe is used for the measurement of the optical pulse.

The timing results presented in the table 6.1 do not take into account the limitations in performance of the PMT module and oscilloscope. For measurement systems which use two or more independent components the errors add in quadrature [140] - in this case represented by Equation 6.1.

$$\tau_{r(system)} = \sqrt{\tau^2_{r(PMT)} + \tau^2_{r(scope)}} \tag{6.1}$$

The rise times of the PMT and the oscilloscope are $0.78ns$ and $0.7ns$ respectively. Hence, the rise time of the system, defined by Equation 6.1, is approximately $1ns$. Assuming that the fall time of the PMT is typically twice the rise time, the fall time

of the system, defined by Equation 6.2, approximates to $1.7ns$.

$$\tau_{f(system)} = \sqrt{\tau^2_{f(PMT)} + \tau^2_{f(scope)}} \tag{6.2}$$

A general approximation of the FWHM being equal to the sum of the rise and fall times of the system yields approximate value for the system FWHM of $2.7ns$. This is the response of the system to a delta function light flash. This response degrades the observed FWHM according to Equation 6.3 which can thus be used to calculate the optical FWHM.

$$FWHM_{(optical)} = \sqrt{FWHM^2_{(observed)} - FWHM^2_{(system)}} \tag{6.3}$$

The calculated timing characteristics of the best-achieved optical signals are listed in table 6.2.

Circuit and Curve	$\mathbf{t_{rise}}$ **[ns]**	**FWHM [ns]**	$\mathbf{t_{fall}}$ **[ns]**
6.9a and 6.11 (A)	1.04	2.73	4.23
6.9b and 6.12 (A)	1.04	2.20	2.76
6.9c and 6.13 (A)	0.73	1.31	2.22
6.9d and 6.14 (A)	0.80	0.74	2.10

Table 6.2: Best achieved timing results

The measurements are repeated using a LeCroy (waveRunner 6100 $1GHz$) oscilloscope with the typical rise time of $0.4ns$. The calculated timing characteristics of optical signals from the repeated measurements are in agreement within experimental error with the results shown in table 6.2.

A possible alternative method for evaluating the timing characteristic of the generated light flashes employs the single photon technique [141]. This procedure requires two PMTs. One of those, which collects large amount of light from the flashing device, provides a zero-time signal by sensing the formation of the first few photoelectrons at its cathode. The other PMT is set in such a way that its probability of photon detection per pulse is much less than one. The pulse shape is determined by constructing a histogram of the time differences between two PMT signals over many flashes. This technique is more accurate and with off the shelf components generates a FWHM accuracy of approximately $100ps$ [142].

6.4 Multiple Output Configuration

Even though the single output LED drivers are of the main interest for the intended PMT calibrating application, the possibility of developing the additional functionalities from slightly altered driver could prove to be significant. A multiple optical output

circuitry offers three additional functions. Primarily, it has a potential of providing an option for PMT intensity calibration. To achieve this function, different LEDs emit light of different intensities. Hence, the optical intensity ought to be easily adjustable for individual LEDs. A train of optical pulses provides an identity stamp for the PMTs, so that any noise signals can be filtered out through the pattern recognition. This function requires delay lines achievable through either electrical or optical pulse delay. The ability to control the delay and the intensity could potentially be exploited for other short-lifetime fluorescence investigating applications. The final benefit from the multiple output drivers comes from the reduction of the device count for the same optical output capability. The optical outputs of these drivers are relatively similar to the outputs achieved by the single LED drivers, but the circuits are reduced in size. Hence, there are likely benefits in terms of size, cost and power consumption.

6.4.1 Circuit Arrangement

The single optical output circuit (Figure 6.7) is reconfigured with the aim of developing a multiple optical output driver, shown in Figure 6.15. The circuit relies on operation of complementary pair regenerative switch. The switch consists of transistors Q_1 and Q_2. This section of the circuit obeys the same principles used by the single output driver (Section 6.3). The main addition to that circuit in terms of pulse generation is transistor Q_3. This transistor helps discharge the storage capacitor C_1 when the regenerative switch enters the on state. The outcome is reduction of decay time and FWHM. Transistor Q_3 is biased with the resistor combination $R_2 - R_3$. The additional inductor L_1 aids the switching off process. The inductor comprises of 5 turns of $0.54mm$ diameter enamel covered copper wire wound on a $8mm$ diameter former. The resulting inductance of the constructed inductor is $0.095\mu H$ as measured at $100kHz$. The benefit of using the inductor L_1 in the circuit is evident in Figure 6.16, which shows the output from transistor Q_2 when a 33 Ω dummy load is used between emitter of the output transistor Q_4 and the ground. Two curves show the switch performance with and without the inductor L_1. Even though the rise time of the switch remains the same, the experimentally determined fall time and the FWHM are reduced from $2.38ns$ to $1.54ns$ and from $4.36ns$ to $3.66ns$ respectively.

The introduction of transistor Q_3 and its supporting components improves the driver timing characteristics. This timing enhancement is offset by a significant reduction in power transfer to the regenerative switch output. Hence, the additional transistor Q_4 is added to the circuit to allow sufficient current delivery to the output LEDs. The collector *d.c.* current rating for this transistor is $0.5A$. The transistor gain-bandwidth product depends on the collector current. For small currents this product is approximately one quarter of its optimal value ($800MHz$). This characteristic pre-

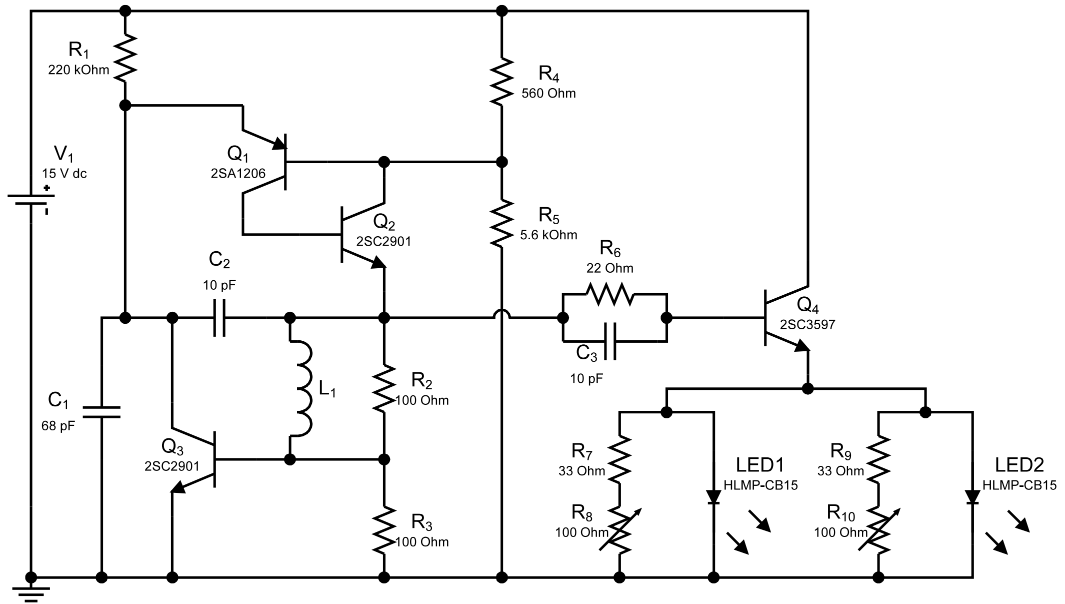

Figure 6.15: Multiple optical output circuit configuration

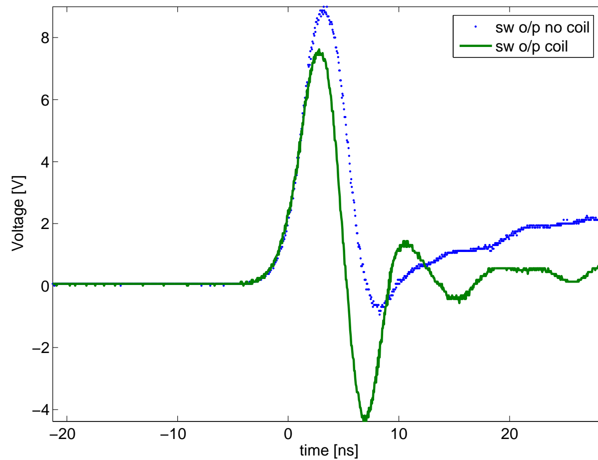

Figure 6.16: Switch output with 33 Ohm dummy load (with and without reg. sw. coil)

vented the use of this transistor and its complementary counterpart in regenerative switch configuration. It is experimentally established that the timing action of the transistors, when configured as the regenerative switch, is poorer than it is the case with the transistors employed. On the contrary, the common emitter configuration (Figure 6.15) provides adequate collector current flow to enable exploitation of optimal gain-bandwidth product and hence faster switching action. The fast switching base current supplied to transistor Q_4 is generated by the regenerative switch. Transistor Q_4 is able to rapidly respond to this signal and provide adequate current for the output LEDs.

The intensity control is provided with a series link consisting of a 33Ω resistor and a 100Ω variable resistor. The setting of the variable resistance changes the impedance

of the path parallel to the LEDs and furthermore alters the amount of current flowing through the LEDs. The intensity control outcome for a single LED is shown in Figure 6.17.

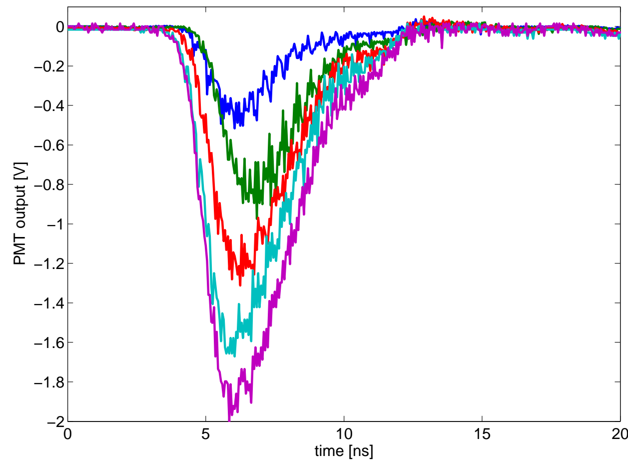

Figure 6.17: Intensity control on a single LED

The multiple outputs can be used as simultaneous multidirectional sources or as fast repeating multiple flashes pointing in the same direction. If the LED outputs are optically coupled and one of the signals is delayed, the optical pulse train shown in Figure 6.18a is generated. As the optical output intensity is adjustable for individual LEDs independently of each other, various intensity and delay patterns are achievable. One of those is shown in Figure 6.18b. The delay is realised in this case with different lengths of coaxial cable connecting the LEDs to the emitter of transistor Q_4. An alternative, and possibly improved solution in terms of signal dispersion, could involve optical delay through a length of optical fibre. This method produces the same train of optical pulses.

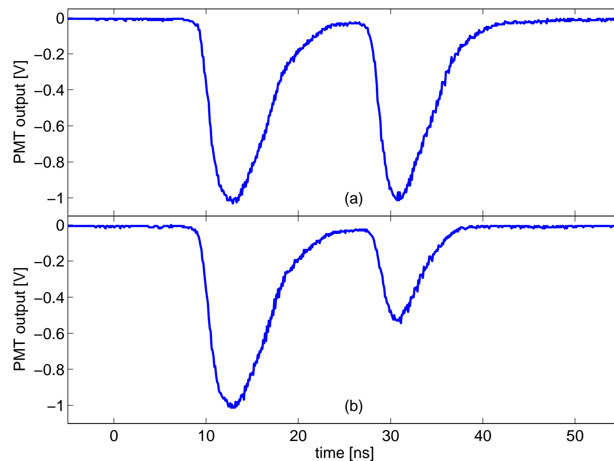

Figure 6.18: Independent intensity control on two LEDs

Figure 6.19 shows the detected optical pulses with the PMT set to its highest sensitivity. Hence, the signals are more disturbed by the noise. This Figure is used to measure timing characteristics of the two pulses in order to compare possible discrepancies caused by the delay line. It emerges that 18ns delay causes no significant pulse alterations. The measured timing characteristics of the two pulses are shown in table 6.3.

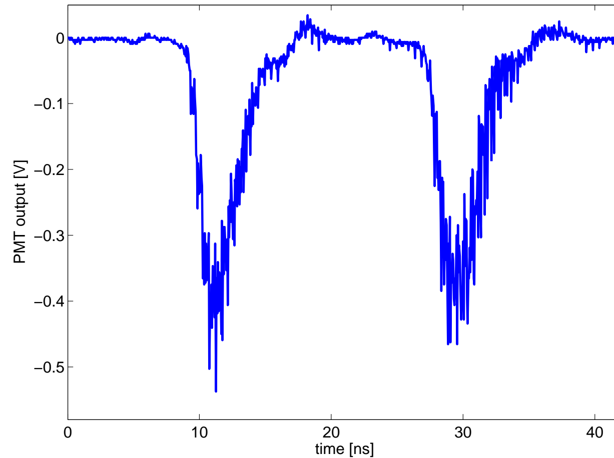

Figure 6.19: Low optical output timing characteristics

Pulse	$\mathbf{t_{rise}}$ **[ns]**	**FWHM [ns]**	$\mathbf{t_{fall}}$ **[ns]**
leading	1.40	3.10	2.92
lagging	1.42	2.92	3.10

Table 6.3: Double output pulse timing

6.5 Chapter 6 Summary

The investigation of the current experimental setup was carried out. The understanding of this arrangement and the theoretical appreciation of the pulse generating and shaping techniques have provided the opportunity for improvement of the LED drivers. It was demonstrated that the newly designed pulses are can produce fast optical signals from LEDs. Taking into account measurement errors a FWHM time of below 1 ns has been achieved. The simplicity of the circuits allows them to be either free running or externally triggered.

The additional functionalities were offered through the use of the multiple optical output drivers. These could be used either as multidirectional sources of light or to generate the train of optical pulses with individually controllable intensity.

Chapter 7

Conclusions and Recommendations for Further Work

This chapter draws conclusion on the important findings achieved in this research. Recommendations are also made concerning possible further work, which may be applied to contribute to development in this area.

7.1 Conclusions

This research has studied the possibility of using blue LEDs for generation of nanosecond range optical pulses. An important part of this experimental program involved the building and optimisation of a practical prototype that would be applicable to the calibration of neutrino detection experiments. The findings are not limited to this application and could be used in a wide range of areas.

A simple regenerative switch using complementary transistors is used in conjunction with simple pulse shaping circuits to produce nanosecond range electronic pulses. These pulses are optimised for active switching of the LED current flow. We demonstrate these pulses are able to overcome the limitations exhibited by the LED material structure. At higher drive currents simple negative transients successfully sweep out the excess carriers from the LED junction. This allows higher intensity blue flashes to be generated. The fast rising optical pulses are actively driven off so that the expected decay of the light output is significantly reduced. This is achieved with the minimal generation of the normally occurring electronic signal ringing. This results with the blue optical pulses whose timing characteristics are worthy of use in calibration of the PMTs and simulation of the Cherenkov radiation in the seawater. Taking into account measurement errors a FWHM time of below $1ns$ has been achieved. The simplicity of the circuits allows them to be either free running or externally triggered for synchronisation purposes. The time jitter between the electrical and optical signals when the

driver is externally triggered is minimal. Hence, the driver is a reliable option for the required distance measurement in underwater astroparticle detectors.

A possibility of the multiple output generation from a single electronic driver is investigated. These drivers can be used either as the simultaneous multidirectional optical sources or as generators of the series of flashes pointing in the same direction. The predefined delay between the pulses is achievable. The optical output intensity is independently adjustable for the individual LEDs. Hence, various intensity and delay patterns are achievable. These features expand the potential range of applications and also extend the prospect of cost reducing in large experimental setups where many optical sources are required for calibration.

In addition to the main experimental results we have discovered that a certain number of the tested LEDs exhibit an unexpected hump-like behaviour in their capacitance-voltage relationship. We have provided adequate reasoning for the existence of this phenomenon and also suggest a possible approach that could make use of this feature in manufacturing quality control.

The work has also on the sideline resulted in an analytical solution of the full diode equation, which takes into account the negative outcomes of the parasitic resistance. Our solution differs from the ones that were previously reported in a sense that we consider both parasitic resistances simultaneously. The generated solution is expressed in the form of an explicit equation. This solution eases the process of theoretical curve fitting to the experimental data.

7.2 Further Work

The emphasis of this study has been on the development of electronic LED driver able to produce nanosecond range blue optical pulses. There is a potential of furthering our development so that pulses with improved light intensity and timing characteristics are obtained. The following recommendations suggest the possible direction that the further work might take if the additional development is to take place in the area.

- The relationship between the current flowing through the LED and the output light intensity is commonly approximated to be linear. Apart from the clear non-linear regions at the very low and very high bias this approximation is relatively accurate. However, this relationship is established at d.c. conditions and it is not clear yet if such estimate can be applied at higher switching speeds. The relationship ought to be investigated at higher frequencies of operation.

- The capacitance - voltage relationship of the LED in low forward bias is somewhat difficult to model because of the unpredictable nature of the depletion capacitance. This capacitive component theoretically tends to infinity at low forward

bias as the depletion layer width tends to zero. It then instantly falls to zero once the depletion layer is removed. Such behaviour is impracticable, but is also difficult to measure. Detailed model of the forward bias capacitance would significantly improve the LED models used for high frequency simulations.

- Further improvements are required should the models generated in this thesis be utilised to their full extent in a-priori pulse circuit design.

- Generation of behavioural LED models from material structure profiles would resolve the issue of parasitic capacitances and inductances. Such models would be more suitable for detailed circuit simulation.

- It is credible that sub-nanosecond pulses using LEDs are possible to achieve. However, the light intensity of such pulses is likely to be very poor. Further investigation in the field is required if the intensity of such short pulses is to be improved.

- The integration of the recently developed 1W and 5W LEDs and the developed drivers is yet to be investigated

- The irregularities observed in the LED capacitance could potentially be used for manufacturing quality control. The observed characteristics could inform about the quality of the deposited crystals. This information could be used for improvements of the deposition methods. Such improvements would result in more predictable device capacitive characteristics and would most certainly contribute to the improvement of the LED pulsing ability.

Appendix A

Practical Diode Equation Analysis

The conclusions are made from the inspection of the relationship between the components of the Equation 2.30. The equation is also mathematically analysed in order to justify the expectations for the I-V behaviour.

A.1 Analysis by inspection

There are four general areas that ought to be considered when analysing the practical diode equation (2.30). The voltage applied to the LED defines these sections. The areas to consider are:

- reverse bias

As $V < 0 \Longrightarrow \left| I_s \left\{ \exp\left[\left(\frac{q(V-IR_s)}{\eta kT} \right) \right] - 1 \right\} \right| \ll \left| \frac{V-IR_s}{R_p} \right| \Longrightarrow I \approx \frac{V-IR_s}{R_p}$.
At reverse bias $|V| \gg |IR_s| \Longrightarrow I \approx \frac{V}{R_p}$.
That is, the reverse bias diode current is approximately equal to the parallel resistance current.

- low forward bias

The exponential term in Equation 2.30 does not become dominant at low voltage levels. Furthermore, 1 is subtracted from this term and the difference is multiplied by very small value of the saturation current.
It follows that $\left| I_s \left\{ \exp\left[\left(\frac{q(V-IR_s)}{\eta kT} \right) \right] - 1 \right\} \right| \ll \left| \frac{V-IR_s}{R_p} \right|$ at low forward bias. Following the argument for the reverse bias case, it follows that the LED current is approximately equal to the parallel resistance current at low forward bias.

- large forward bias

At large forward bias, the exponential term becomes dominant.
$\therefore I \approx I_s \left\{ \exp\left[\left(\frac{q(V-IR_s)}{\eta kT} \right) \right] - 1 \right\}$
Expectedly, this is the standard diode equation (2.29) with the series resistance voltage drop ($-IR_s$) accounted. Therefore, standard diode behaviour is expected in this region, but it should be affected by the voltage drop across the series resistance. As the current increases, this voltage drop should become more significant.

- region between low and large forward bias

The two terms from the Equation 2.30 are comparable in magnitude in this region. Even though the nearly exponential behaviour expected for the large forward bias is obeyed, it is superimposed on the linear component of the parallel resistance current.

The above sections coincide with those generated by the practical diode I-V relationship (Equation 2.30 Figure 2.6).

A.2 Mathematical Analysis

The analytical algebraic solution to the Equation 2.30 proves to be somewhat complicated. It is the use of both, current and voltage, on both sides of the equation that makes the algebraic manipulation of the equation complex. The mixture of the exponential and linear terms disallows generation of explicit expression for either diode current or voltage equation through the use of standard algebraic manipulations. It is the use of the Lambert W function that helps resolve the issue. The function is defined in Equation A.1.

$$\mathrm{LambertW}\left(x\right) e^{\mathrm{LambertW}(x)} = x \tag{A.1}$$

The Lambert W function has a series expansion defined by equation, but is limited to the complex numbers whose real part is less than unity A.2 [143].

$$\mathrm{LambertW}\left(x\right) = \sum_{n=1}^{\infty} \frac{(-1)^{n-1} n^{n-2}}{(n-1)!} x^n \tag{A.2}$$

The Symbolic Math Toolbox of the MATLAB software package is used to solve the Equation 2.30 in terms of diode current. The solution is further simplified using the toolbox. The solution in terms of diode current is shown in Equation A.3. The equation

assumes the thermal voltage to be constant throughout the measurements ($V_t = \frac{kT}{q}$).

$$I = \frac{1}{R_s(R_s+R_p)}\left\{R_sV + \eta V_t R_p \text{LambertW}\left[\frac{I_sR_sR_p\exp\left(\frac{R_p(V+I_sR_s)}{\eta V_t(R_s+R_p)}\right)}{\eta V_t(R_s+R_p)}\right] + \eta V_t R_s \text{LambertW}\left[\frac{I_sR_sR_p\exp\left(\frac{R_p(V+I_sR_s)}{\eta V_t(R_s+R_p)}\right)}{\eta V_t(R_s+R_p)}\right] - I_sR_sR_p\right\} \tag{A.3}$$

This is manually simplified to a shorter form shown in Equation A.4.

$$I = \frac{V - I_sR_p}{R_s+R_p} + \frac{\eta V_t}{R_s}\text{LambertW}\left[\frac{I_sR_sR_p\exp\left(\frac{R_p(V+I_sR_s)}{\eta V_t(R_s+R_p)}\right)}{\eta V_t(R_s+R_p)}\right] \tag{A.4}$$

The Equation A.4 is used to plot the Figures 2.5 and 2.6. It is also employed for I-V characteristic fitting. A solution to the diode I-V relationship based on the same principle was previously employed to diodes and solar cells [144–147].

A.2.1 Manual Solution

Slightly more complex, but certainly preferred, method of solving the diode equation in terms of its current is shown in this section. The LambertW(x) is shown in this section as W(x) so as to keep the mathematical expressions compact. It is possible to rewrite the diode equation (Equation 2.30) to the form shown in Equation A.5

$$I = I_s\left\{\exp\left[(a(V - IR_s)\right] - 1\right\} + \frac{V - IR_s}{R_p} \tag{A.5}$$

where $a = \frac{q}{\eta kT}$ or $a = \frac{1}{\eta V_t}$. The further rearrangements of the diode equation are shown below.

$$I_s\exp(aV)\exp(-aIR_s) - I_s + \frac{V}{R_p} - \frac{IR_s}{R_p} = I \tag{A.6}$$

$$\frac{I_s}{I}\exp(aV)\exp(-aIR_s) - \frac{I_s}{I} + \frac{V}{IR_p} - \frac{R_s}{R_p} = 1 \tag{A.7}$$

$$\frac{\exp(-aIR_s)}{I}I_s\exp(aV) - \frac{1}{I}\left(\frac{V}{R_p} - I_s\right) = 1 + \frac{R_s}{R_p} \tag{A.8}$$

or rather

$$B\exp(AI) + C = DI \tag{A.9}$$

where $A = -aR_s$, $B = I_s\exp(aV)$, $C = \frac{V}{R_p} - I_s$ and $D = 1 + \frac{R_s}{R_p}$, or

$$\exp(AI) + E = FI \tag{A.10}$$

where $E = \frac{C}{B}$ and $F = \frac{D}{B}$. Further rearranging results in Equation A.11.

$$(FI - E)\exp(-AI) = 1 \tag{A.11}$$

Multiplying Equation A.11 through by $-\frac{A}{F}\exp\left(\frac{AE}{F}\right)$ which is an expression independent of I results with Equation A.12

$$-\frac{A}{F}(FI - E)\exp\left(\frac{AE}{F}\right)\exp(-AI) = -\frac{A}{F}\exp\left(\frac{AE}{F}\right) \tag{A.12}$$

or

$$\frac{A}{F}(E - FI)\exp\left(\frac{A}{F}(E - FI)\right) = -\frac{A}{F}\exp\left(\frac{AE}{F}\right) \tag{A.13}$$

which can be solved using the LambertW function to get Equation A.14.

$$\mathrm{W}\left[-\frac{A}{F}\exp\left(\frac{AE}{F}\right)\right] = \frac{A}{F}(E - FI) \tag{A.14}$$

Further manipulation is required:

$$I = \frac{AE - \mathrm{W}\left[-\frac{A}{F}\exp\left(\frac{AE}{F}\right)\right]F}{AF} \tag{A.15}$$

$$I = \frac{A\frac{C}{B} - \mathrm{W}\left[-\frac{AB}{D}\exp\left(\frac{AC}{D}\right)\right]\frac{D}{B}}{\frac{AD}{B}} \tag{A.16}$$

$$I = \frac{AC - \mathrm{W}\left[-\frac{AB}{D}\exp\left(\frac{AC}{D}\right)\right]D}{AD} \tag{A.17}$$

Expressions for A, B, C, D and E can be substituted in Equation A.17.

$$\begin{aligned} I = &\frac{1}{(-aR_s)\left(1 + \frac{R_s}{R_p}\right)}\left\{-aR_s\left(\frac{V}{R_p} - I_s\right) - \right. \\ &\left. -\mathrm{W}\left[-\frac{(-aR_s)\left[I_s\exp(aV)\right]}{1 + \frac{R_s}{R_p}}\exp\left(\frac{(-aR_s)\left(\frac{V}{R_p} - I_s\right)}{1 + \frac{R_s}{R_p}}\right)\right]\left(1 + \frac{R_s}{R_p}\right)\right\} \end{aligned} \tag{A.18}$$

$$I = \frac{-aR_s\left(\frac{V}{R_p} - I_s\right)}{-aR_s\left(1 + \frac{R_s}{R_p}\right)} - \frac{\mathrm{W}\left\{-\frac{(-aR_s)[I_s\exp(aV)]}{1+\frac{R_s}{R_p}}\exp\left[\frac{-aR_s\left(\frac{V}{R_p} - I_s\right)}{1+\frac{R_s}{R_p}}\right]\right\}\left(1 + \frac{R_s}{R_p}\right)}{-aR_s\left(1 + \frac{R_s}{R_p}\right)} \tag{A.19}$$

$$I = \frac{\frac{V}{R_p} - I_s}{1 + \frac{R_s}{R_p}} + \frac{\mathrm{W}\left\{-\frac{(-aR_s)[I_s\exp(aV)]}{1+\frac{R_s}{R_p}}\exp\left[\frac{-aR_s\left(\frac{V}{R_p} - I_s\right)}{1+\frac{R_s}{R_p}}\right]\right\}}{aR_s} \tag{A.20}$$

Replace a with $\frac{1}{\eta V_t}$ where $V_t = \frac{kT}{q}$.

$$I = \frac{V - I_s R_p}{R_p + R_s} + \frac{\eta V_t}{R_s} \mathrm{W} \left\{ \frac{R_s R_p I_s \exp(\frac{V}{\eta V_t})}{\eta V_t \left(R_p + R_s\right)} \exp \left[\frac{R_s \left(I_s R_p - V\right)}{\eta V_t \left(R_p + R_s\right)} \right] \right\} \tag{A.21}$$

$$I = \frac{V - I_s R_p}{R_p + R_s} + \frac{\eta V_t}{R_s} \mathrm{W} \left\{ \frac{R_s R_p I_s}{\eta V_t \left(R_p + R_s\right)} \exp \left[\frac{R_s \left(I_s R_p - V\right)}{\eta V_t \left(R_p + R_s\right)} + \frac{V}{\eta V_t} \right] \right\} \tag{A.22}$$

$$I = \frac{V - I_s R_p}{R_p + R_s} + \frac{\eta V_t}{R_s} \mathrm{W} \left\{ \frac{R_s R_p I_s}{\eta V_t \left(R_p + R_s\right)} \exp \left[\frac{1}{\eta V_t} \left(\frac{R_s \left(I_s R_p - V\right)}{R_p + R_s} + V \right) \right] \right\} \tag{A.23}$$

$$\begin{aligned} I = {} & \frac{V - I_s R_p}{R_p + R_s} + \\ & + \frac{\eta V_t}{R_s} \mathrm{W} \left\{ \frac{R_s R_p I_s}{\eta V_t \left(R_p + R_s\right)} \exp \left[\frac{1}{\eta V_t} \left(\frac{R_s \left(I_s R_p - V\right) + V \left(R_p + R_s\right)}{R_p + R_s} \right) \right] \right\} \end{aligned} \tag{A.24}$$

$$\begin{aligned} I = {} & \frac{V - I_s R_p}{R_p + R_s} + \\ & + \frac{\eta V_t}{R_s} \mathrm{W} \left\{ \frac{R_s R_p I_s}{\eta V_t \left(R_p + R_s\right)} \exp \left[\frac{1}{\eta V_t} \left(\frac{I_s R_s R_p - R_s V + V R_p + V R_s}{R_p + R_s} \right) \right] \right\} \end{aligned} \tag{A.25}$$

$$I = \frac{V - I_s R_p}{R_p + R_s} + \frac{\eta V_t}{R_s} \mathrm{W} \left\{ \frac{R_s R_p I_s}{\eta V_t \left(R_p + R_s\right)} \exp \left[\frac{R_p}{\eta V_t} \left(\frac{I_s R_s + V}{R_p + R_s} \right) \right] \right\} \tag{A.26}$$

The expression in Equation A.26 is identical to that obtained with the help of MATLAB from Equation A.4.

Appendix B

SPICE Diode Model Parameters

Symbol	SPICE keyword	Parameter Name
I_s	IS	Saturation Current
r_s	RS	Ohmic Resistance
η	N	Ideality factor / Emission Coefficient
τ_D	TT	Transit Time
$C_D(0)$	CJO	Zero Bias Junction Capacitance
v_{bi}	VJ	Junction Potential
m	M	Grading Coefficient
E_g	EG	Energy Bandgap
FC	FC	Coefficient for fwd-bias depletion Capacitance formula
BV	BV	Reverse Breakdown Voltage (positive number)
IBV	IBV	Reverse Breakdown Current (positive number)

Table B.1: PSPICE parameters

The PSPICE parameters are used for diode modelling, as described in Section 4.1. The diode is modelled as a current source in series with the series parasitic resistance r_s. When the parasitic capacitance is introduced it is modelled in parallel with the current source. The current source is controlled by the voltage applied across the device. The relationship between these PSPICE equations and the diode theoretical representation are shown below.

Table 4.1 is a PSPICE equivalent of diode current from Equation 2.29. The modelled representation distinguishes two regions: when the diode is in on and off state. The additional term $(V * GMIN)$ is purely computational and has no effect on the modelled current. The model simplifies the diode reverse current to being equal to its steady saturation current only.

The equations of table 4.2 differ from those of table 4.1 in that the ideality factor is introduced to represent the recombination and generation of carriers in the depletion region. Ideally the ideality factor is equal to unity for an abrupt junction. This is the

same parameter that is introduced in Equation 2.30 in order to show realistic diode behaviour.

The diode parameter r_s takes into account the voltage drop across the diode parasitic series resistance. When this parameter is used, the junction voltage is that of the diode voltage reduced by the voltage drop across the series resistance.

The parameters BV and IBV (used in table 4.3) represent the diode breakdown voltage and current respectively. The modelled current is set to be equal to the breakdown current at the point when the voltage across the device equals the breakdown voltage. The PSPICE uses its own representation of the diode current once the bias voltage exceeds the magnitude of the breakdown voltage.

The diode large signal model takes into consideration its parasitic capacitive effects generated by the charge storage. The stored charge and the resulting capacitance are defined by Equations 4.3, 4.4, 4.5 and 4.6. They are clearly determined for the reverse and low forward bias - as shown in the upper parts of tables 4.4 and 4.5. The behaviour of the diode junction capacitance at large forward bias is somewhat unclear and there are various models available to represent this action. The PSPICE uses equations shown in the lower parts of tables 4.4 and 4.5 to model this effect, as described by [93].

Appendix C

LED Capacitance Analysis

C.1 Inverse Capacitance Squared Versus Voltage Plots

Figures C.1 and C.2 illustrate the conventional way of representing the diode depletion capacitance. The plots show squared inverse plot of the capacitance against the bias voltage. The diffusion capacitance is also incorporated in these plots as a section of the measurements refers to the forward bias. It is a common practice to use these plots for the reverse biased conditions in order to extrapolate the impurity concentration of the devices.

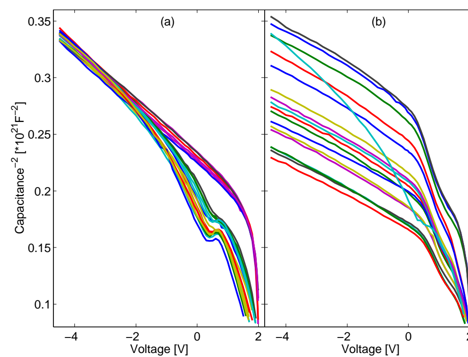

Figure C.1: Inverse of the squared Capacitance vs Voltage for LEDs 1-38

C.2 Depletion Capacitance Fit

The depletion capacitance fit is based on Equation 2.36. The Equation C.1 is used to model this capacitance. The variables c_1 and c_2 are the coefficients generated by the curve fitting. A comparison of the two equations yields the theoretical interpretation

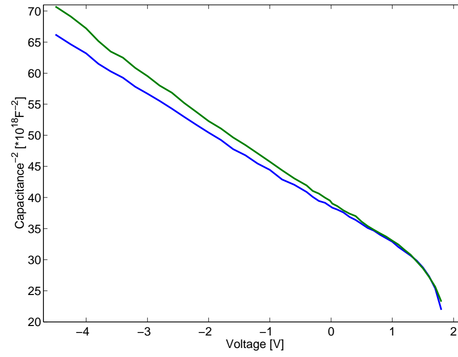

Figure C.2: Inverse of the squared Capacitance vs Voltage for LEDs 39 and 40

of the coefficients shown in Equations C.2 and C.3.

$$C_j = c_1\sqrt{\frac{1}{c_2 - V}} \tag{C.1}$$

$$c_1 = \sqrt{\frac{q\epsilon_S N_B}{2}} \tag{C.2}$$

$$c_2 = v_{bi} \tag{C.3}$$

The results of the depletion capacitance (Equation C.1) fitting to the experimental data are shown in Figures C.3, C.4, C.5, C.6 and C.7. The fitting procedure that uses MATLAB unconstrained nonlinear optimisation function (fminsearch) is detailed in Section 5.1.1.

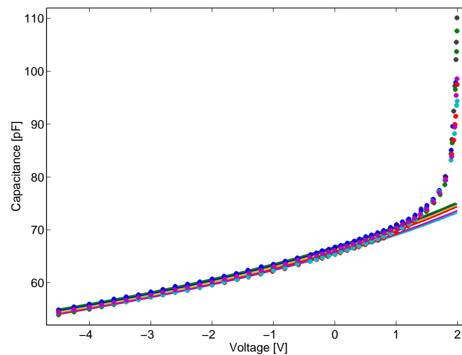

Figure C.3: Depletion capacitance fit to NO HUMP LEDs

C.3 Diffusion Capacitance Fit

The diffusion capacitance that is caused by the injection of the carriers across the junction has an exponential shape (as described by Equation 2.43). The model that is used to represent this capacitance is shown in Equation C.4.

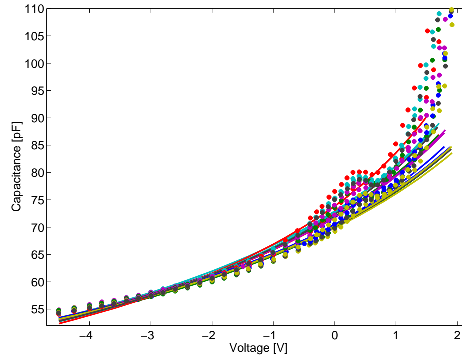

Figure C.4: Depletion capacitance fit to HUMP LEDs

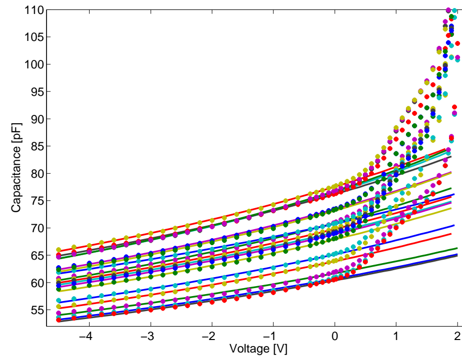

Figure C.5: Depletion capacitance fit to BATHCH2 LEDs (21-37)

$$C_d = c_1 \exp(c_2 V) \tag{C.4}$$

The fitting results are shown in Figures C.8, C.9, C.10, C.11 and C.12.

C.4 Hump Capacitance Fit

Figure C.13 and C.14 show the fitting results for the hump capacitance. The two Figures are also combined and shown in Figure 5.11 in Section 5.1.1. The hump capacitance is a distinct residual from the depletion and diffusion fits and can certainly not be attributed to the measuring system or fitting error. The positions of the humps differ for two LED batches. The Gaussian distribution is found to be an appropriate fit for this capacitance. The fitting model used is shown in Equation C.5. The variables that are extracted from the fit are the amplitude of the hump (c_1), the mean of the distribution (μ) and the standard deviation (σ).

$$C_{hump} = c_1 \exp\left[\frac{-(V-\mu)^2}{2\sigma^2}\right] \tag{C.5}$$

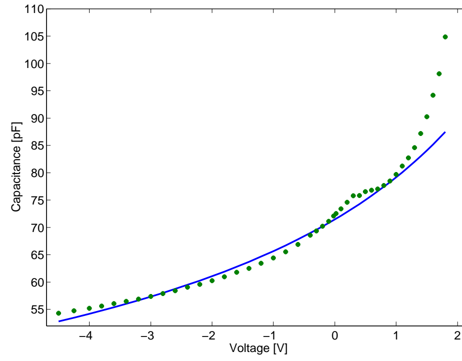

Figure C.6: Depletion capacitance fit to LEDs (38)

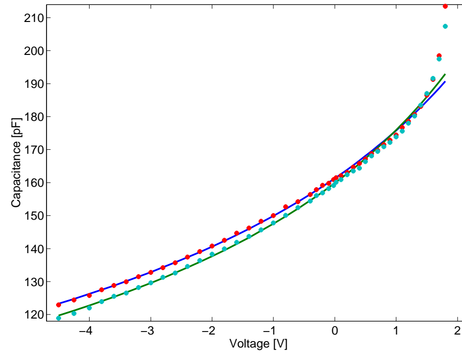

Figure C.7: Depletion capacitance fit to LEDs 39 and 40

C.5 Fitting Errors

The fitting errors are the diode capacitance residuals formed when the depletion, junction and hump capacitance fits are taken away from the experimental measurements. Figures C.15 and C.17 show the fitting error for the NO-HUMP and BATCH-2 LEDs on two different scales. The fitting errors for the other groups of LEDs are less stretched so are shown on a single scale in Figures C.16, C.18 and C.19.

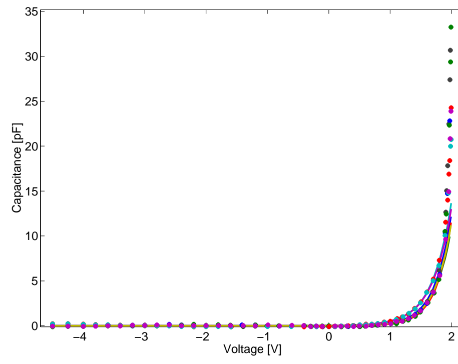

Figure C.8: Diffusion capacitance fit to NO HUMP LEDs

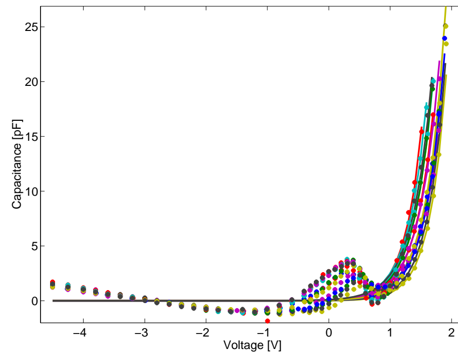

Figure C.9: Diffusion capacitance fit to HUMP LEDs

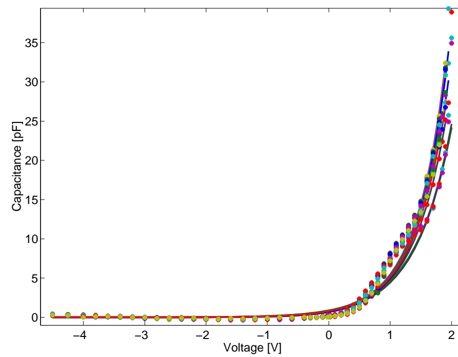

Figure C.10: Diffusion capacitance fit to BATCH2 LEDs (21-37)

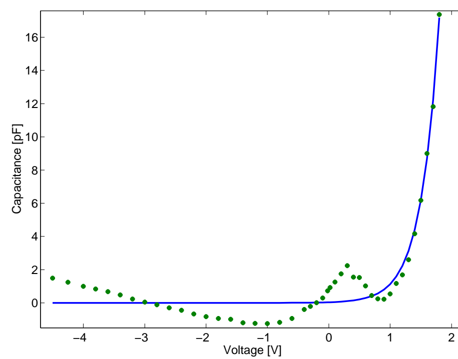

Figure C.11: Diffusion capacitance fit to LED 38

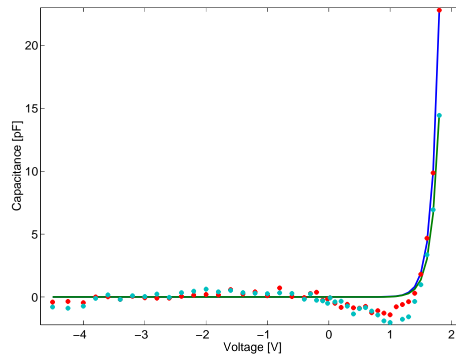

Figure C.12: Diffusion capacitance fit to LEDs 39 and 40

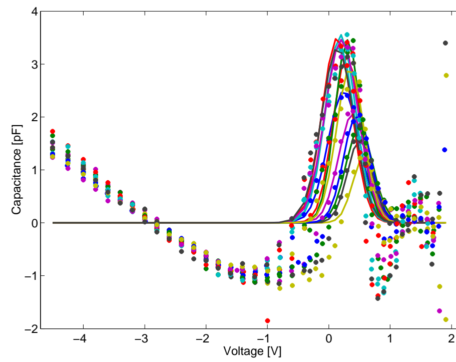

Figure C.13: Hump capacitance fit to HUMP LEDs

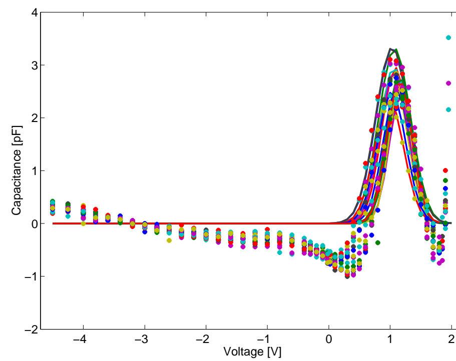

Figure C.14: Hump capacitance fit to BATCH2 LEDs (21-37)

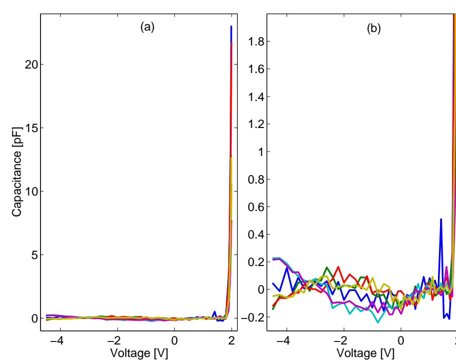

Figure C.15: Capacitance fit error for NO HUMP LEDs

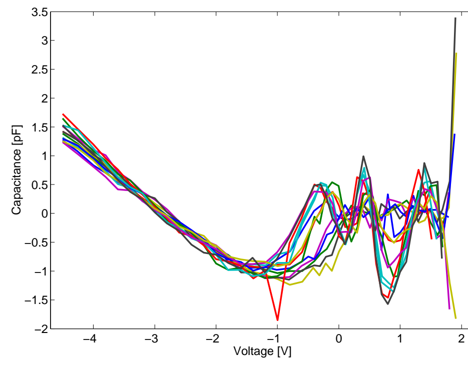

Figure C.16: Capacitance fit error for HUMP LEDs

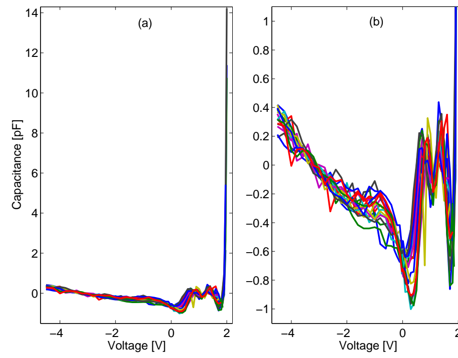

Figure C.17: Capacitance fit error for BATCH2 LEDs

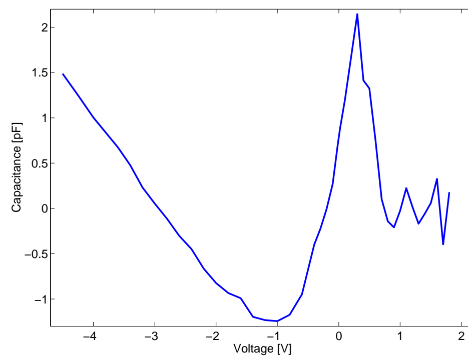

Figure C.18: Capacitance fit error for LED 38

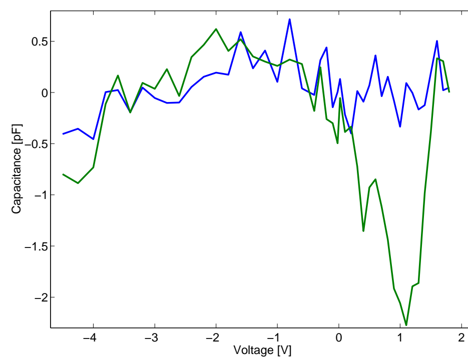

Figure C.19: Capacitance fit error for LEDs 39 and 40

Appendix D

LED Current - Voltage Analysis

Figure D.1 shows the low bias level I-V relationship for the three identified groups of LEDs. The characteristic is shown on the same scale for the HUMP and NO-HUMP LEDs. The BATCH-2 LEDs are shown on the same horizontal, but increased vertical scale. The graphs show the variation in current flowing through the LEDs for the same voltage applied to the devices. The NO-HUMP LEDs exhibit the lowest current flow of the three groups of the LEDs. The current flowing through the BATCH-2 LEDs at the high end of the horizontal scale is by a factor of four larger than of its counterparts from the other groups.

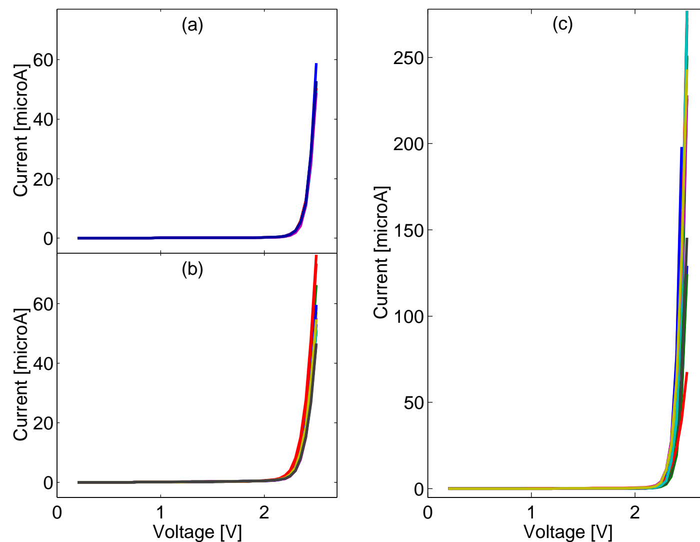

Figure D.1: LED low scale I-V relationship: a) NO HUMP, b) HUMP, c) BATCH2

The model of the diode I-V characteristic is represented by Equation A.4. This relationship is derived from diode practical equation (2.30) as shown in appendix A.2. The behaviour of this relationship is shown on linear and semi-logarithmic scale in Figure D.2.

The above fitting equation is rearranged so that the logarithmic value of this re-

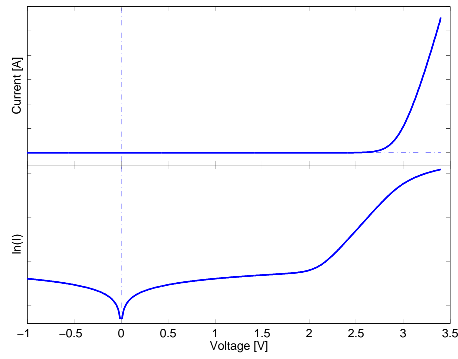

Figure D.2: Practical LED current model

lationship is fitted to the logarithmic value of the experimental data (for the reasons explained in Section 5.1.2). The fitting relies on MATLAB unconstrained nonlinear optimisation function (fminsearch) and is performed in the same manner as the capacitance fitting. The parameters derived from this fit are diode saturation current, ideality factor and series and parallel resistance. The extracted parameters are graphically compared in Figures D.3, D.4, D.5 and D.6. Some form of clustering is evident from each one of those Figures, even though it is less evident in the case of the LED series resistance. The generated clusters match with the originally determined LED grouping.

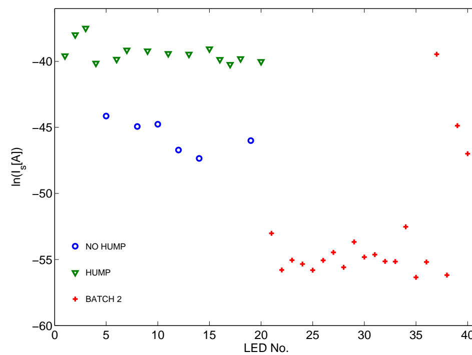

Figure D.3: LED fitting parameter: saturation current - I_S

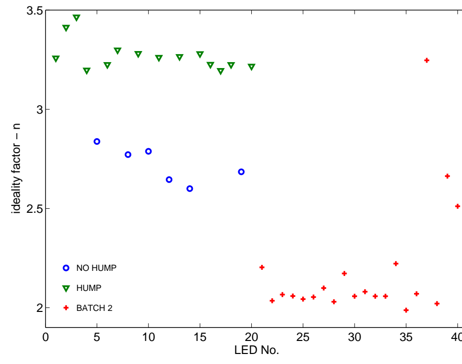

Figure D.4: LED fitting parameter: ideality factor - η

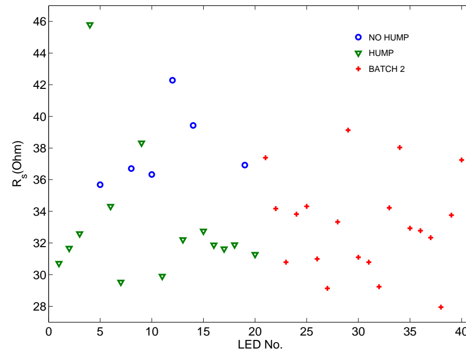

Figure D.5: LED fitting parameter: series resistance - R_S

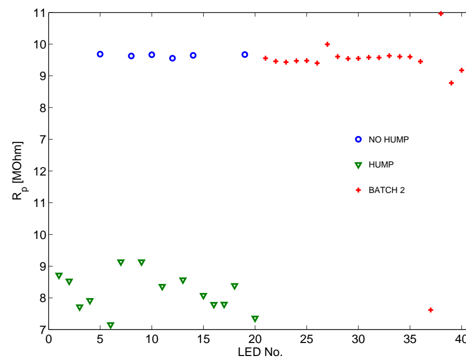

Figure D.6: LED fitting parameter: series resistance - R_P

Appendix E

LED Output Spectrum Analysis

The skewness and kurtosis of the LED normalised relative output spectrum are shown in Figure E.1. There is very little evidence of clustering in this case. Therefore it is concluded that the skewness and kurtosis of the LED output spectrum are not related to the previously established device groupings.

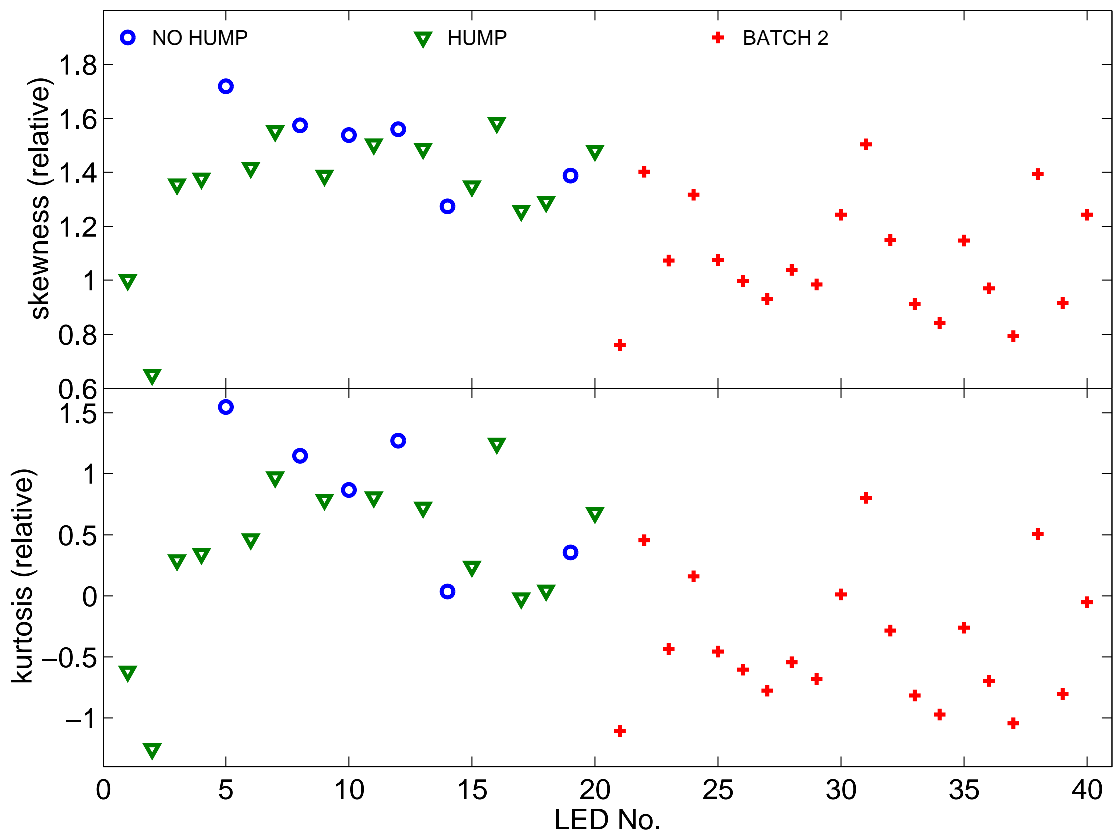

Figure E.1: Skewness and Kurtosis of the LED output spectrum

Appendix F

LED Intensity Analysis

Figure F.1 presents the gradients of the linear approximations derived for the LED relationship between its current and output intensity. The device clustering generated by the LED output intensity coincides with the previously determined LED groups.

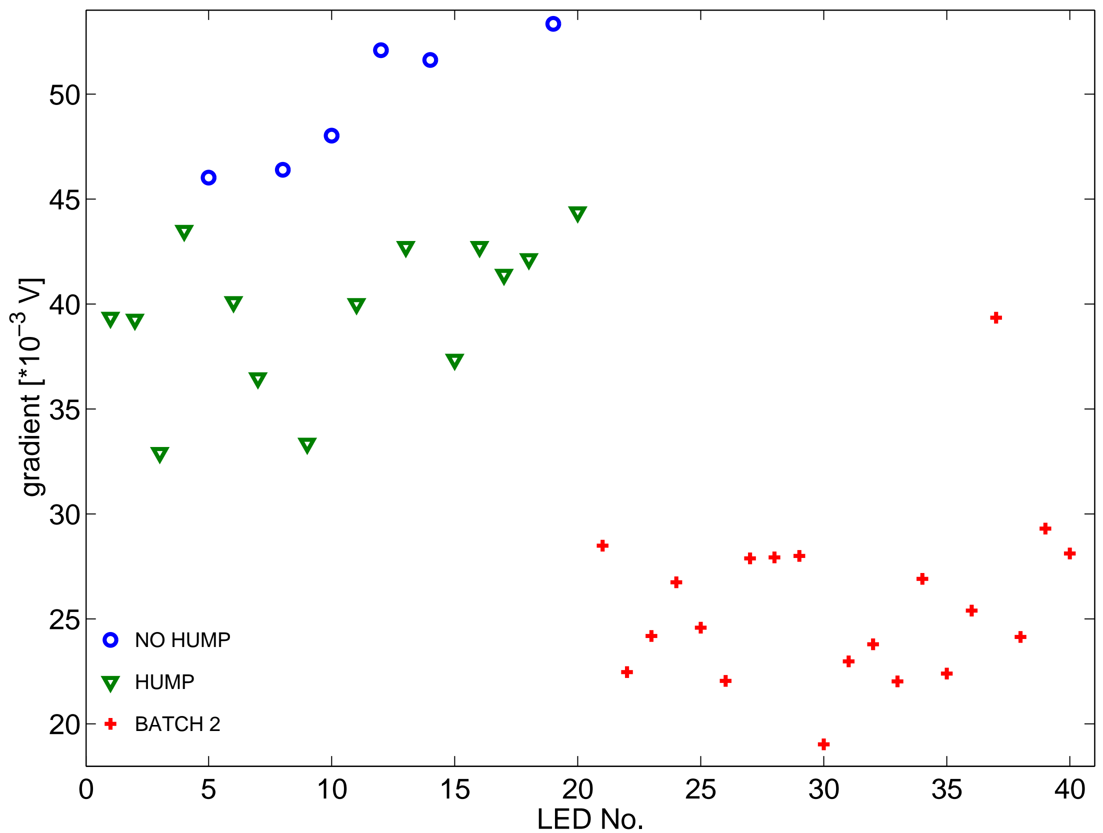

Figure F.1: Slopes of the fitted current - intensity relationship

Appendix G

Using LED as a Photodetector

The skewness and kurtosis of the LED photodetection curves are displayed in Figure G.1. These curves represent the potential difference developed across the devices when exposed to the strong light source (as described in Section 5.1.5).

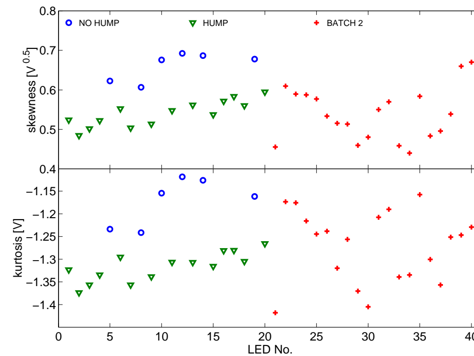

Figure G.1: LED as photodetector - distribution skewness and kurtosis

The normalised photodetection curves of Figure 5.19b are rearranged in Figure G.2 so that two LED batches are displayed separately. Subtle differences are visible at the rising and falling edges of the curves.

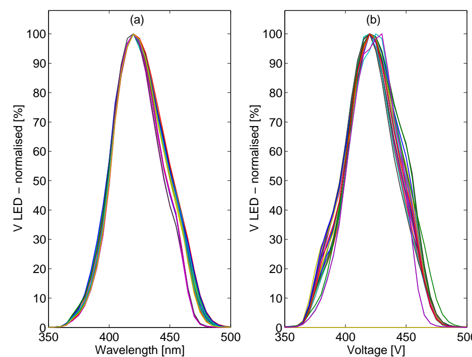

Figure G.2: LED used as photodetector: a) BATCH-1, b) BATCH-2

The Gaussian distribution is fitted to these curves and the differences are shown in

Figure G.3. As predicted from the observation of the curve plots, the BATCH-1 LEDs have a slight dip in the rising edge of the photodetection curves while the BATCH-2 LEDs have a hump in the same position. Both batches (except LEDs 39 and 40) have a hump at the falling edge of the curves. It is also noticed that the NO-HUMP LEDs have narrower spread than it is the case with the other two groups. The Gaussian distribution is fitted to the residual curves of Figure G.3. A typical fit for each of the three groups is shown in Figure G.4. The final fitting errors are shown in Figure G.5.

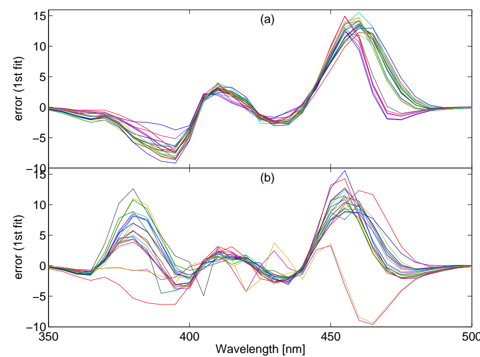

Figure G.3: LED as photodetector - error after first Gaussian fit: a) BATCH-1, b) BATCH-2

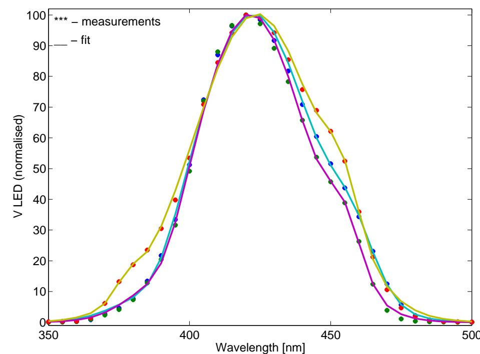

Figure G.4: LED as photodetector - measured data vs complete model: examples LEDs 17 (HUMP), 19 (NO-HUMP) and 21(BATCH-2)

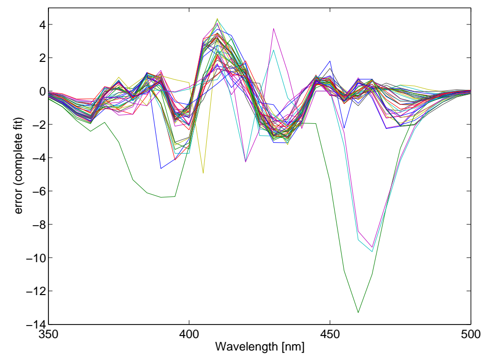

Figure G.5: LED as photodetector - error after complete fit

Appendix H

Blue LED Model Netlist - Using OrCAD Model Editor

The PSPICE below describes the LED model based on the use of two signal diodes in parallel. The diode named LEDMODC includes the capacitive behaviour of the LED and is used to model the LED electrical behaviour. The other diode and its supplementary circuitry are used to model the optical characteristics of the LED.

```
.subckt Dbreak3 1 2 3
D_D1 1 2 LEDMODC
D_D2 N1 N2 LEDMODR
E_E1 N1 0 1 2 1
E_E2 3 0 VALUE={0.054844*V(N4)}
F_F1 0 N4 VF_F1 1
VF_F1 N2 0 0V
R_R1 N4 0 1
.MODEL LEDMODC D(IS=3.83E-19 N=2.986 RS=31.67
+TT=5E-9 EG=2.627 FC=0.5 CJO=6.61E-11 VJ=2 M=0.15)
.MODEL LEDMODR D(IS=3.83E-19 N=2.986 RS=31.67 EG=2.627)
.ends
```

Bibliography

[1] L F Thompson *Cherenkov Ring Imaging and Vector Meson Photoproduction,* University of Sheffield PhD Thesis 1987

[2] J. Carr On behalf of ANTARES Collaboration, *Status of ANTARES in Nov 2005*, Nuclear Instruments and Methods in Physics Research A 567 (2006) 428–432

[3] E. Migneco *et al.*, *Status of NEMO*, Nuclear Instruments and Methods in Physics Research **A567** (2006) 444–451

[4] G. Aggouras *et al.*, *Recent results from NESTOR*, Nuclear Instruments and Methods in Physics Research **A567** (2006) 452–456

[5] IceCube Collaboration, *First year performance of the IceCube neutrino telescope*, Astroparticle Physics **26** (2006) 155–173

[6] V. Aynutdinov *et al.*, *BAIKAL experiment: Main results obtained with the neutrino telescope NT200*, Nuclear Instruments and Methods in Physics Research **A567** (2006) 423–427

[7] U.F. Katz, *Neutrino telescopy in the Mediterranean Sea*, Progress in Particle and Nuclear Physics **57** (2006) 273–282

[8] P Amram *et al.*. (ANTARES collaboration), *The ANTARES optical module*, Nuclear Instruments and Methods in Physics Research **A484** (2002) 369-383

[9] ANTARES collaboration, *Technical Design Report of the ANTARES 0.1km^2 project*, (2001) available in pdf at http://antares.in2p3.fr/Publications/index.html

[10] T Sefzick *et al.*., *A System for Simulation of Scintillator Light Signals*, Nuclear Instruments and Methods in Physics Research **A288** (1990) 571-573

[11] W L Reiter and G Stengl, *A Blue Light Emitting Diode Used as a Reference Element in Scintilation Spectrometers*, Nuclear Instruments and Methods **180** (1981) 105-157

[12] J J Samueli and A Sarazin, *A Nanosecond Pulse Generator and Shaping Circuit with Avalanche Transistors*, Nuclear Instruments and Methods **26** (1964) 71-76

[13] D R Green, *A LED System to Test Scintillation Counter Hodoscopes*, Nuclear Instruments and Methods **151** (1978) 307-312

[14] J S Kapustinsky *et al.*., *A Fast Timing Light Pulser for Scintillation Detectors*, Nuclear Instruments and Methods in Physics Research **A241** (1985) 612-613

[15] www.km3net.org

[16] U F Katz, *KM3NeT: Towards a km3 Mediterranean neutrino telescope*, Nuclear Instruments and Methods in Physics Research Section **A567** (2006) 457-461

[17] C H Liu *et al.*., *Raman, fluorescence and time-resolved light scattering as optical diagnostic techniques to separate diseased and normal biomedical media*, Journal of Photochemistry and Photobiology **B16** (1992) 187-209

[18] A Katz and R R Alfano, *Optical Biopsy - Detecting Cancer With Light*, www.ieee.org/ organizations/pubs/newsletters/leos/feb96/katz.html

[19] Nikiforos Kollias *et al.*., *Endogenous Skin Fluorescence Includes Bands that may Serve as Quantitative Markers of Aging and Photoaging*, The Journal of Investigative Dermatology **111 No.5** (1998) 776-780

[20] H J Round, *A Note on Carborundum*, Electrical World **49** (1907) 309

[21] N Holonyak Jr and S F Bevacqua, *Coherent (visible) light emission from* $Ga(As_{1-x}P_x\ )$ *junctions*, Applied Physics Letters **1** (1962) 82–83

[22] S Nakamura, Stephen Pearton and Gerhard Fasol, *The Blue Laser Diode,* 2nd edition, Springer, 2000

[23] H P Maruska and J J Tietjen, *The Preparation and Properties of Vapor-Deposited Single-Crystal-Line GaN*, Applied Physics Letters **15** (1969) 327-329

[24] I Akasaki and H Amano, *Crystal Growth and Conductivity Control of Group III Nitride Semiconductors and their Application to Short Wavelength Light Emitters*, Japanese Journal of Applied Physics **36** (1997) 5393-5408

[25] J I Panakove *et al.*l, *Electroluminescence in GaN*, Journal of Luminescence **4** (1971) 63-66

[26] US Patent 3,683,240 Aug. 8, 1972, Pankove

[27] J I Pankove *et al.*, *Luminescent properties of GaN*, Solid State Communications **8** (1970) 1051-3

[28] H Maruska, W Rhines and D Stevenson, *Preparation of Mg-doped GaN diodes exhibiting violet electroluminescence*, Materials Research Bulletin **7** (1972) 777-781

[29] R Dingle *et al.*, *Stimulated Emission and Laser Action in Gallium Nitride*, Applied Physics Letters **19** (1971) 5-7

[30] Y Koide *et al.*, *Effect of AlN Buffer Layer on AlGaN/αAl_2O_3 Heteroepitaxial Growth by Metalorganic Vapor Phase Epitaxy*, Japanese Journal of Applied Physics **27** (1988) 1156-1161

[31] US Patent 4,855,249 Aug. 8, 1989, Akasaki *et al.*

[32] H Amano *et al.*, *Metalorganic Vapor Phase Epitaxial Growth of a High Quality GaN film using an AlN Buffer Layer*, Applied Physics Letters **48** (1986) 353-355

[33] S Yoshida, S Misawa and S Gonda , *Improvements on the electrical and luminescent properties of reactive molecular beam epitaxially grown GaN films by using AlN-coated sapphire substrates*, Applied Physics Letters, **42** (1983) 427-429

[34] T Nagatomo *et al.*, *Propertiesof $Ga_{1-x}In_xN$ Films Preparedby MOVPE,* Japanese Journal of Applied Physics **28** (1989) L1334-L1336

[35] K Osamura, S Naka and Y Murakami , *Preparation and optical properties of Ga1xInxN thin films*, Journal of Applied Physics **46** (1975) 3432-3437

[36] H Amano *et al.*, *P-type Conduction in Mg Doped GaN Treated with Low-Energy Electron Beam Irradiation (LEEBI),* Japanese Journal of Applied Physics **28** (1989) L2112-2114

[37] US Patent 5,334,277 Aug. 2, 1994, Nakamura

[38] S Nakamura, Y Harada and M Seno, *Novel Metalorganic Chemical Vapor Deposition for GaN Growth*, Applied Physics Letters **58** (1991) 2021-2023

[39] S Nakamura, *In Situ Monitoring of GaN Growth Using Interference Effects,* Japanese Journal of Applied Physics **30** (1991) 1620-1627

[40] S Nakamura, *GaN Growth Using GaN Buffer Layer,* Japanese Journal of Applied Physics **30** (1991) L1705-L1707

[41] S Nakamura, M Senoh and T Mukai, *Highly P-typed Mg-Doped GaN Films Grown with GaN Buffer Layer,* Japanese Journal of Applied Physics **30** (1991) L1708-L1711

[42] S Nakamura, N Mukai and M Senoh, *High Power GaN P-N junction Light-Emitting diodes*, Japanese Journal of Applied Physics **30** (1991) L1998-L2001

[43] S Nakamura *et al.*, *Thermal Annealing Effects on P-type Mg-doped GaN Films*, Japanese Journal of Applied Physics **31** (1992) L139-L142

[44] S Nakamura *et al.*, *Hole Compensation Mechanism of P-type GaN Films,* Japanese Journal of Applied Physics **31** (1992) 1258-1266

[45] C Wang and R Davis, *Deposition of highly resistive, undoped, and p-type, magnesium-doped gallium nitride films by modified gas source molecular beam epitaxy,* Applied Physics Letters **63** (1993) 990-992

[46] S Nakamura T Mukai and M Senoh, *Si- and Ge-Doped GaN Films Grown with GaN Buffer Layers,* Japanese Journal of Applied Physics **31** (1992) 2883-2888

[47] W Xie *et al.*, *Room temperature blue light emitting p-n diodes from Zn(S,Se)-based multiple quantum well structures,* Applied Physics Letters **60** (1992) 1999-2001

[48] N Yoshimoto *et al.*, *Photoluminescence of InGaN films grown at high temperature by metalorganic vapor phase epitaxy,* Applied Physics Letters **59** (1991) 2251-2253

[49] S Nakamura and T Mukai, *High-Quality InGaN Films Grown on GaN Films*, Japanese Journal of Applied Physics **31** (1992) L1457-L1459

[50] S Nakamura, T Mukai and M Senoh, *Si-Doped InGaN Films Grown on GaN Films*, Japanese Journal of Applied Physics **32** (1993) L16-L19

[51] S Nakamura, M Senoh and T Mukai, *P-GaN / N-InGaN / N-GaN Double Heterostructure Blue-Light-Emitting Diodes*, Japanese Journal of Applied Physics **32** (1993) L8-L11

[52] S Nakamura, M Senoh and T Mukai *High-power lnGaN/GaN double-heterostructure violet light emitting diodes,* Applied Physics Letters **62** (1993) 2390-2392

[53] H Amano *et al.*, *Room-temperature violet stimulated emission from optically pumped AIGaN / GalnN double heterostructure,* Applied Physics Letters **64** (1994) 1377-1379

[54] S Nakamura, T Mukai and M Senoh , *Candela-class high-brightness InGaN/AlGaN double heterostructure blue-light-emitting diodes*, Applied Physics Letters **64** (1994) 1687-1689

[55] S Nakamura *et al.*, *High-Brightness InGaN Blue, Green and Yellow Light-Emitting Diodes with Quantum Well Structures,* Japanese Journal of Applied Physics **34** (1995) L797-L799

[56] I Akasaki *et al.*, *Stimulated Emission by Current Injection from an AlGaN / GaN / GaInN Quantum Well Device*, Japanese Journal of Applied Physics **34** (1995) L1517-L1519

[57] S Nakamura *et al.*, *High-power InGaN single-quantum-well-structure blue and violet light-emitting diodes*, Applied Physics Letters **67** (1997) 1868-1870

[58] S Nakamura *et al.*, *Superbright Green InGaN Single-Quantum-Well-Structure Light Emitting Diode,* Japanese Journal of Applied Physics **34** (1995) L1332-L1335

[59] S Kim, H Amano and I Akasaki , *Surface-mode stimulated emission from optically pumped GaInN at room temperature*, Applied Physics Letters, **67** (1995) 267-269

[60] S Nakamura *et al.*, *InGaN-Based Multi-Quantum-Well-Structure Laser Diodes,* Japanese Journal of Applied Physics **35** (1996) L74-L76

[61] T Mukai, H Narimatsu and S Nakamura, *Amber InGaN-Based Light-Emitting Diodes Operable at High Ambient Temperatures*, Japanese Journal of Applied Physics **37** (1998) L479-L481

[62] T Mukai, M Yamada and S Nakamura, *Characteristics of InGaN-Based UV / Blue / Green / Amber / Red Light-Emitting Diodes*, Japanese Journal of Applied Physics **38** (1999) 3976-3981

[63] T Mukai, M Senoh and S Nakamura, *InGaN-Based Blue Light-Emitting Diodes Grown on Epitaxially Laterally Overgrown GaN Substrates*, Japanese Journal of Applied Physics **37** (1998) L839-L841

[64] T Mukai and S Nakamura, *Ultraviolet InGaN and GaN Single Quantum Well Structure Light Emitting Diodes Grown on Epitaxially Laterally Overgrown GaN Substrates*, Japanese Journal of Applied Physics **38** (1999) 5735-5739

[65] M Yamada *et al.*, *Red-Enhanced White-Light-Emitting Diode Using a New Red Phosphor,* Japanese Journal of Applied Physics **42** (2003) L20-L23

[66] Y Narukawa *et al.*, *Phosphor-Conversion White Light Emitting Diode Using InGaN Near-Ultraviolet Chip*, Japanese Journal of Applied Physics **41** (2002) L371–L373

[67] M Iwaya *et al.*, *High-Power UV-Light-Emitting Diode on Sapphire,* Japanese Journal of Applied Physics **42** (2003) 400-403

[68] M Razeghi and M Henini, *Optoelectronic Devices: III Nitrides*, Elsevier 2004

[69] J Kovac, L Paternai and O lengyel, *Advanced light emitting diodes structures for optoelectronic applications*, Thin Solid Films **433** (2003) 22-26

[70] M Yamada *et al.*, *InGaN-Based Near-Ultraviolet and Blue-Light -Emitting Diodes with High External Quantum Efficiency Using a Patterned Saphire Substrate and a Mesh Electrode*, Japanese Journal of Applied Physics **41** (2002) L1431-L1433

[71] D Moriata *et al.*, *High Output Power 365 nm Ultraviolet Light Emitting Diode of GaN-Free Structure*, Japanese Journal of Applied Physics **41** (2002) L1434-L1436

[72] M Tsukihara *et al.*, *Dislocation reduction in GaN layer by introducing GaN-rich GaNP intermediate layers*, Japanese Journal of Applied Physics **42** (2003) 1514-1516

[73] T Onuma *et al.*, *Improved Emission Efficiency in InGaN / GaN Quantum Wells with Compositionally-Graded Barriers Studied by Time-Resolved Photoluminescence Spectroscopy*, Japanese Journal of Applied Physics **42** (2003) L1369-L1371

[74] A J Steckl *et al.*, *Multiple color capability from rare earth-doped gallium nitride*, Material Science Engineering **B81** (2001) 97

[75] M Yamada, Y Narukawa and T Mukai, *Phosphor Free High-Luminous- Efficiency White Light-Emitting Diodes Composed of InGaN Multi-Quantum Well*, Japanese Journal of Applied Physics **41** (2002) L1246-L248

[76] ProLight PG1N-5LXS 5W Power LED Technical Datasheet

[77] M Meyyappan and L Kelly, *Carbon Nanotubes: Science and Applications,* CRC Press 2004

[78] S V Rotkin and S Subramaney (editors), *Applied Physics of Carbon Nanotubes: Fundamentals of Theory, Optics and Transport Devices,* Springer-Verlag 2005

[79] L Pavesi and E V Buzaneva (editors), *Frontiers of Nano-Optoelectronic Systems,* Kluwer Academic Publishers 2000

[80] J W Plunkett, *Plunkett's Nanotechnology & Mems Industry Almanac 2006,* Plunkett Research Ltd 2006

[81] P Avouris and J Chen, *Nanotube electronics and optoelectronics,* Materials Today **9** (2006) 46-54

[82] US Patent 3,172,862 Mar. 9, 1965, E F Gurnee *et al.*

[83] US Patent 4,356,429 Oct. 26, 1982 C W Tang

[84] US Patent 5,247,190 Sep. 21, 1993 R H Friend, J H Burroughes and D D Bradley

[85] P Le Barny *et al.*, *Application of organic electroluminescent materials in visualisation : Electroluminescence organique*, Comptes rendus de l'Académie des sciences. Série IV, Physique, astrophysique **1** (2000) 493-508

[86] J Kovac, L Peternai and O Lengyel, *Advanced Light Emitting Diode Structures for Optoelectronic Applications*, Thin Solid Films **433** (2003) 22-26

[87] L S Hung and C H Chen, *Recent progress of molecular organic electroluminescent materials and devices*, Materials Science and Engineering **R39** (2002) 143-222

[88] X Xu, G Yu, Y Liu and D Zhu, *Electrode modification in organic light-emitting diodes,* Displays **27** (2006) 24-34

[89] D Gubta, M Katiyar and Deepak, *Various approaches to white organic light emitting diodes and their recent advancements,* Optical materials **28** (2006) 295-301

[90] S M Sze, *Physics of Semiconductor Devices*, 2nd edition, John Willey & Sons, 2002

[91] JM Liu, Photonic Devices, Cambridge university Press, 2005

[92] J Wilson and J Hawkes, *Optoelectronics - an introduction,* 3rd edition, Prentice Hall Europe, 1998

[93] G Massobrio & P Antognetti, *Device Modelling with SPICE*, 2nd Edition, McGraw-Hill, Inc., 1993

[94] E H Rhoderick and R H Williams, *Metal - Semiconductor Contacts*, 2nd Edition, Oxford University Press, 1988

[95] J M Shah *et al.*, *Experimental Analysis and Theoretical Model for Anomalously High Ideality Factors (n>>2.0) in AlGaN/GaN p-n junction diodes*, Journal of Applied Physics **94** (2003) 2627-2630

[96] E F Schubert, *Light Emitting Diodes*, Cambridge University Press, 2003

[97] B G Streetman & S Banarjee, *Solid State Electronic Devices*, 5th edition, Prentice Hall, 2000

[98] M Fukuda, *Optical Semiconductor Devices*, John Wiley and Sons Inc., 1999

[99] M Shur, *Introduction to Electronic Devices*, John Wiley and Sons, 1996

[100] S Nakamura, T Mukai and M Senoh , *High brightness InGaN/AlGaN double heterostructure light emitting diodes*, Journal of Applied Physics **76** (1994) 8189-8191

[101] J A Coekin, *High Speed Pulse Techniques*, Pergamon Press 1975

[102] P W Smith, *Transient Electronics - Pulsed Circuit Technology*, John Wiley and Sons, 2002

[103] J Watson, *Analog and Switching Circuit Design*, Adam Hilger, 1984

[104] D A Bell, *Solid State Pulse Circuits*, 3rd edition, Prentice Hall, 1988

[105] R L Castellucis, *Pulse Logic Circuits*, Litton Educational Publishing, 1976

[106] R S H Boulding, *Principles and Practice of Radar*, 7th edition, George Newnes Ltd, 1963

[107] L Warnes, *Analogue and Digital Electronics*, McMillan Press, 1998

[108] R Littauer, *Pulse Electronics*, McGraw-Hill, 1965

[109] J Budinsky, *Techniques of Transistors Switching Circuits*, Iliffe Books, 1968

[110] A Barna, *High Speed Pulse and Digital Techniques*, John Wiley and Sons, 1980

[111] O H Davie, *The Elements of Pulse Techniques*, Chapman and Hall, 1964

[112] RCA Designer's Handbook, *Solid State Power Circuits*, RCA Corporation, 1971

[113] E Gelder, *Transistor as a switch*, (pi22), Siemens Aktiengesellschaft, 1988

[114] D A LaLand and J A Ross, *Principles of Electronic Devices and Circuits*, Delmar Publishers, 1994

[115] J H Thorngate and P T Perdue, *A Stable Pulsed Light Source using Low-Cost Light-Emitting Diodes*, Nuclear Instruments and Methods **105** (1972) 57-60

[116] R V Vasil'ev, B K Lubsandorzhiev and P G Pokhil, *A Nanosecond Light Source for Scintillation and Cherenkov-Detector Calibration*, Instruments and Experimental Techniques, **43** (2000) 570-572

[117] J J Samueli and A Sarazin, *A Nanosecond Pulse Generator and Shaping Circuit with Avalanche Transistors*, Nuclear Instruments and Methods **26** (1964) 71-76

[118] C C Lo and B Leskovar, *A Measuring System for Studying the Time-Resolution Capabilities of Fast Photomultipliers*, IEEE Transactions on Nuclear Science **21** (1977) 93-105

[119] J A Lodge *et al.*, *A Cross-Field Photomultiplier with Sub-Nanosecond Risetime suitable for Nuclear Studies*, IEEE Transactions on Nuclear SCience **15** (1968) 491-497

[120] J Millman and H Taub, *Pulse, Digital and Switching Waveforms - Devices and Circuits for their generation and processing,* McGraw-Hill, 1965

[121] S Dimitrijev, *Understanding Semiconductor Devices*, Oxford University Press, 2000

[122] *Pulse and Waveform Generation with Step Recovery Diodes*, Hewlett Packard Application Note AN 918

[123] US Patent 4,121,124 Oct. 17, 1978 Hunt

[124] US Patent 3,521,092 Jul. 21, 1970 C H Kalthoff and Boulder

[125] R H Kingston, *Switching Time in Junction Diodes and Junction Transistors*, Proceedings of the IRE **42** (1954) 288-293

[126] M L Riaziat, *Introduction to high-speed electronics and optoelectronics*, John Willey & Sons, 1996

[127] C M Snowden, *Semiconductor Device Modelling*, Peter Peregrinus Ltd, 1988

[128] Agilent Sun Power Series HLMP-CB15 InGaN Blue Lamp - Data Sheet

[129] Marconi TF 1313A 0.1% Universal Bridge - Instruction Manual

[130] E Kreyszig *Advanced Engineering Mathematics,* 7th edition, John Willey and Sons, 1993

[131] J C Lagarias, J A Reeds, M H Wright and P E Wright *Convergence Properties of the Nelder-Mead Simplex Method in Low Dimensions* SIAM Journal of Optimization **9** (1998) 112-147

[132] C Van Opdrop and H K J Kanerva *Current - Voltage Characteristics and Capacitance of Isotype heterojunctions* Solid-State Electronics **10** (1967) 401-421

[133] S Luryi *Quantum Capacitance Devices* Applied Physics Letters **52** (1988) 501-503

[134] G J Borse *Numerical Methods with MATLAB*, An International Thompson Publishing Company, 1997

[135] Spectrometer Control And Data Acquisition System - Datasheet

[136] E Miyazaki, S Itami and T Araki, *Using a light-emitting diode as a high-speed, wavelength selective photodetector*, Review of Scientific Instruments **69** (1998) 3751-3754

[137] L Euler, *De serie Lambertina plurimiscue eius insignibus proprietatibus*, Acta Academiae Scientiarum Petropolitanae **2** (1783) 29-51

[138] E Anderson *et al.*, *LAPACK User's Guide* (www.netlib.org/lapack/lug/lapack_lug.html), 3rd edition, SIAM, 1999

[139] *Gate Drive Design for Large Drive MOSFETs*, Advanced Power Technology Application Note APT 9302

[140] H W Johnson and M Graham *High Speed Digital Design; a Handbook of Black Magic*, New Jersey: Prentice Hall, 1993

[141] L M Bollinger and G E Thomas *Measurement of the Time Dependence of Scintillation Intensity by a Delayed-Coincidence Method* Review of Scientific Instruments **32** (1961) 1044-1050

[142] J E McMillan *The single photon technique for measuring LED pulser flash width* Sheffield Particle Astrophysics (Sheffield University – Department of Physics and Astronomy Internal Publication) (1999) SH-HEP-99-07

[143] http://mathworld.wolfram.com/LambertW-Function.html

[144] T C Banwell and A Jayakumar, *Exact analytical solution for current flow through diode with series resistance*, Electronics Letters **36** (2000) 291-292

[145] A Ortiz-Conde, F J Garcia Sanchez, *Extraction of non-ideal junction model parameters from the explicit analytic solutions of its I–V characteristics,* Solid State Electronics **49** (2005) 465-472

[146] A Jain and A Kapoor, *Exact analytical solutions of the parameters of real solar cells using Lambert W-function*, Solar Energy Materials & Solar Cells **81** (2004) 269–277

[147] A Ortiz-Conde, F J Garcıa Sanchez and J Muci, *Exact analytical solutions of the forward non-ideal diode equation with series and shunt parasitic resistances* - Technical Note, Solid-State Electronics **44** (2000) 1861-1864